Pattern formation in nanoparticle suspensions: A Kinetic Monte Carlo Approach

by

Ioan Vancea

A Doctoral Thesis

Submitted in partial fulfilment of the requirements for the award of Doctor of Philosophy of Loughborough University

November 30, 2010

Abstract

Various experimental settings that involve drying solutions or suspensions of nanoparticles often called nano-fluids have recently been used to produce structured nanoparticle layers. In addition to the formation of polygonal networks and spinodal-like patterns, the occurrence of branched structures has been reported.

After reviewing the experimental results, the work presented in this thesis relies only on simulations. Using a modified version of the Monte Carlo model first introduced by Rabani et al. [95] the study of structure formation in evaporating films of nanoparticle solutions for the case that all structuring is driven by the interplay of evaporating solvent and diffusing nanoparticles is presented.

The model has first been used to analyse the influence of the nanoparticles on the basic dewetting behaviour, i.e., on spinodal dewetting and on dewetting by nucleation and growth of holes. We focus, as well, on receding dewetting fronts which are initially straight but develop a transverse fingering instability. One can analyse the dependence of the characteristics of the resulting branching patterns on the driving effective chemical potential, the mobility and concentration of the nanoparticles, and the interaction strength between liquid and nanoparticles. This allows to understand the underlying fingering instability mechanism.

We describe briefly how the combination of a Monte Carlo model with a Genetic Algorithm (GA) can be developed and used to tune the evolution of a simulated self-organizing nanoscale system toward a predefined nonequilibrium morphology. This work has presented evolutionary computation as a method for designing target morphologies of self-organising nano-structured systems.

Finally, highly localised control of 2D pattern formation in colloidal nanoparticle arrays via surface inhomogeneities created by atomic force microscope (AFM) induced oxidation is presented and some simulations are shown.

Furthermore, the model can be extended further, and by including the second type of nanoparticle, the binary mixture behaviour can be captured by simulations.

We conclude that Kinetic Monte Carlo simulations have allowed the study of the processes that lead to the production of particular nanoparticle morphologies.

List of publications

P. J. Moriarty, M. O. Blunt, C. P. Martin, E. Pauliac-Vaujour, A. Stannard, B. Tadic, M. Suvakov, I. Vancea and U. Thiele, *Patterns and Pathways in Colloidal Nanoparticle Assemblies*, in The Oxford Handbook on Nanoscience and Technology: Frontiers and Advances, ed. A.V. Narlikar and Y.Y. Fu, Oxford University Press (2010), ISBN13: 9780199533046

U. Thiele, I. Vancea, A. J. Archer, M. J. Robbins, L. Frastia, A. Stannard, E. Pauliac-Vaujour, C. P. Martin, M. O. Blunt and P. J. Moriarty, *Modelling approaches to dewetting evaporating thin films of nanoparticle suspensions*, J. Phys.-Cond. Mat. , 21 264016 (2009)

I. Vancea, U. Thiele, E. Pauliac-Vaujour, A. Stannard, C. P. Martin, M. O. Blunt and P. J. Moriarty, *Front instabilities in evaporatively dewetting nanofluids*, Phys. Rev. E , 78 041601(2008)

E. Pauliac-Vaujour, A. Stannard, C. P. Martin, M. O. Blunt, I. Notingher, P. J. Moriarty, I. Vancea and U. Thiele, *Fingering instabilities in dewetting nanofluids*, Phys. Rev. Lett., 100 176102 (2008)

C. P. Martin, M. O. Blunt, E. Pauliac-Vaujour, I. Vancea, U. Thiele and P. J. Moriarty, *Controlling pattern formation in nanoparticle assemblies via directed solvent dewetting*, Phys. Rev. Lett., 99 116103 (2007)

P. Siepmann, C. P. Martin, I. Vancea, P. J. Moriarty, N. Krasnogor, *A genetic algorithm approach to probing the evolution of self-organised nanostructured systems*, Nano Letters.; (Letter); 2007; 7(7)

Acknowledgments

First and foremost, I would like to thank you to my supervisor Prof. Uwe Thiele for his support, encouragement and his patient guidance. Thank you Uwe for having me as a student and to introducing me in the mysteries of research. Your positive outlook inspired me and gave me confidence.

I am grateful to the Max Planck Institute for the Physics of Complex Systems in Dresden, Germany and to Loughborough University, UK, for providing me with such excellent working conditions. I acknowledge financial support by the European Union via the FP6 Marie Curie scheme [Grant MRTN-CT-2004005728 (PATTERNS)].

I want to address many thanks to the people involved in the PATTERNS network: to Philip Moriarty, Chris Martin (Nottingham Nanoscience Group) for their help and useful discussions and all the other people - students and permanent staff - of the network.

Special thanks also to Andrew Archer, Lubor Frastia, Desislava Todorova, Fathi Bribesh, Mark Robbins, Mariano Galvagno, Philippe Beltrame and Santiago Madruga for useful discussion and suggestions during our group meetings and for enjoyable beer/juice evenings. The good atmosphere within the group has ensured a pleasant working experience.

In addition I am grateful for the support from my previous professors Ion Cotaescu, Dumitru Vulcanov, Gheorghe Ardelean and Dana Petcu from "Universitatea de Vest", Timisoara, Romania, but also from my friends including Dan Marius, Marian Stingaciu and Bogdan Faina.

Last but not least I would like to thank my wife Ani for keeping her patience when I was losing mine and for her loving support, and to my parents, brother and sister for their understanding and support.

Contents

List of Figures

Chapter 1

Introduction

Spontaneously-formed patterns appear in a wide variety of natural phenomena including growing trees, river networks, dendrites in solidification, animal skins and crystallisation [2].

Although pattern formation is ubiquitous in nature, so far there does not exist an associated universal theory. Anyone hoping to understand the complexity of pattern formation will have to content themselves with a set of general principles, through which some experimentally observed complex structures can be explained. In order to look at the "big picture", one has to concentrate on finding one's way towards unifying the principles of non-equilibrium pattern formation. Spontaneous pattern formation is generally the result of a competition between two or more driving forces. The more balanced the competition is, the more complex and visually stunning the pattern will be.

One aspect of pattern formation is the breaking of symmetry. This concept is not trivial and may be explained as follows. When a pattern-forming system (initially random and isotropic) is driven away from its equilibrium state, it tends to do so by breaking as little symmetry as possible at a time. This explains why lines (e.g. wrinkling in polymer films, symmetry broken along one direction) and hexagons (e.g. honeycomb-like convection cells, symmetry broken along two directions) are very commonly observed patterns. As a result, a close-to-equilibrium system will often appear highly symmetrical, which incidentally also makes it rather striking to the eye, whereas a far-from-equilibrium system may present little or no symmetry.

There exists a difference between the order that characterises an equilibrium system, like a crystal for example, and the ordered non-equilibrium states arising from spontaneous pattern formation. In the former systems, the periodicity of the system is determined by the dimension and geometry of its elementary components. The latter systems, on the other hand, are

maintained out of equilibrium by a continuous flow of energy. Patterns formed under these conditions are called dissipative structures. As opposed to the previously described equilibrium systems, they exhibit a spatial scale which is the result of intrinsic interactions within the system (and therefore is steady in the face of perturbations).

Patterns mean usually non-stationary and nonuniform states of a system which is driven away from equilibrium and which represents the temporal and spatial evolution of observable quantities like the velocity field of a fluid, the concentration field of chemical reactants or biological species. Nonlinear waves or pulse trains are simple patterns which often arise just above onset of pattern formation and may appear also periodic in time and/or space. If the system is driven further away from equilibrium, there are, as well, complex patterns which can replace simple patterns (via a secondary instability).

Pattern formation process can be observed if the system is far away from equilibrium. That is to say, that are not in their thermodynamically most stable state. Away from equilibrium there is no free energy functional defined and no minimisation principle holds, so, the well developed, known tools of classical statistical mechanics are usually not applicable for studying systems far from equilibrium. When a system reaches equilibrium, entropy production ceases.

In the 1930s the Norwegian scientist Lars Onsager [85, 86, 87], began to study the factors that govern entropy production while equilibrium has not been attained. He considered the case where only small deviations from an equilibrium state is taken into account and he showed that under these conditions there are universal laws which relate to various forces and rates which do not depend on the specific details of the system being considered. For this work, Onsager was awarded the Nobel prize for chemistry in 1963. However, for complex patterns forming away from equilibrium, free energy is not the determining criterion, nor is it the minimum entropy production, as initially believed by Prigogine in the 1950s, and by Landauer in 1975.

The first experimental studies of pattern formation were carried out by H. Bénard [4] in a fluid placed between two horizontal plates and heated from below. The vertical temperature difference $\Delta T = T_{bottom} - T_{top}$ across the fluid is an external driving that can be adjusted by the experimentalist, Fig. 1.1. A control parameter, the Rayleigh number R serves as a measure for the "distance" from equilibrium which corresponds to $\Delta T = 0$. A non equilibrium state is enforced as ΔT increases. Heat is transported by both convection (above R_c) and conduction (below a threshold of R_c). At higher R_c turbulent behaviour is observed.

Lord Rayleigh suggested a mechanism for the instability of the stationary conducting state

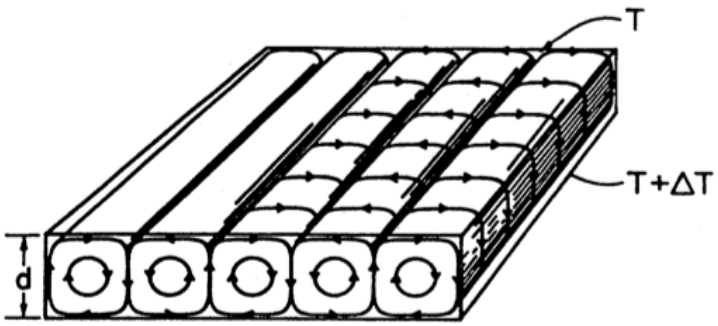

Figure 1.1: Schematic picture of Rayleigh-Bénard convection showing fluid streamlines in an ideal roll state (reproduced from [21]).

of the fluid [97]. He examined how far the results obtained by H. Bénard [4] in his experiments can be explained theoretically. Rayleigh's system is known as Rayleigh-Bénard convection.

It was used for some of the most accurate measurements on pattern formation and has become a paradigm. Other examples are Bénard-Marangoni convection [59] where the upper surface of a shallow fluid is open to the air and temperature dependent surface tension destabilises instead of buoyancy, and Taylor-Couette flow [119], where the fluid is placed in the gap between two vertical concentrical rotating cylinders, Fig. 1.2. There, the centrifugal force replaces the buoyancy force and circular rotating rolls (called Taylor vortices) are established in planes perpendicular to the axis of the cylinder.

Beside the described classical pattern forming systems, attention focusses more and more on systems related to material science and technological processes where structure formation occurs. Typical examples include drying macroscopic drops of colloidal solutions of micron- or nanometer-sized particles [24, 23, 25, 46, 51], spin-casted aqueous collagen solutions [73, 72, 127], spin-casted solutions of polystyrene in benzene [56], and spin-casted solutions of polyacrylic acid (PAA) in toluene [47]. The behaviour presented in these studies is generic for a wide class of solvents and solutes (see, e.g., references in [56]). More complex situations have also been studied, such as evaporating thin films of a binary polymer solution on horizontal [45] or inclined [79] substrates, a drying binary suspension of hard-sphere colloidal particles and a non-adsorbing polymer [48], and structuring of polymer solution films caused by high-temperature evaporation/boiling in a dip-coating setting [8, 9].

For the less complex systems, in several regions of the parameter space, the dewetting behaviour of the solutions appears to be very similar to that described for simple polymeric liquids

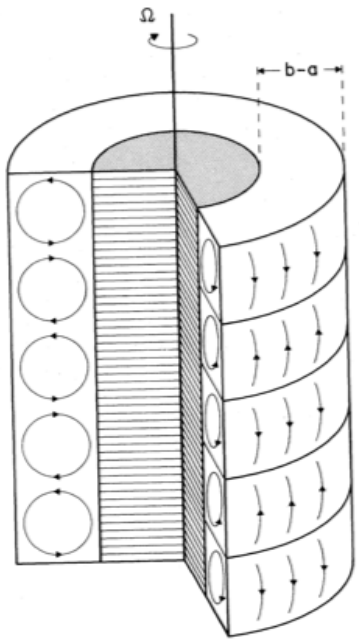

Figure 1.2: Schematic picture of the Taylor-Couette system, showing fluid streamlines for the case when the inner cylinder is rotated at a rate $\Omega > \Omega_c$, (reproduced from [21]).

[22, 99, 123, 108]. In these regions it is possible to use the solute to "image" the dewetting patterns created by the volatile solvent. This route was taken, e.g., in Refs. [73, 127]. This is, however, not the case in other parameter regions. Most strikingly, the experiments show that dewetting (evaporating) solutions show much stronger transverse instabilities of the dewetting front than pure liquids (see, e.g., Refs. [122, 47, 91]).

Different modelling approaches are developed to study thin liquid films on solid substrates. The most convenient approach is the formulation of the model in terms of nonlinear partial differential equations. This method works just in some cases. For example, on the mesoscopic scale, the dynamics of a thin film of pure liquid can be described by a thin film equation derived using a long wave approximation [88, 54]. However, continuum models using Navier-Stokes equations with no-slip or slip boundary conditions at the substrate work only in a limited range of film thicknesses. Below this thickness the solvent dynamics is dominated by evaporation and it is necessary to find alternative models. These alternatives include molecular dynamics simulations (MD), lattice-based technique such as Monte Carlo simulations (MC), and other probabilistic molecular models.

For the presently studied system of an evaporating solution of gold nanoparticles that dewets a silicon substrate [42, 41, 77, 69, 70], we discuss our results in the context of a kinetic Monte

Carlo approach in a two-dimensional model [95, 69, 120] which is found to give useful results and estimates in agreement with the experiments [70, 91].

Our focus is to understand the nanoscale dynamic behavior of thin films of nanoparticle suspensions, relevant to the emerging field of nanotechnology, especially for achieving durability and reliability of coating processes/techniques, and in nanoscale devices.

This report describes the results of my attempts to understand the related phenomena by using Monte Carlo simulations. After an overview over experimental techniques, a short introduction in a continuum theory of thin films, based on the Navier-Stokes equations using lubrication approximation, is given. The model used in the simulations is introduced in detail and a justification of its usage is discussed. The second part of the report presents the influence of the nanoparticles on the basic dewetting behavior, i.e., on spinodal dewetting and on dewetting by nucleation and growth of holes, but as well, on receding dewetting fronts which are initially straight but develop a transverse fingering instability. One can analyse the dependence of the characteristics of the resulting branching patterns on the driving effective chemical potential (provides a criterion for equilibrium and spontaneity for a system), the mobility and concentration of the nanoparticles, and the interaction strength between liquid and nanoparticles. This allows an understanding of the underlying fingering instability mechanism.

The thesis describes briefly how the combination of a Monte Carlo model with a Genetic Algorithm can be developed and used to tune the evolution of a simulated self-organising nanoscale system toward a predefined non-equilibrium morphology. This work has presented evolutionary computation as a method for designing target morphologies of self-organising nano-structured systems.

Finally, highly localised control of 2D pattern formation in colloidal nanoparticle arrays via surface inhomogeneities created by atomic force microscope (AFM) induced oxidation is presented and some simulations are shown.

Furthermore, the model can be extended further, and by including the second type of nanoparticle, the binary mixture behaviour can be captured by simulation.

Chapter 2

Review of Dewetting Experiments

The process of dewetting consists in the retraction of fluid from a surface which it has covered. Dewetting has an important impact in many technological applications as adhesion [105, 136, 32, 101, 40, 27], lubrication [103, 118], coating applications [35, 17, 137, 71, 57] and other applications in which liquids are applied directly to solid surfaces, but also in a variety of different biological [121, 64] (dewetting in protein folding, dewetting in protein-ligand binding) and many physical systems [16]. It is a process observed in our everyday life and the experiments to study dewetting processes are very attractive due to their rapidity and simplicity, for example, everyone has already observed how a drop slides down on grass's surface, Fig. 2.1. Despite its simplicity with respect to experimental observation it turns out that dewetting is extremely sensitive to quite small changes in the studied system.

Figure 2.1: Water drops sliding down on the surface of grass (photo taken by the author).

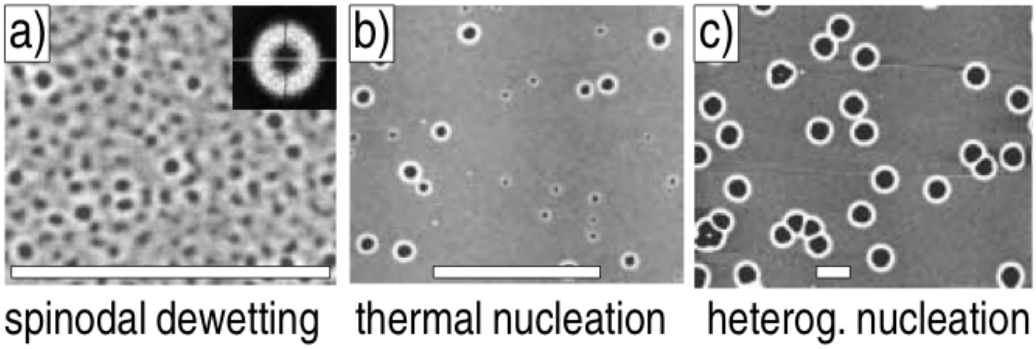

Figure 2.2: Dewetting patterns as observed with AFM. The height scale ranges from black (0 nm) to white (20 nm). (a) spinodal dewetting, (b) homogeneous (thermal) nucleation, and (c) heterogeneous nucleation, (reproduced from [106]).

First we have to understand the underlying mechanism of the dewetting process. This will allow us to determine, for example, the interfacial properties.

In pursuing this, many conduct different kind of experiments on dewetting non-volatile pure liquids, [99, 106], on dewetting and evaporating pure liquids, [33, 34, 62], dewetting and evaporating solutions and suspensions that include different types of solutes, particles and also polymers.

Particularly interesting is the self-organised structure evolution in time and space. Often the basics of dewetting have been studied on liquid films because heterogeneous influences associated with solid films are not as prominent or must not be considered. From the theoretical considerations, dewetting of a metastable liquid film can develop via two different mechanisms, Fig. 2.2. First, nucleation and growth of holes can take place. In general the growth of the holes leads to accumulation of the material along the perimeter of the holes by building up an elevated rim around them. This process has already been studied in detail experimentally, [7]. The second process which can lead to dewetting is based on an instability of the film against thermally activated surface waves [7].

The patterns formed in dewetting processes have attracted strong interest since Reiter analysed the process quantitatively in the early nineties. Reiter et al. [99] used a toluene solution of the polymer (polystyrene) spin coated onto a silicon substrate with dewetting taking place when the films (they use two different non-wettable surfaces) were annealed in a vacuum oven for different times at temperatures above glass transition. The film ruptured in several places, forming holes which subsequently grew, competing for space. As a result, a random polygonal

network of liquid rims emerged. The rims may further decay into lines of small drops due to a Rayleigh-type instability [99, 100, 112]. They show that dewetting of thin films proceeds via three stages: first, the films break up thus creating randomly distributed holes. Second, the holes then grow and the rims ahead of the holes eventually merge forming cellular structures. Third, the resulting ribbons are unstable and decay into droplets. Even if their results are in agreement with some theoretical predictions, there are at least two questions which remain unanswered. One of them is related to the detailed mechanism creating almost regular patterns although the initial holes are distributed randomly and the second one is how the surface modulations evolve before the film breaks up. The related problems of retracting contact lines on partially wetting substrates and the opening of single holes in rather thick films have also been studied [22, 11].

Lipson and Elbaum [33, 34, 62] study drying water films where they considered also the evaporation process coupled with dewetting. They conducted experiments with a thick water film which is deposited on a mica substrate at low temperature. The external pressure is reduced, so the water evaporates. However, it does not do so homogeneously. Due to the fact that water recedes from the hole, a moving rim of water is created around the hole which becomes unstable producing a pattern of water drops. The experiments are done for both homogeneous and heterogeneous nucleation. The effect has been observed as well for other fluids on wetted substrate, so it is not specific to water on mica substrate.

Additional work has mainly focused on many different aspects of the dewetting process for simple non-volatile liquids and polymers, [78, 108, 124]. All stages of the dewetting of a film are studied: the initial film rupture via nucleation or a surface instability (called spinodal dewetting) [99, 138, 106, 131, 6, 3], the growth process of individual holes [98, 107, 36], the evolution of the resulting hole pattern [112, 3], and the stability of the individual dewetting fronts [12, 102, 81].

Sharma and Reiter, [112] give experimental results on instabilities and various stages of dewetting of thin ($< 60nm$) films on coated substrates. Thin ($> 10nm$) polystyrene films, prepared on silicon wafers with three different nano-sized (about 1 nm) coatings, dewet spontaneously above the glass transition temperature by the growth of cylindrical holes with "wavy" rims. They could clearly distinguish, and theoretically explain, four different stages as dewetting proceeded: (a) rupture of the film; (b) expansion and coalescence of holes to form a polygonal "cellular" pattern; (c) disintegration of polymer ridges forming the polygon into spherical drops due to Rayleigh instability; and (d) fingering instability of hole rims during hole expan-

sion witnessed only on low wettability coatings.

Reiter et al. [101] use dewetting to understand the properties of a polymer melt which is slipping on a layer of identical molecules, end-grafted to a silicon substrate (polymer brush). The interesting questions which arise here are: which are the implications of autophobic behaviour between grafted and free polymers for dewetting and what is the value of the friction coefficient at polymer-polymer interface. They concluded that polymers can not only dewet but also slip on their own brush due to autophobicity.

A number of experiments has been performed employing dewetting processes of solutions and suspensions which can contain nanoparticles or macromolecules like collagen [72, 73, 67, 10].

Mertig et al. [72] study the dewetting process of an evaporating precursor film. The thin monomeric collagen films which is prepared by spin coating on hydrophobic substrates is investigated by scanning force microscopy. The precursor consists of collagen monomers dissolved in acetic acid. Films with an initial thickness of about $10\mu m$ are prepared by spin-coating on a flat substrate. Evaporation of the solvent causes a decrease in the film thickness with time. During drying, the film ruptures and pores are formed. They conclude that pattern formation takes place as the result of dewetting of the liquid precursor initiated by pore nucleation in the drying film. The growth of pores leads to an accumulation of collagen monomers along the perimeter of the dry patches formed. Different well-defined film morphologies have been observed depending on the evaporation velocity of the solvent.

More recently, Reiter et al. [39] showed experimental results on the dewetting behaviour of thin polymer films (polydimethylsiloxane, PDMS) supported by silicon wafers which were coated with a layer of end-grafted PDMS molecules, on smooth non-wettable silicon substrates. In the second part, they replaced the PDMS films by polystyrene (PS) films of different molecular weights. Dewetting of PS films was induced by heating of the sample on a nitrogen- purged hot stage above the glass transition temperature. The presented experiments demonstrate that dewetting represents also a powerful approach for a sensitive characterisation of rheological, frictional and interfacial properties of thin polymer films.

In the previous paragraphs is given a very short overview over different experimental setups, from experiments with pure, classical simple liquids, without evaporation, to more complex experimental setups where dewetting process and also decomposition and evaporation take place.

More recently, interest has turned to the dewetting processes of solutions and suspensions.

In the next paragraphs we discuss different setups for experiments which involve dewetting, solvent evaporation and as well the presence of nanoparticles. However, there is no in depth investigation of these systems. The mentioned systems are complicated because their behaviour is an interplay between the various solute and solvent transport processes. Also, usually the solvents used evaporate, so, there has to be a distinction between "normal" convective dewetting and evaporative dewetting. A number of experiments have been performed employing macromolecules like collagen (see above described experiment of Mertig et al.) and DNA [73, 72, 127, 66, 114, 140], nanoparticles [68, 41, 77, 95, 46, 69, 70, 116, 91] and solution of polymers [56, 47, 50, 63].

Moriarty et al. [77] showed that under appropriate conditions, Au nano-crystals (dispersed in either a toluene or a hexane solvent) on silicon form cellular networks. Using statistical crystallography they showed that nano-structured foams are structurally distinct from a variety of prototypical froths and also demonstrated that mechanisms based solely on Marangoni convection fail to explain many aspects of cellular network in nanocrystal systems. So, Au nano-crystals form cellular networks on silicon surfaces and Marangoni convection alone cannot explain the various foams and patterns they observed. Nanocrystal foams are far from statistical equilibrium due to the imposition of a specific intercellular wavelength that dominates network evolution.

Ge and Brus [41] studied nanocrystal aggregation patterns and kinetics on smooth graphite (HOPG) using an AFM, both under organic liquid and after drying of thin wet films. Aggregates of a few nano-crystals form and then dissolve, most nano-crystals are monomers. The nano-crystals seem to form a single lattice gas fluid phase on the smooth HOPG surface. Very regular bicontinuous patterns, whose length scale increases with time, are observed when the particle coverage is higher, about 20-30%. These patterns are similar to spinodal decomposition patterns observed when a high temperature, single fluid phase polymer blend is quenched below its critical temperature and begins to phase separate.

Karthaus et al. [56] shown that by a simple casting process from a solution (polystyrene, a nonpolar polymer, dissolved in benzene), regular arrays of micron-sized mesoscopic polymer aggregates could be formed. The driving force for this self-organisation of polymers into a superstructure are dissipative structures that occur in the solution and especially at the three-phase-line, contact line between solid, liquid and gas phase. To get a deeper insight into the formation mechanism of such an ordered array, evaporation of a polystyrene solution was ob-

served in situ by optical microscopy. A few seconds after placing the polymer solution onto the substrate (best results were obtained by using hydrophilic substrates, such as glass, quartz, silicon or mica) the equilibrium size of the droplet has been established, and the effect of solvent evaporation becomes evident. The volume of the solution becomes smaller with ongoing evaporation of the solvent, and the size and shape of the polymer aggregates depend on the solvent, evaporation speed, concentration, three-phase-line velocity, temperature, etc.

Hong et al. [50] discussed spontaneous formation of well organised mesoscale polymer patterns during the course of solvent evaporation by constraining polymer solutions in a sphere-on-Si geometry. Their approach opened up a new way for producing yet more complex patterns in a simple, controllable, and cost effective manner by allowing a drop to evaporate in a sphere-on-Si geometry, where the interfacial interaction between the solute and the substrate effectively mediate the pattern formation.

The latest experiments discussed above, employing nanoparticles are sometimes referred to as "nano-fluids". Polygonal networks or/and labyrinthine structures result from spinodal dewetting and heterogeneous nucleation and growth, respectively. One may find strongly ramified structures in all three systems [122, 47, 91, 63]. A selection of images exhibiting some of the possible structures is displayed in Fig. 2.6 and Fig. 2.8.

The main work of this thesis focuses on the theoretical reproduction of this kind of systems (experiments that use monodisperse colloidal suspensions of thiol-passivated gold nanoparticles in toluene [41, 77, 69, 70, 90, 91, 116]). Kinetic Monte Carlo simulations are used to obtain the patterns obtained experimentally (nucleation process, spinodal decomposition and as well branching patterns).

The system studied is a solution of gold nanoparticles which are suspended in toluene. The 2 or 3 nm gold core is covered by alkyl-thiol molecules, Fig. 2.3, whose carbon chain length can be changed from C_6 to C_{12} [91]. Varying the length of the chain allows control of the interaction parameters (we will discuss the correspondence with our interaction parameters used in the simulation model, in the next section).

The particles can be hydrophobic (in this case they are suspended in toluene), or they can be hydrophilic by modifying the termination of the passivating alkyl-thiol molecules, (they will be suspended in water or in another polar solvent). The experiments are done, in general using hydrophobic particles.

The standard procedure is the following: The nanoparticles are deposited onto a substrate,

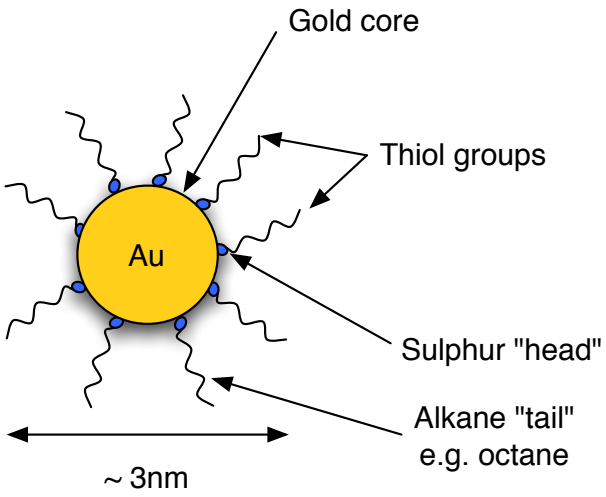

Figure 2.3: A schematic structure of a thiol-passivated gold nanoparticle.

at the surface of which the self-assembly process takes place. Depending on the experimental conditions one can observe/obtain a broad range of patterns. In order to change the affinity between the solution and the substrate, the properties of the substrate can also be modified. The solution can also be modified if there is a need to have a better control over evaporation. The wetting behaviour of the solvent can be modified (locally) by oxidising the substrate further [70].

The goal is to obtain exactly the patterns wanted on a specific type of substrate. To do that, it is necessary to find the best experimental conditions. All the parameters mentioned above contribute to form patterns.

The next step after sample preparation is the investigation by atomic force microscopy (AFM). It shows a variety of patterns which depend the concentration of the solution (see Fig. 2.6 and Fig. 2.8). For low concentration, it is possible to obtain fractal patterns and if the concentration and coverage is increased, cellular networks and ribbon structures are obtained. The deposition process is very important to determine the evaporation speed and it has a strong influence on the final pattern. Two procedures are used as described as follows.

2.1 Spin coating method

A thin film of solution is deposited by spin-coating a drop of solution onto a solid substrate. Evaporation of solvent plays an important role in this kind of experiment. The evaporation of solvent competes with dewetting as was described first in Ref. [127] for a related system

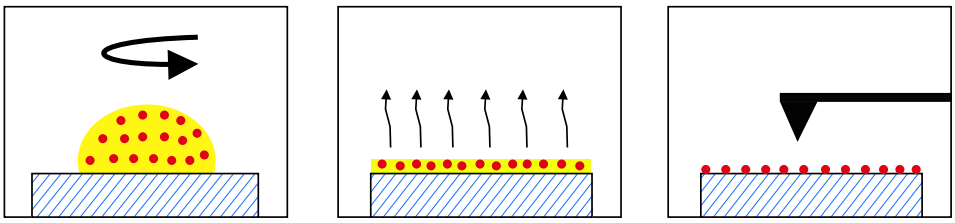

Figure 2.4: A schematic representation of the spin coating technique.

involving a solution of macromolecules. After all solvent has evaporated the final structure is analysed by atomic force microscopy. A schematic representation of this process is given in Fig. 2.4. Depending on the concentration of the initial solution one may find fractal patterns, cellular networks and ribbon structures (see Fig. 2.6 and Fig. 2.8). Note that for spin-coated films the evaporation is quite fast if the experiment is not performed under controlled humidity.

The parameters for this experiment are: humidity, temperature (they are normally not controlled by experiment, experiments use ambient temperature and humidity), the concentration of nanoparticles and the wetting properties of substrate.

2.2 Meniscus technique

With the first method just introduced, the evaporation of the solvent is not well controlled. To improve the control a meniscus technique using a teflon ring was introduced [90] to decrease the solvent evaporation rate during nanoparticle self-organisation. For a solvent with appropriate wetting properties, such as toluene, a Teflon ring can be used for creating a meniscus of solution rather than a drop, Fig. 2.5. The affinity of the solvent with Teflon is higher than that with silicon oxide (considering native oxide-terminated silicon substrates) hence the formation of a meniscus. As the solvent evaporates, it now retreats from the centre of the sample towards the edge of the ring. The rate of evaporation in this configuration is mainly dictated by the capillary forces related to the presence of the Teflon ring.

As mentioned above, the difference for this method is that the affinity of toluene for teflon is higher than that for silicon oxide, which means that the solvent will dry quickly (a few seconds) from the centre of the ring. It will take a long time, maybe one hour and more, to evaporate near to the edge of the ring. In the first case (where we used a droplet of solution) the solvent evaporates at the beginning from the edges to the centre. At the centre the evaporation rate is

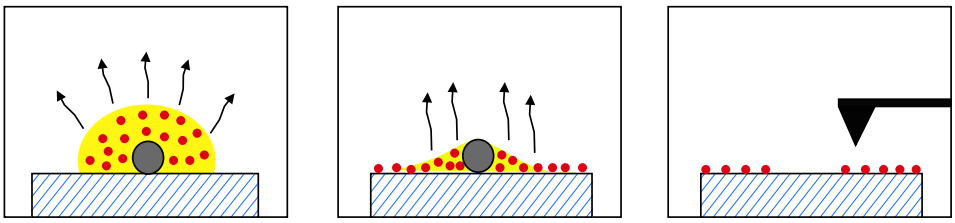

Figure 2.5: Sketch of the meniscus technique.

increased and will result in many particles being pinned to the surface simultaneously.

The meniscus technique allows for the study of branched structures in a more controlled manner. The work done in Ref. [91] indicates that fingering strongly depends on the interaction strength of the particles, i.e., on the chain length of the thiol molecules coating the gold cores, (for details see Ref. [91]).

In Fig. 2.6 and Fig. 2.8 are shown AFM images of patterns of gold nanoparticles using the experimental techniques described above. Fig. 2.7 shows three images of strongly ramified dewetting structures obtained using atomic force microscopy for different systems.

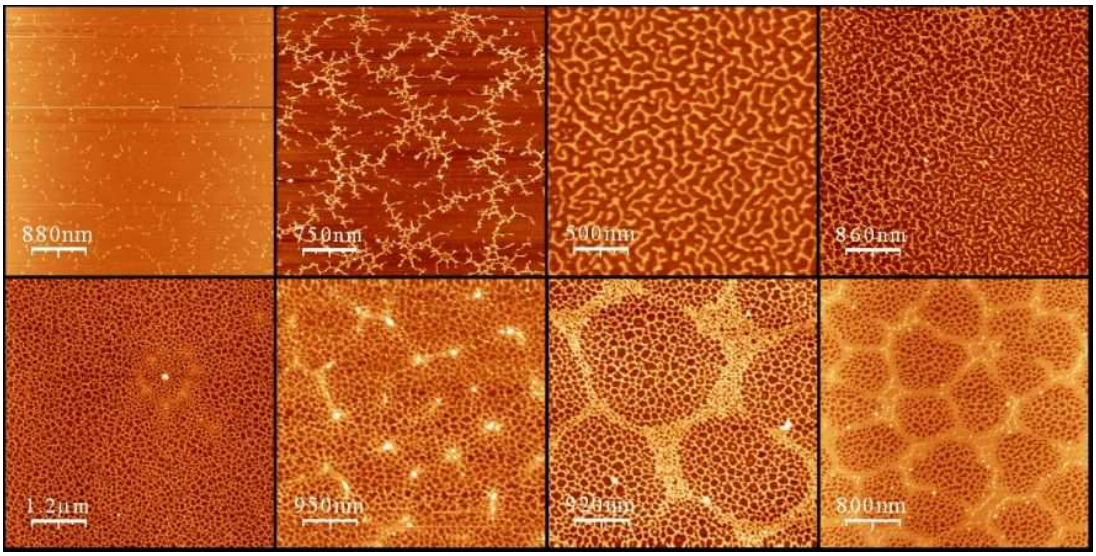

Figure 2.6: Atomic Force Microscopy images of patterns of gold nanoparticles. From top left to bottom right, concentrations increase as follows: 0.10 mg/ml, 0.25 mg/ml, 0.50 mg/ml, 0.75 mg/ml, 1.00 mg/ml, 1.25 mg/ml, 1.50 mg/ml and 1.75 mg/ml. Scans are 2 to $5\mu m$ in size (courtesy of Matthew Blunt, Nottingham University).

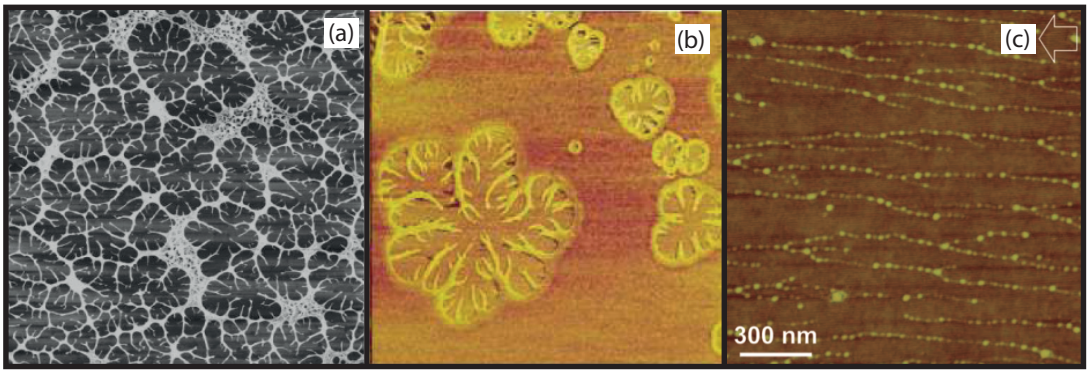

Figure 2.7: Images of strongly ramified dewetting structures obtained using atomic force microscopy in the case of (a) an aqueous collagen solution on graphite, image size $5 \times 5\mu m^2$, (b) polyacrylic acid in water spin coated onto a polystyrene substrate, image size $2.5 \times 2.5\mu m^2$ (images taken from [130], cf. also [122]) and (c) represents an AFM image of 1% polyacrylic acid (PAA) after droplet evaporation on the PS surface. The units of the two dimensions are micrometers, and the height scale is 20 nm. The moving direction of the contact line is from right to left, as denoted by the arrow in the top right corner (image taken from [63]).

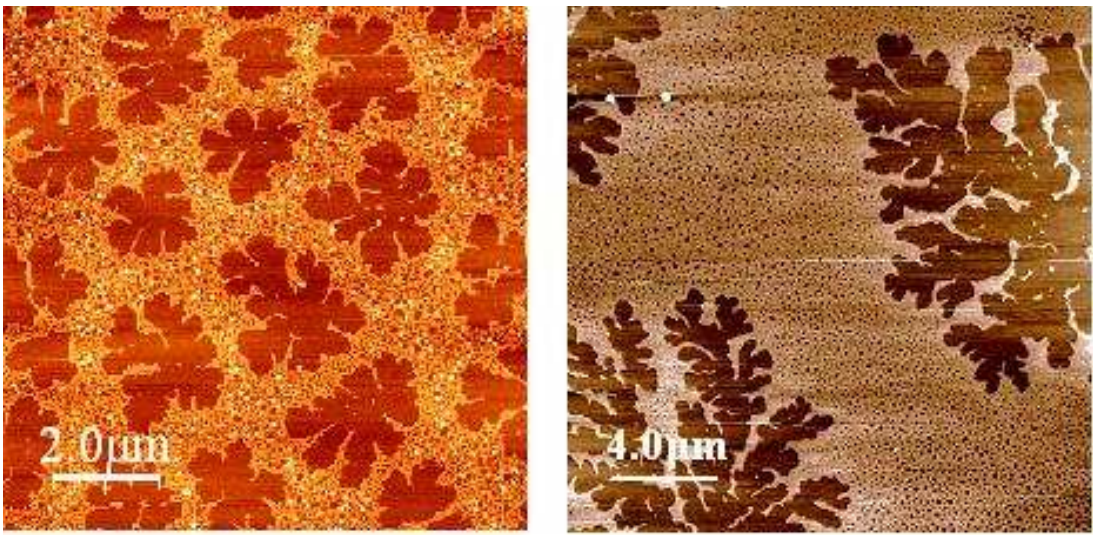

Figure 2.8: AFM pictures of viscous fingering patterns in the case of (a) spin-coated solution of gold nanoparticles onto silicon (scan size $10 \times 10\mu m^2$, and (b) solution deposited using the meniscus technique (scan size $20 \times 20\mu m^2$) (courtesy of Matthew Blunt, Nottingham University).

Chapter 3

Theoretical Approaches

3.1 Overview

Different theoretical approaches are developed to study a thin film of solution which is deposited by spin-coating a drop of solution onto a solid substrate. In order to have a complete overview and understanding of the behaviour of thin films it would be useful and necessary to have theoretical and computational tools that will cover the details to the atomic scale and to describe and explain, as well, a coarse grained description provided by continuum equations. Over time, much effort has been done to combine the traditional methodologies such as density functional theory, molecular dynamics, Monte Carlo methods with mesoscopic continuum descriptions into a more complete and unified multiscale framework (cf. Fig. 3.1).

The most convenient approach is the formulation of the model in terms of nonlinear partial differential equations. Of course that this method works just in some cases, for example, on the mesoscopic scale, continuum models using Navier-Stokes equations with no-slip or slip boundary conditions at the substrate work only in a limited range of film thicknesses. Density function methods provide a quantum mechanical description of electrons and nuclei, which is appropriate for processes such as chemical reactions and crack formation or surface kinetics. Continuum equations provide a reduced description in terms of continuous fields for the coarse-grained evolution of the system. Monte Carlo methods are especially useful for obtaining statistical information about a system from the transition rates between configurations, whether in equilibrium or driven away from equilibrium.

In order to describe various aspects of material behaviour with the ultimate goal of systematically coupling the atomistic to the continuum descriptions we have to employ and compare

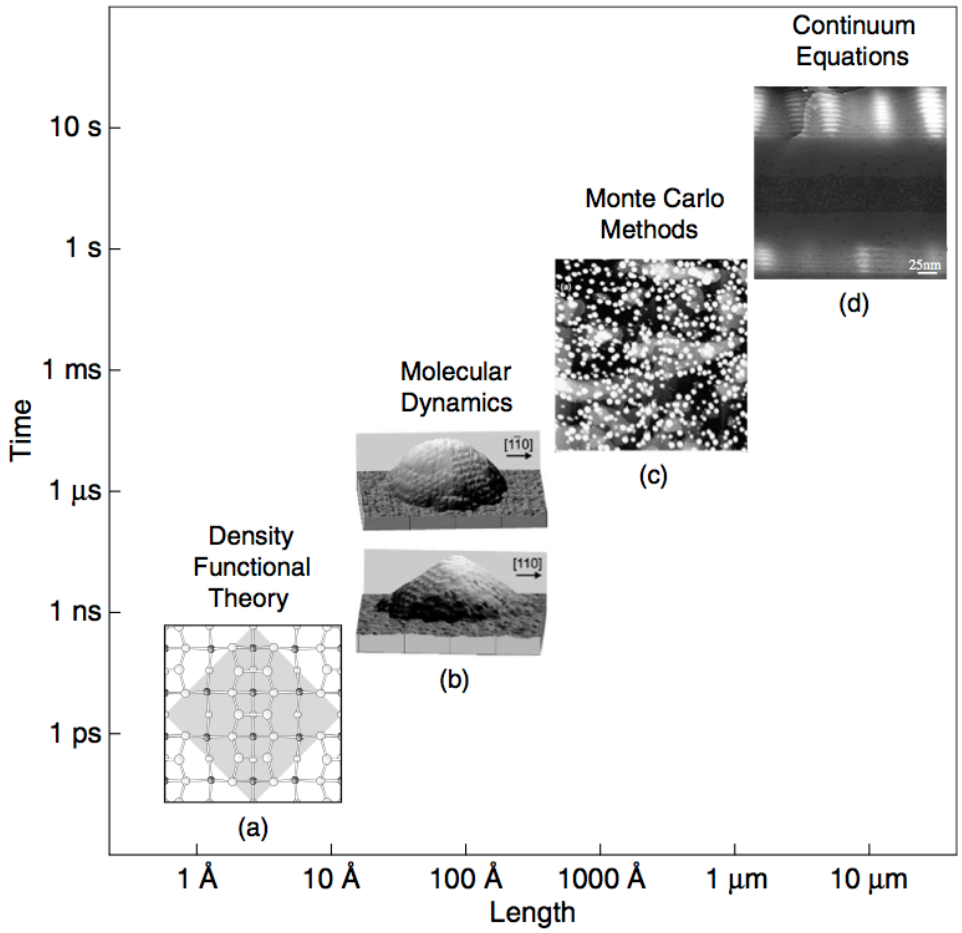

Figure 3.1: A hierarchy of modelling methods, (reproduced from [135]): (a) The c(4x4) phase (reconstruction) of the GaAs(001) surface that is the most common substrate for the growth of quantum dots. The unit cell is indicated by the shaded region, (b) Atomically resolved scanning tunnelling microscopy (STM) images (200x200 A^o), (c) An STM image (500x500 nm) of an ensemble of three-dimensional islands on GaAs(001) and (d) A (200x200 nm) section of a large-scale cross-sectional image showing five- and ten-period superlattices of InAs/GaAs quantum dots (bright regions).

different methods. That is the reason why in the present chapter a brief introduction is given to theoretical approaches and after that, we discuss our results in the context of a kinetic Monte Carlo approach in a two-dimensional model [95, 69, 120] which is found to give useful results and estimates in agreement with the experiments [70, 91]. Lattice-based techniques such as Monte Carlo (MC) simulations, and other probabilistic molecular models are necessary to introduce because as it was mentioned already above, under certain film thicknesses the solvent dynamics is dominated by evaporation and it is necessary to find alternative models.

In the next sections of this chapter an overview on thin film theory for pure liquids is given and also a short description of the Cahn-Hilliard equation for decomposition of a mixture. In the following chapters the discrete model is introduced and the results from it discussed.

3.2 The thin film theory for pure liquids

3.2.1 General approach

In principle, all situations which involve a single liquid layer on a solid substrate (see Fig. 3.2), are governed by the Navier-Stokes equations with adequate boundary conditions at the substrate and the free surface, the liquid-gas interface. At the substrate one usually applies the no-slip condition, [88, 124]. In some cases a variety of different slip conditions are used, for example, the Navier slip condition [80, 36, 82].

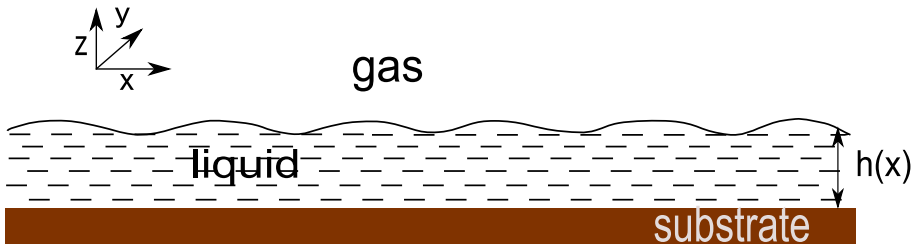

Figure 3.2: Sketch of a liquid film on a horizontal substrate.

In thin films, the velocities parallel to the substrate are large compared to the ones orthogonal to the substrate and the gradients orthogonal to the substrate are large compared to the ones parallel to the substrate. This allows the simplification of the governing equations using the long-wave or lubrication approximation [88].

To describe the time evolution of the film thickness profile, a kinematic boundary condition is used at the free surface.

A liquid layer sitting on a solid substrate is modelled using an evolution equation for the film thickness profile $h(\vec{x},t)$, which can be derived from the Navier-Stokes equations using the long-wave approximation.

$$\partial_t h = -\nabla \cdot \left[\frac{h^3}{3\eta} \nabla (\gamma \nabla^2 h + \Pi(h)) \right], \tag{3.1}$$

where γ and η are the surface tension at the liquid/gas interface and the viscosity of liquid, respectively. $\gamma\nabla^2 h$ represents the Laplace or curvature pressure. The operator ∇ is two dimensional, i.e.

$$\nabla = \begin{pmatrix} \partial_x \\ \partial_y \end{pmatrix}$$

The last term, $\Pi(h)$, a pressure term, is called disjoining or Derjaguin pressure [117] and includes the effective molecular forces between substrate and film surface (all wettability effects). It was first introduced by Derjaguin [26, 27]. The disjoining pressure can lead to film rupture. The disjoining pressure can incorporate electrostatic or van der Waals interactions, depending on the particular problem at hand. Usually it is a combination of short and long range components, described by power and/or exponential laws. The disjoining pressure can be written as the derivative of a local free energy $f(h)$

$$\Pi(h) = -\frac{\partial f}{\partial h}, \tag{3.2}$$

a formulation often used in what follows.

There are different expressions for disjoining pressure, a variety of different combinations of stabilising or destabilising exponentials and power laws are used, one offer advantages over the others, depending on the system studied. We will not discuss the details of them, but only list some usual expressions, in dimensionless form:

$$\Pi(h) = \frac{1}{h^3} - \frac{1}{h^6}, [22] \tag{3.3}$$

$$\Pi(h) = 2ke^{-h}(1 - e^{-h}) + Gh, [93] \tag{3.4}$$

$$\Pi(h) = \pm \left(-\frac{b}{h^3} + e^{-h} \right), [110,\ 111,\ 109] \tag{3.5}$$

Eq. (3.3) uses a combination of polar short-range destabilising and apolar (Lifshitz - Vander-Waals) long range stabilising interactions that is widely used in the literature [26, 111, 110, 109].

The first term of Eq. (3.4) was derived by Pismen and Pomeau [93] combining the long wave approximation for thin films [88] with a diffuse interface model for the liquid-gas interface [1]. The second term represents the hydrostatic pressure. Eq. (3.4) has the advantage of remaining finite even for vanishing film thickness. The parameter G is normally very small, however it is possible to study the qualitative system behaviour using a small but not very small G.

Eq. (3.5) is another interesting expression that combines a long-range apolar van der Waals interaction and a short-range polar (electrostatic or entropic) interaction [22, 109, 110, 111]. If the positive sign is used, the two disjoining pressures (Eq. (3.3) and Eq. (3.5)) lead to qualitatively very similar results [129, 128].

The disjoining pressure can be calculated for specific intermolecular interactions. Assuming a long-range apolar van der Waals interaction, S_{AP}, one finds

$$\Pi_{vdW}(h) = \frac{2S_{AP}d_0^2}{h^3} \tag{3.6}$$

For a short-range polar interaction,S_P, (like, for instance, arising from the interaction of the electric double layers in a thin film of an electrolyte) one finds

$$\Pi_p(h) = \frac{S_P}{l}e^{(d_0-h)/l} \tag{3.7}$$

So, the disjoining pressure containing a short range polar destabilising force (the second term in Eq. (3.8)) and a long range apolar stabilising force (the first term in Eq. (3.8)) is given by:

$$\Pi(h) = 2S_{AP}\frac{d_0^2}{h^3} + \frac{S_P}{l}e^{[(d_0-h)/l]} \tag{3.8}$$

where $d_0 = 0.158nm$ is the Born repulsion length, and l is the correlation length for polar interactions. S_P and S_{AP} are the polar and apolar components of the total spreading coefficient, S, which is given by

$$S = S_{AP} + S_P = \gamma(\cos\theta - 1), \tag{3.9}$$

where θ is the macroscopic contact angle (see Fig. 3.3).

The contact angle represents the angle between the solid substrate and the liquid/gas interface in the vicinity of the three phase contact line. Fig. 3.3 sketches schematically this situation. The equilibrium contact angle θ is given by the Young-Laplace equation:

$$\gamma_{lg}\cos\theta = \gamma_{sg} - \gamma_{sl}, \tag{3.10}$$

and is related to the spreading coefficient by Eq. (3.9). γ_{lg}, γ_{sg} and γ_{sl} represent the surface tensions of the liquid/gas, solid/gas and solid/liquid interfaces, respectively. If we are using the

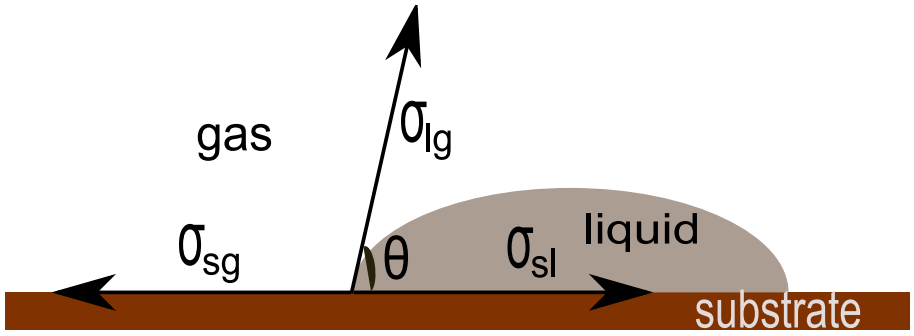

Figure 3.3: Macroscopic contact angle θ in the Young-Laplace equation: γ_{lg}, γ_{sg}, γ_{sl} denote the surface tensions of the liquid/gas, solid/gas and solid/liquid interfaces, respectively.

macroscopic contact angle we can distinguish three different wettability regimes. The special case is called complete wetting when $\theta = 0$. In this case the liquid forms a flat film on the surface. The second case is when $0 < \theta < \pi$ which is called partial wetting and the last is the case with $\theta = \pi$ which is called non-wettable (see Fig. 3.4).

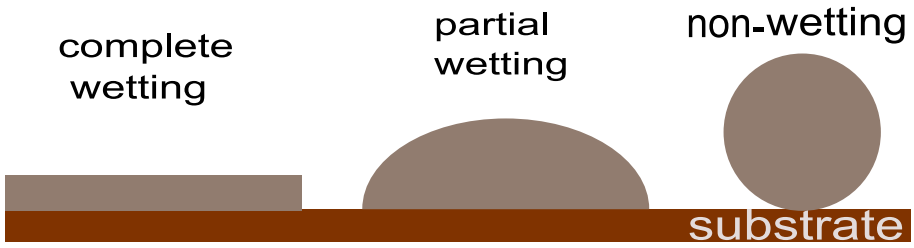

Figure 3.4: A schematic image showing the different wettability regimes.

If we introduce the ratio of apolar and polar interaction $b = 2S_{AP}d_0^2/S_P l^2 e^{d_0/l}$ and assumed $S_{AP} > 0$ and $S_P < 0$, then we can plot the disjoining pressure over film thickness for different values for the ratio of the effective molecular interactions b. The corresponding plot is given in Fig. 3.5. In this situation we can obtain from Eq. (3.1) the dimensionless evolution equation for the thickness profile h

$$\partial_t h = -\nabla \cdot \left\{ h^3 \nabla \left[\nabla^2 h + \frac{b}{h^3} - e^{-h} \right] \right\}, \tag{3.11}$$

where $\Pi(h)$ is the rescaled disjoining pressure given by

$$\Pi(h) = \frac{b}{h^3} - e^{-h} \tag{3.12}$$

which was introduced before. The scaling that we used to non-dimensionalise the evolution equation for the thickness profile h is shown in the Appendix A.

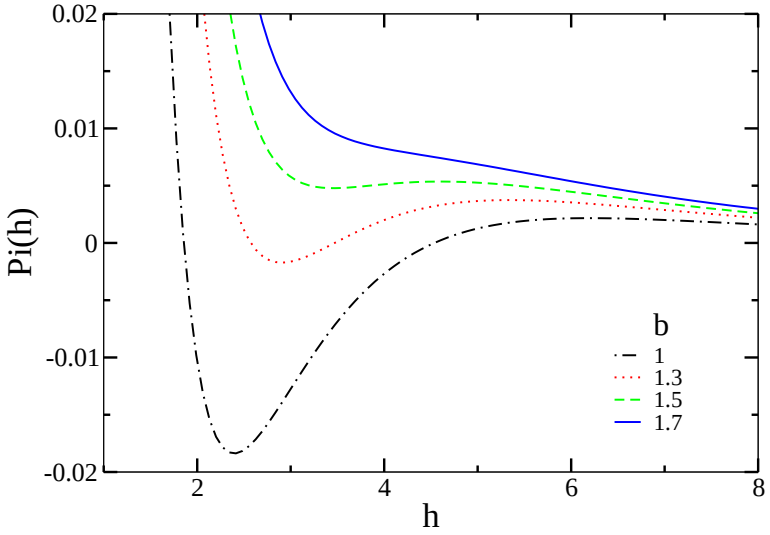

Figure 3.5: The disjoining pressure, Eq. (3.5), for different values of the ratio of apolar and polar interactions b.

The next step, after introducing the dimensionless form of thin film evolution equation and discussing different variants of disjoining pressure is to study its linear stability which will be discussed in detail in the next section.

3.2.2 Linear stability of flat film

The linear stability analysis give us information about the initial stages of the dynamics of the system for an infinitesimal perturbation. Here, in this section, we give an overview of the linear behaviour of thin film equation, Eq. (3.11). Only the linear stability for a flat film solution is discussed and we will analyse under which conditions the flat film solution can become unstable to infinitely small perturbation. First, the simple 1-dimensional case is discussed and after that, for completeness, the more general 2-dimensional case is shown.

The film thickness evolution equation for a liquid layer on a horizontal substrate in a general form is:

$$\partial_t h = -\partial_x \{Q(h)\, \partial_x [\partial_{xx} h - \partial_h f(h)]\} \tag{3.13}$$

where $Q(h)$ is a mobility factor, that in Eq. (3.11) is $Q = h^3$.

To discuss the linear stability of flat films ($h(x) = h_0$), one uses a Fourier mode decompo-

sition of a general perturbation.

$$h(x,t) = h_0 + \epsilon\, e^{\beta t + ikx} \tag{3.14}$$

where β and k give the growth rate and the wave number of the disturbance mode and ϵ is the small amplitude. The next steps is to linearize the full time dependent thin film equation.

Considering the above assumptions, we Taylor expand in $\epsilon \ll 1$ every term in Eq. (3.13), e.g.,

$$\partial_h f(h) \approx \partial_h f(h_0) + \epsilon \partial_h^2 f(h_0)\, e^{\beta t + ikx} \tag{3.15}$$

$$Q(h) \approx Q(h_0) + \epsilon \partial_h Q(h_0) e^{\beta t + ikx} \tag{3.16}$$

After some algebra we collect terms of $O(\epsilon)$ and obtain the equation for growth rate β:

$$\beta = -Q(h_0)k^2[k^2 + \partial_h^2 f(h_0)] \tag{3.17}$$

which is plotted in Fig. 3.6 for case $k > 0$.

The flat film is unstable for $\beta > 0$ and the critical wave number is given by

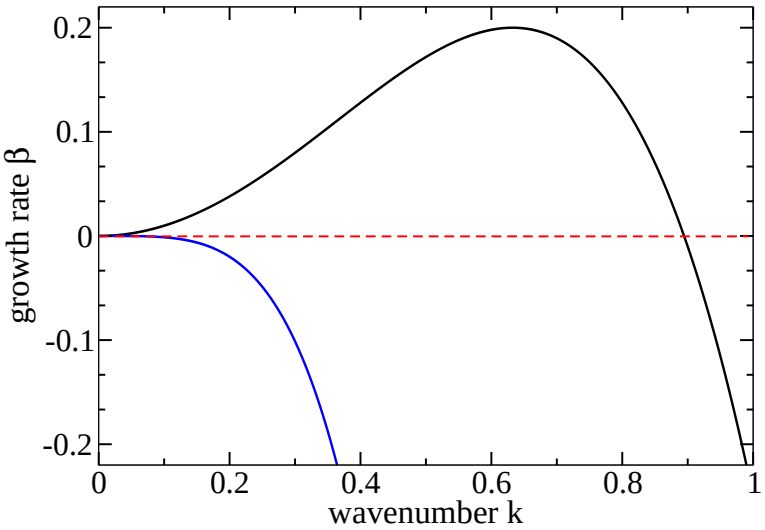

Figure 3.6: Dispersion relation, Eq. (3.17), giving the growth rate β in dependence of the wave number k of harmonic perturbations for a flat film on a horizontal homogeneous substrate: the black line represents the unstable case whereas the blue curve shows the stable case, for the generic form $\beta = -k^2(k^2 - k_c^2)$. The wave number is given in units of k_c

$$-Q(h_0)k_c^2[k_c^2+\partial_h^2 f(h_0)]=0 \quad \Rightarrow \quad k_c=\pm\sqrt{-\partial_h^2 f(h_0)} \tag{3.18}$$

and the corresponding critical wavelength is $\lambda_c = 2\pi/k_c$. At k_c, the thickness profile $h_0+\epsilon e^{ik_c x}$ with $\epsilon \ll 1$ is marginally stable and represents a small amplitude periodic steady solution of Eq. (3.13).

The wavelength of the fastest growing mode for a linearly unstable film is $\lambda_m = \sqrt{2}\lambda_c$ and has the growth rate

$$\beta_m = \frac{1}{4}Q(h_0)[\partial_{hh} f(h_0)]^2 \tag{3.19}$$

Above is discussed one dimensional case, but a description of linear stability for thin film equation can be given as well in a general way. In the 2-dimensional case, one can follow the same procedure as above, so here are the details, just for completeness.

In two-dimensional case we can write the thin film evolution equation:

$$\partial_t h = -\nabla\{Q(h)\nabla[\triangle h - \partial_h f(h)]\}, \tag{3.20}$$

The corresponding Fourier mode decomposition (ansatz):

$$h(x,y,t) = h_0 + \epsilon\, e^{\beta t + ik_x x + ik_y y} \tag{3.21}$$

The terms in the thin film equation are Taylor-expanded as, e.g.

$$Q(h) = Q(h_0) + \epsilon\partial_h Q(h_0)W$$

$$\partial_h f(h) = \partial_h f(h_0) + \partial_h^2 f(h_0)\epsilon W$$

$$\triangle h = (\partial_{xx}+\partial_{yy})h = -\epsilon(k_x^2+k_y^2)W$$

with

$$W = e^{\beta t + ik_x x + ik_y y}.$$

With these notations we can calculate $\partial_t h$, finally, obtaining the equation for growth rate β, plotted in Fig. 3.7:

$$\beta = -Q(h_0)(k_x^2+k_y^2)\left[(k_x^2+k_y^2)+\partial_h^2 f(h_0)\right] \tag{3.22}$$

In the two dimensional case we have for the critical wave number k_c:

$$k_c^2 = -\partial_{hh}^2 f(h), \tag{3.23}$$

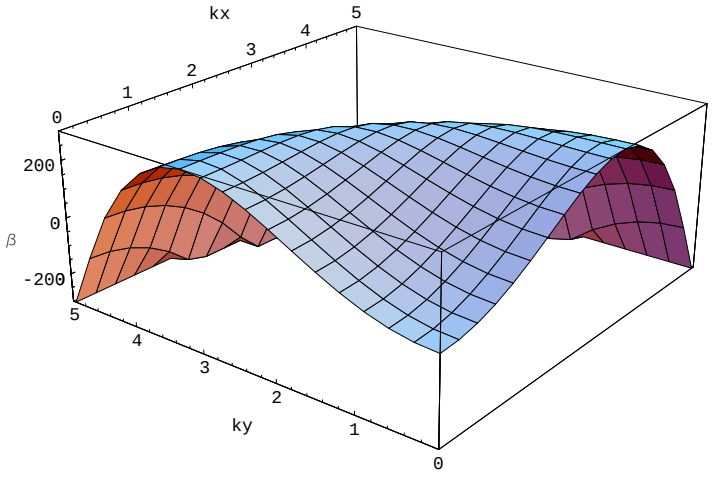

Figure 3.7: Dispersion relation, Eq. (3.22), giving the growth rate β in dependence of the wave number k_x and k_y of harmonic perturbations for a flat film on a horizontal homogeneous substrate for the two dimensional case.

with

$$k_c^2 = k_x^2 + k_y^2, \tag{3.24}$$

i.e. all modes with wave vectors (k_x, k_y) inside a circle of radius k_c are linearly unstable.

3.2.3 Stationary solutions of thin film equation

If we consider droplets which coexist with a thin precursor film it is possible to find stationary solutions for the thin film equation. This type of solutions can be calculated using continuation techniques, e.g. using periodic boundary conditions and fixing the average film thickness. This section does not cover all the details about stationary solutions of thin film equation, only a very short overview is given. More information can be found in Ref. [131, 132, 129, 125].

As disjoining pressure, in this case, we use a combination of polar short-range destabilising interaction and apolar (van-der-Waals) long-range stabilising interaction [22, 94]:

$$\Pi(h) = \frac{1}{h^3} - \frac{1}{h^6} \tag{3.25}$$

Using Auto2000 (a software package used for continuation and bifurcation problems in ordinary differential equations), we can calculate stationary solutions corresponding to droplets on a horizontal substrate. Using continuation in parameter space, we follow a family of solutions by changing the "period" and fixing the mean film thickness. It is as well possible to keep the period fixed and change the mean film thickness.

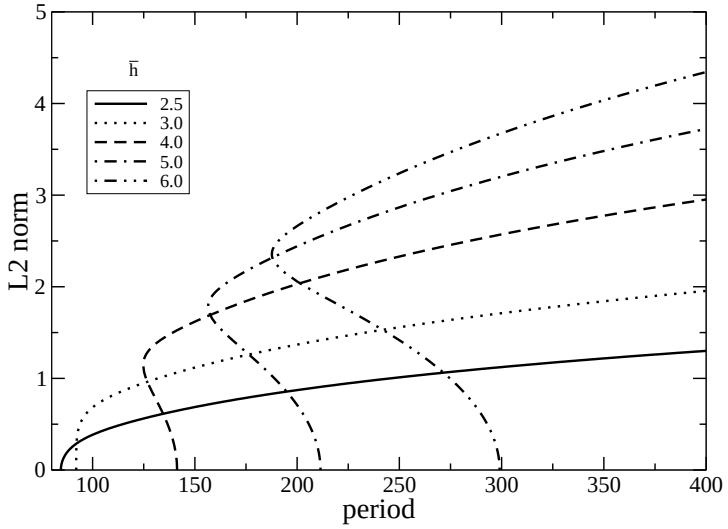

Figure 3.8: L_2-norm of periodic drop and nucleation solutions in dependence of the period for different values of mean film thickness $\overline{h}$, with $b = 0.2$.

In order to define these families, we plotted L2-norm, $||\delta h|| = [(1/L)\int_0^L (h(x) - h_0)^2 dx]$, Fig. 3.8, and the energy, $E = [(1/L)\int_0^L F(h)dx]$, in dependence of the period for different fixed mean film thicknesses as given in the legends, Fig. 3.9, where L is system size [84, 89, 75]. Plots for amplitude over period closely resemble the ones for the L2-norm over period. We choose the film thickness in the linearly unstable regime.

Looking at Fig. 3.8 and Fig. 3.9 it is possible to distinguish two regions:

1. there is only one branch of stationary solutions. Increasing the period, the amplitude increases and energy decreases monotonically. This types of solution families can be found in the linearly unstable solution range, that is away sufficiently from the spinodal line.

2. there are two branches of stationary solutions. In this case the amplitude goes to zero when the period is increased. This type of solution families can be found in the linearly unstable solution range, that is very close to the spinodal line.

There is a third case, which is shown in Fig. 3.10 for mean film thickness larger then 6 ($\bar{h} = 14$ in figure), for metastable flat thin film, where exist two branches of periodic solutions which continue to infinite period. In this situation the flat film is metastable and nucleation

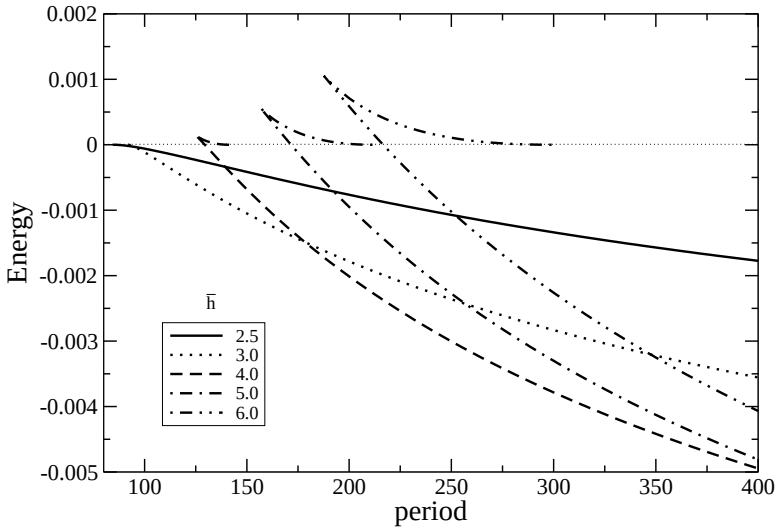

Figure 3.9: Energy of periodic drop and nucleation solutions in dependence of the period for different values of mean film thickness $\overline{h}$, with $b = 0.2$.

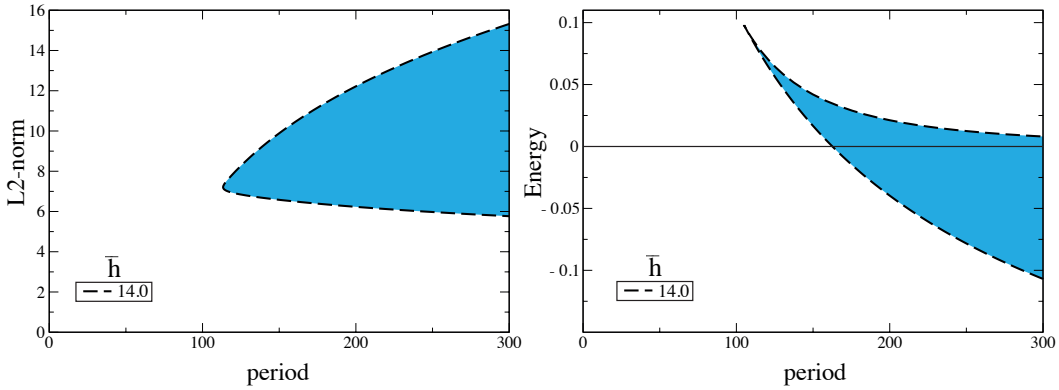

Figure 3.10: L_2-norm and energy in dependence of the period for large mean film thickness, for metastable flat thin film, with $b = 0.2$.

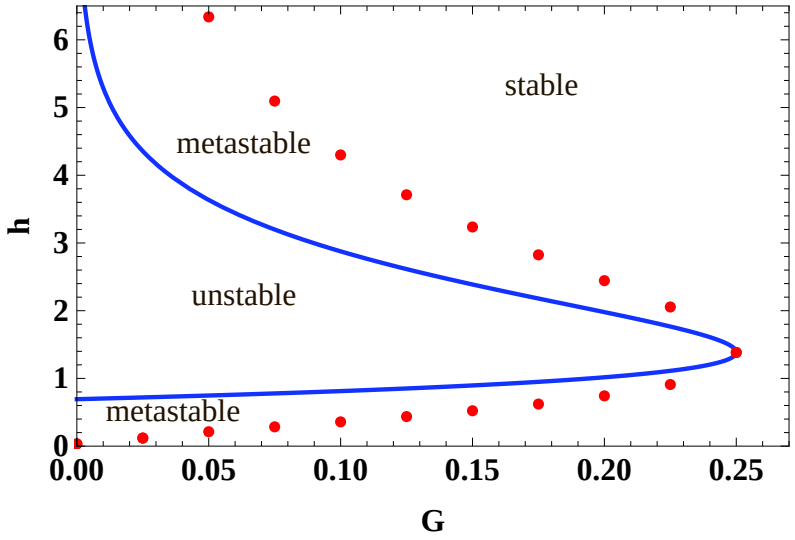

Figure 3.11: The regions for stable, metastable, and linearly unstable flat films in the parameter plane (G,h), where $G(h) = f(h) - C1(h_0)h$.

process occurs. That solution can be found only in the metastable solution range where the nucleation process is favourable. Fig. 3.11 shows the ranges for stable, metastable, and linearly unstable flat films in the parameter plane (G,h). The ranges of different stability behaviour in the parameter plane (G,h) are valid for two and three dimensional film geometries and are given by the position of spinodal line (blue curve in Fig. 3.11) and binodal line (red curve in Fig. 3.11). Binodal line can be calculated by using a Maxwell construction. For example, one can consider an infinitely long film of thickness h_0. Only a small part of finite length has a different thickness h to assure that the mean film thickness is h_0. Compared with the finite length, the width of the finite transition region between the two thicknesses is smaller and its energy can be neglected. One can calculate the energy per unit length of the changed part, which is given by:

$$g(h) = f(h) - C_1(h_0)h. \tag{3.26}$$

where $C_1(h_0) = \partial f(h_0)$. The function $g(h)$ has two minima which represent a lower and an upper linearly stable film thickness. There exist an upper and a lower limit of the metastable thickness range, denoted by h_m^u and h_m^d, respectively. They are characterised by minima of equal depth for $g(h)$ and identical $C_1(h_m)$, i.e. by

$$\begin{aligned} \partial_h f|_{h_m^u} &= \partial_h f|_{h_m^d} \\ g(h_m^u) &= g(h_m^d). \end{aligned} \tag{3.27}$$

Eq. (3.27) are equivalent to a Maxwell construction (see as well [75, 76, 104]). Using the

previous results from linear instability of the flat film and Eq. (3.27) for its absolute stability one can calculate the ranges of different stability shown in Fig. 3.11.

3.3 The Cahn-Hilliard description of the decomposition of a mixture

The film thickness equation discussed in the previous section is related to another important evolution equation that is meant to study the dynamics of binary mixtures that may decompose into their components. The so-called Cahn-Hilliard equation [15, 83] can be seen as a rather general model equation for the irreversible dynamics of out-of-equilibrium systems that approach equilibrium close to a phase transition of first order. Here it is relevant as we are concerned with thin films of mixtures. The film might dewet the substrate and the mixture that forms the film might decompose at the same time.

Originally, the equation has been derived to describe the demixing of a binary solution, or in more general terms one may say that it describes the phase separation of a conserved order parameter. These systems can develop from an initial unstable state through spinodal decomposition process or an initial metastable state through nucleation process. The investigation of spinodal decomposition process has been for many years in attention. While a spinodal decomposition process occurs, a binary mixture that is quenched suddenly into the unstable region will develop fluctuations in concentration that will grow in time. However, phase transition will only happen if the quench brings the solution into the two-phase coexistence region and if the temperature suffices for diffusion.

Phase separation may proceed through the discontinuous process of nucleation and growth in the metastable region, (Fig. 3.12) or by the continuous process of spinodal decomposition in the unstable region, [15]. A calculated representation of spinodal and binodal curve is given in Fig. 3.13. While small concentration fluctuations in the metastable region increase the total free energy of the system in terms of the nucleation energy, a sufficiently large but finite concentration perturbation can decrease it. This makes the entire solid solution unstable and leads to phase separation by discontinuous nucleation and growth.

In contrast, continuous phase separation, as described by spinodal decomposition, slowly and gradually degrades the free energy right from the beginning of phase transition, it is a non-activated process and does not reveal any threshold energy. This type of decomposition

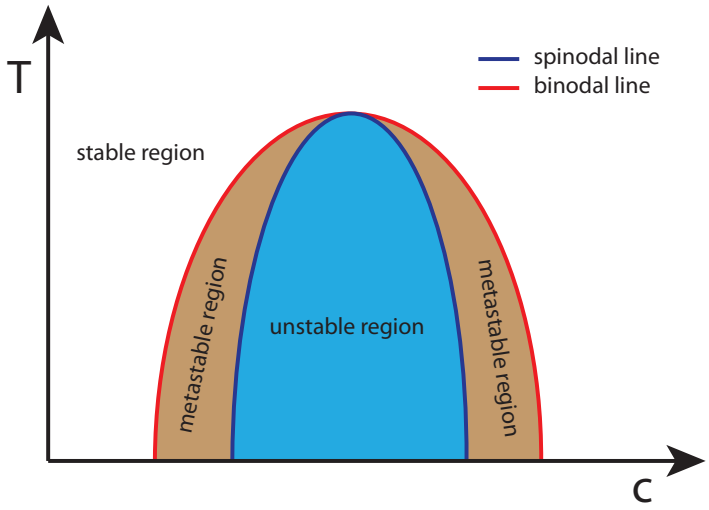

Figure 3.12: A typical phase diagram according to classical thermodynamic theory showing the stable region, the metastable region between red line and blue line where nucleation process occurs and the unstable region, blue area, where spinodal decomposition process is favourable. A calculated representation of spinodal and binodal lines is given in Fig. 3.13.

phenomena are theoretically described by Cahn-Hilliard model [15, 14] which combines the generalised law of diffusion with a Landau energy term. The extension of the original Cahn-Hilliard model to transitions which change the long-range order, the crystal orientation or the crystal structure, is provided by Allen-Cahn model (1979) and its generalised derivatives.

While the Cahn-Hilliard model describes the kinetics of transformation phenomena with conserved field variables, the Allen-Cahn model [44] describes transformations with non-conserved variables (long range order).

The Cahn-Hilliard equation can be viewed as a particular kinetic equation of a time-dependent Ginzburg-Landau theory, which is based on a free energy functional of the so-called "order parameter". For a decomposing mixture the order parameter represents the local concentration of one of the two mixture components.

The Cahn-Hilliard equation is a nonlinear partial differential equation of fourth order in space and first order in time:

$$\frac{\partial \phi}{\partial \hat{t}} = D\nabla^2[\alpha^2\phi^3 - \phi - \nabla^2\phi]. \tag{3.28}$$

where D is a diffusion coefficient and $\alpha = b/\sqrt{a}$ (details in the next section). Here $\partial/\partial\hat{t}$ is the partial time derivative and ∇^2 is the laplacian. The quantity $\mu = \phi^3 - \phi - \gamma\nabla^2\phi$ may be identified as a chemical potential.

An analytical treatment of Eq. (3.28) is very difficult [83]. Therefore, to gain insight into the physical mechanisms which govern the kinetics of demixing one often uses numerical solutions. The most simple techniques used are explicit numerical schemes, as the Euler or Runge-Kutta method. However, for the mentioned simple schemes, to be linearly stable we have to deal with very small time steps Δt. In particular it has to be smaller than a number of order $(\Delta x)^4$, where Δx is the space discretisation length. Therefore, a large number of time steps is required even when exploring the fastest kinetic processes.

In the following two sections, after discussing the derivation of Cahn-Hilliard equation we will analyse the linear and nonlinear stability of trivial homogeneous solutions and give some simulations details and results.

3.3.1 Derivation of Cahn-Hilliard equation

In this section, the derivation of Cahn-Hilliard equation [84, 83], will be developed explicitly. One can consider a $2D$ binary fluid which is composed of two different A and B type particles considering the limit where the diffusion process, as opposed to hydrodynamics, is the only important transport mechanism. Thus, one can define the order parameter field ϕ in such a way that $\phi = 1$ is considered a phase made of first type A particles, and $\phi = -1$ is a phase which is completely made of B type particles. Let assume, as well, that the interactions of AA and BB are favourable and $AB = BA$ are unfavourable. If one particle B and one particle A interact each other, this means that there is a kind of unfavourable energy which is associated with a gradient $\nabla\phi$. Of course, the direction of that gradient does not have a big importance (rotational symmetry) and the energy and its derivatives to be very well defined, then, the gradient in the field has to be energetically penalised by $|\nabla\phi|^2$ in order to confirm that symmetry. Considering the inter-molecular interactions and interactions with any external fields, one can assume that, there is a potential energy landscape, $f(\phi, T)$, that has a transition dependent of temperature from a random and high temperature phase, to an ordered and low temperature phase. Considering the Landau formalism, this can be expressed by a potential with the following form

$$f(\phi, T) = c_1(T)\phi^2 + c_2(T)\phi^4, \tag{3.29}$$

where the two coefficients c_1 and c_2 are connected with the Hamiltonian of the system. When $(\partial^2 f/\partial\phi^2)|_{\phi=0} = 0$, or in the other words when c_1 switches sign, the minimum at $\phi = 0$ vanishes, and lead to a state which has two distinct minima for field values which are non zero

($\phi \neq 0$), what is so called phase transition. Without loss of generality, the potential can be rewritten as

$$f = \frac{1}{4}(a - (b\phi)^2)^2. \tag{3.30}$$

The stable phases, given by $\partial^2 f/\partial\phi^2 = 0$, are

$$\phi^\star = \pm\frac{\sqrt{a}}{b}, \tag{3.31}$$

which can be interpreted as that real values of $\phi^\star$ are stable always ($a > 0$), the energy barrier considered between these fixed points being at $\phi = 0$, Fig. 3.13.

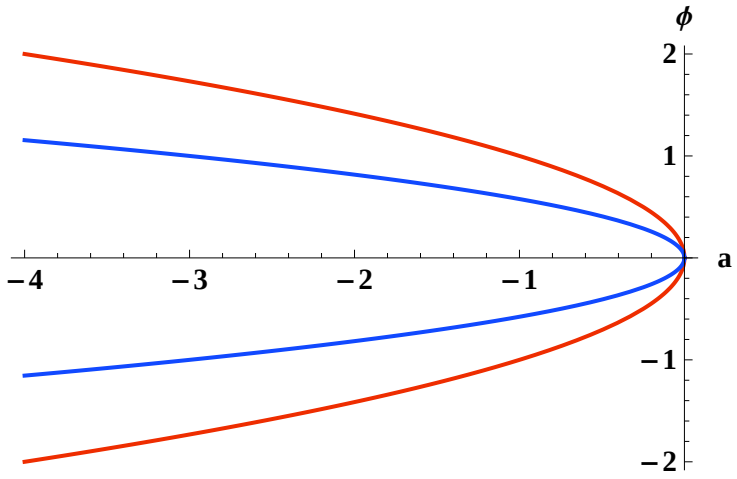

Figure 3.13: Representation of calculated binodal (red) and spinodal (blue) lines for Cahn-Hilliard equation. The value of b parameter in this case is 2.

In order to form a functional of energy for the complete field ϕ in space and time, a combination of this potential with the boundary gradient penalty is necessary:

$$F[\phi(\bar{x}, t)] = \int \left[\frac{1}{4}(a - (b\phi)^2)^2 + \frac{\gamma}{2}|\nabla\phi|^2\right] d\bar{a} \tag{3.32}$$

where γ is a constant that penalises phase boundaries. Its microscopic origins are in the interactions of the particles of type A and type B.

If F is considered the energy of a special configuration of ϕ, where ϕ is seen as a measure for particle concentration, then the variation in functional energy F with respect to ϕ gives how the energy is changing when particles are changing position (considering the chemical potential of the system):

$$\frac{\delta F}{\delta \phi} = \mu \tag{3.33}$$

Starting from this simple idea, to get the final Cahn-Hilliard equation is straight forward, following the next steps.

The Fick's First Law [53], states that the gradient of the chemical potential is proportional to the flux of particles in a system,

$$\bar{J} = -D\nabla\mu, \tag{3.34}$$

where D is the diffusion constant, and is not possible to create, destroy or switch particles, which shows that this flux must follow a continuity equation

$$\frac{\partial \phi}{\partial t} + \nabla \cdot \bar{J} = 0, \tag{3.35}$$

or can be written

$$\frac{\partial \phi}{\partial t} = D\nabla^2\mu. \tag{3.36}$$

However, in general case, M depends on ϕ

$$\bar{J} = -M(\phi)\nabla\mu. \tag{3.37}$$

where, the linear response coefficient $M(\phi)$ has the meaning of a mobility and defines the time scale for the system.

The only remaining step, to finish the derivation, is the calculation of the chemical potential

$$\mu = \frac{\delta F}{\delta \phi} = (b^4\phi^3 - ab^2\phi) - \gamma\nabla^2\phi. \tag{3.38}$$

Finally

$$\frac{\partial \phi}{\partial t} = D\nabla^2[(b^4\phi^3 - ab^2\phi) - \gamma\nabla^2\phi], \tag{3.39}$$

where D is, as mentioned before, an effective diffusion coefficient.

Moving forward can be extracted a length and time scale, in such a way that there will be only one free parameter in the Cahn-Hilliard equation. In order to do that one can suppose that this system has a length scale λ with a time scale τ, that $t = \tau\hat{t}$ and $\bar{x} = \lambda\hat{x}$. Then, one can rewrite the differentials as

$$\frac{\partial}{\partial t} = \frac{1}{\tau}\frac{\partial}{\partial \hat{t}} \tag{3.40}$$

and

$$\nabla^n = \frac{1}{\lambda^n}\nabla^n_{\hat{x}}. \tag{3.41}$$

Then, one can write the Cahn-Hilliard equation

$$\frac{\partial \phi}{\partial \hat{t}} = D\nabla^2 \left[\frac{\tau a b^2}{\lambda^2}(\alpha^2\phi^3 - \phi) - \frac{\tau\gamma}{\lambda^4}\nabla^2\phi \right] \tag{3.42}$$

with $\alpha = b/\sqrt{a}$. This allows to fix τ and λ such that two of the coefficients are set to one

$$\tau = \frac{\gamma}{a^2 b^4} \tag{3.43}$$

and

$$\lambda = \frac{1}{b}\sqrt{\frac{\gamma}{a}}. \tag{3.44}$$

The Cahn-Hilliard equation is now:

$$\frac{\partial \phi}{\partial \hat{t}} = D\nabla^2[\alpha^2\phi^3 - \phi - \nabla^2\phi]. \tag{3.45}$$

One can notice two things: first, near the phase transition the nonlinearity in the PDE is strongest ($\lim_{a\to 0}\alpha = \infty$) and the second, that the length scale diverges at the phase transition ($\lim_{a\to 0}\lambda = \infty$), the well known result.

Considering an initial condition, $\phi(\hat{x}, 0)$, the equation can be solved numerically (Appendix C) for a short description of one of the numerical method), however to get an analytic solution is possible to use the well-known "strong-segregation" limit. "Strong-segregation" limit means that one can consider far from phase transition the region where particles of type A and of type B strongly search their own kind, such that $\alpha \ll 1$. Thus, the Cahn-Hilliard equation can be written in a linearized form

$$\frac{\partial \phi}{\partial \hat{t}} = -\nabla^2[\phi + \nabla^2\phi] \tag{3.46}$$

Eq. (3.46) is called the linear Cahn-Hilliard equation [14, 84, 83]. This equation was first used by Cahn to describe a spinodal decomposition in binary alloys upon a fast quench from a temperature, where the alloy is stable down, to a temperature where the alloy is unstable.

3.3.2 Linear stability of the Cahn-Hilliard equation: spinodal and binodal lines

In the previous section the derivation of the Cahn-Hilliard equation is provided, which is essentially a diffusion equation and describes the time evolution of a conserved order parameter. This section will give a short overview and description of the linear stability of the Cahn-Hilliard equation and give some conclusions for stationary periodic solutions and their stability obtained by continuation techniques.

Considering a Cahn-Hilliard equation in one spatial dimension, the spatially uniform solution $\phi(x) = \bar{\phi} = \phi_0 = const$ is a fixed point of the Cahn-Hilliard equation, Eq. (3.46). The linear stability of the uniform solution ϕ_0 of the Cahn-Hilliard equation, can be analysed by using a Fourier mode decomposition of the perturbation:

$$\phi(t, x) = \phi_0 + \phi_1 \exp(\beta t + ikx), \tag{3.47}$$

where $\phi_1 \ll 1$ is the amplitude of the perturbation and β and k are its growth rate and wave number, respectively. Plugging the perturbation ansatz of Eq. (3.47) into the full time dependent rescaled Cahn-Hilliard equation, and linearizing in ϕ_1 one obtain a relationship between the wave number of the perturbation and its growth rate, This relationship is called dispersion relation and it is given by

$$\beta(k) = -\phi_0(1 - \phi_0)[k^2 \partial_\phi^2 f(\phi_0) + k^4]. \tag{3.48}$$

where $f(\phi)$ represents the local free energy density. The uniform solution ϕ_0 is linearly unstable for positive growth rates, e.g. for finite $k > 0.$, the fix point ϕ_0 is unstable for

$$\partial_\phi^2 f(\phi_0) < 0. \tag{3.49}$$

The critical wave number k_c is determined by the condition $\beta(\phi_0) = 0$ and is given by

$$k_c = \sqrt{-\partial_\phi^2 f}. \tag{3.50}$$

The wave number k_m with the maximum growth rate of the dispersion relation is given by

$$k_m = \sqrt{-\frac{\partial_\phi^2 f(\phi_0)}{2}} \tag{3.51}$$

Note, that at zero wave number one can find a zero growth rate. This stationary instability is called type II_s instability, according to the classification by Cross and Hohenberg [21]. This type of instability is often associated with conservation relations in the system. The condition $\partial_\phi^2 f(\phi_0) = 0$ is called the spinodal line (Fig. 3.12), similarly the region for which the condition $\partial_\phi^2 f(\phi_0) < 0$ holds is called the spinodal region. If a binary solution has the parameters in the spinodal region then it will start to decompose into two distinct liquid phases upon infinitely small perturbations. This process is called spinodal decomposition.

Fig. 3.12 shows the spinodal and binodal lines of a binary solution, schematically. The region between the spinodal and binodal lines is called metastable because in this region two

linearly stable states of the system coexist, but the uniform state is linearly stable. Nevertheless, two distinct phases can coexist, but phase separation only occurs via nucleation. Fluctuations can be large enough to produce a nucleus above a certain critical size. The critical nucleus size depends on the distance to the spinodal line. A larger distance from the spinodal line requires a larger critical nucleus. In the spinodal region, the uniform state of the system is unstable with respect to infinitesimal small perturbation. The spinodal and binodal line meet at the critical point.

By quenching the system from the stable into the unstable region through the critical point, the system undergoes a second order phase transition, otherwise the system undergoes a first order phase transition.

So far, we have seen some results and discussions for the the initial period and the expected equilibrium state for phase separating mixture. Using continuation techniques [30] one can also study the stationary solutions of the Cahn-Hilliard equation in one spatial dimension for a finite system with size L. Setting the time derivative of the concentration ϕ in Cahn-Hilliard equation to zero and integrating the time independent equation twice, is obtained a nonlinear ODE of second order which can be solved using the appropriate boundary and integral conditions. Depending on the chosen parameters one can find for the Cahn-Hilliard equation three qualitatively different one parameter solution families in the linearly unstable and metastable range. A qualitatively similar behaviour was found for the stationary periodic solutions of the thin film equation, Eq. (3.13), on a horizontal solid substrate [129]. The discussion of this problem is beyond the scope of this introductory chapter. A more thorough discussion of this problem for the case of dewetting of thin liquid films on a horizontal solid substrate can be found in [129].

An interesting subject of Cahn-Hilliard equation is the late stage. Experiments and numerical studies showed that phase separating mixtures initially develop a periodic structure with a certain spinodal wavelength or nucleation. But these structures are not stable in large systems, where several wavelength fit into system. The system will move instead to a lower free energy and therefore larger period. This process is called coarsening. The driving force for coarsening is mainly the reduction in energy associated with interfaces. In practice, the coarsening process is a major concern for micro-structured materials. The discussion of this problem is beyond the scope of this introductory chapter, as well.

The Cahn-Hilliard equation is a continuous evolution equation to describe the formation of periodic structure from a uniform state. Using linear stability analysis one obtains a phase

diagram with three different regions, called stable, binodal and spinodal region. In the stable region no phase separation can occur. In the spinodal regime phase separation can occur via a spinodal decomposition process whereas in the binodal regime phase separation can only occur via nucleation and growth process.

In Appendix C, in order to illustrate the spinodal decomposition and nucleation process, the Cahn-Hilliard equation is solved numerically using a semi-implicit time discretisation scheme. A series of snapshots in time can be seen in the Fig. 3.14 and Fig. 3.15 for spinodal decomposition and nucleation process, respectively.

For the studied experimental system (experiments that use monodisperse colloidal suspensions of thiol-passivated gold nanoparticles in toluene [41, 77, 69, 70, 90, 91, 116]) a description using thin film equation is not suitable because the nanoparticles are not taken into account. However, under certain conditions one can argue that thin film equation can be coupled with an equation for the evolution of the mean particle concentration. The resulting model is able to describe the behaviour of an evaporating solution on the meso- and macroscale [19, 20, 130, 38]. However, the theory is less suited to a description of the dewetting dynamics of the ultrathin postcursor film.

The dewetting of the ultrathin film of highly concentrated suspension may be described by a discrete stochastic model such as, for instance, a kinetic Monte Carlo (KMC) model based solely on evaporation/condensation dynamics of the solvent and diffusion of the solute [95, 116, 133]. Such a model is introduced in the next chapter of the thesis.

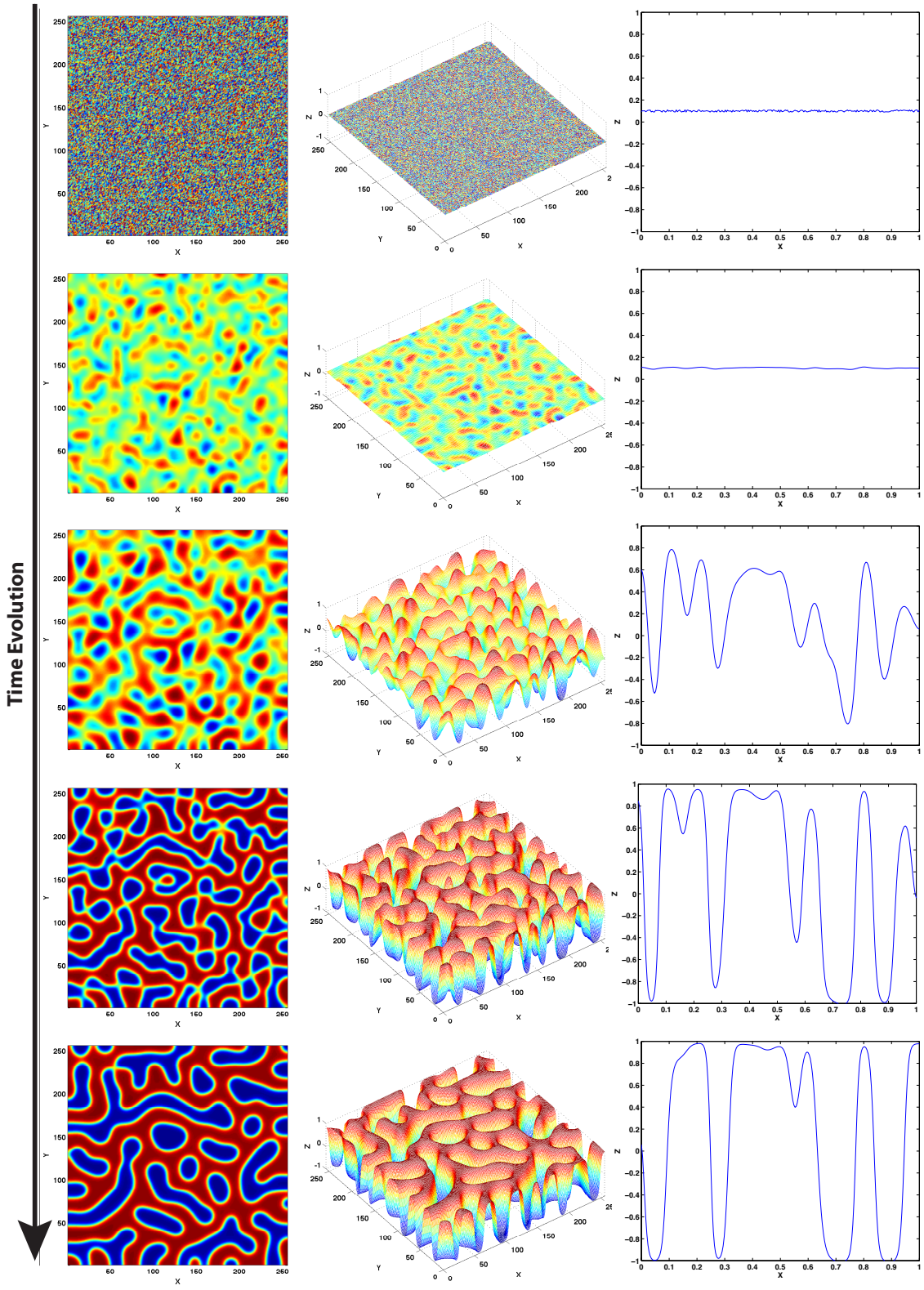

Figure 3.14: Snapshots showing the evolution in time for Cahn-Hilliard equation towards to spinodal decomposition process starting with random initial distribution for concentration of mixture. First column shows 2D plots, the second column shows 3D surface plots for the same time steps as first column and in the third column is shown a cross section of the corresponding patterns.

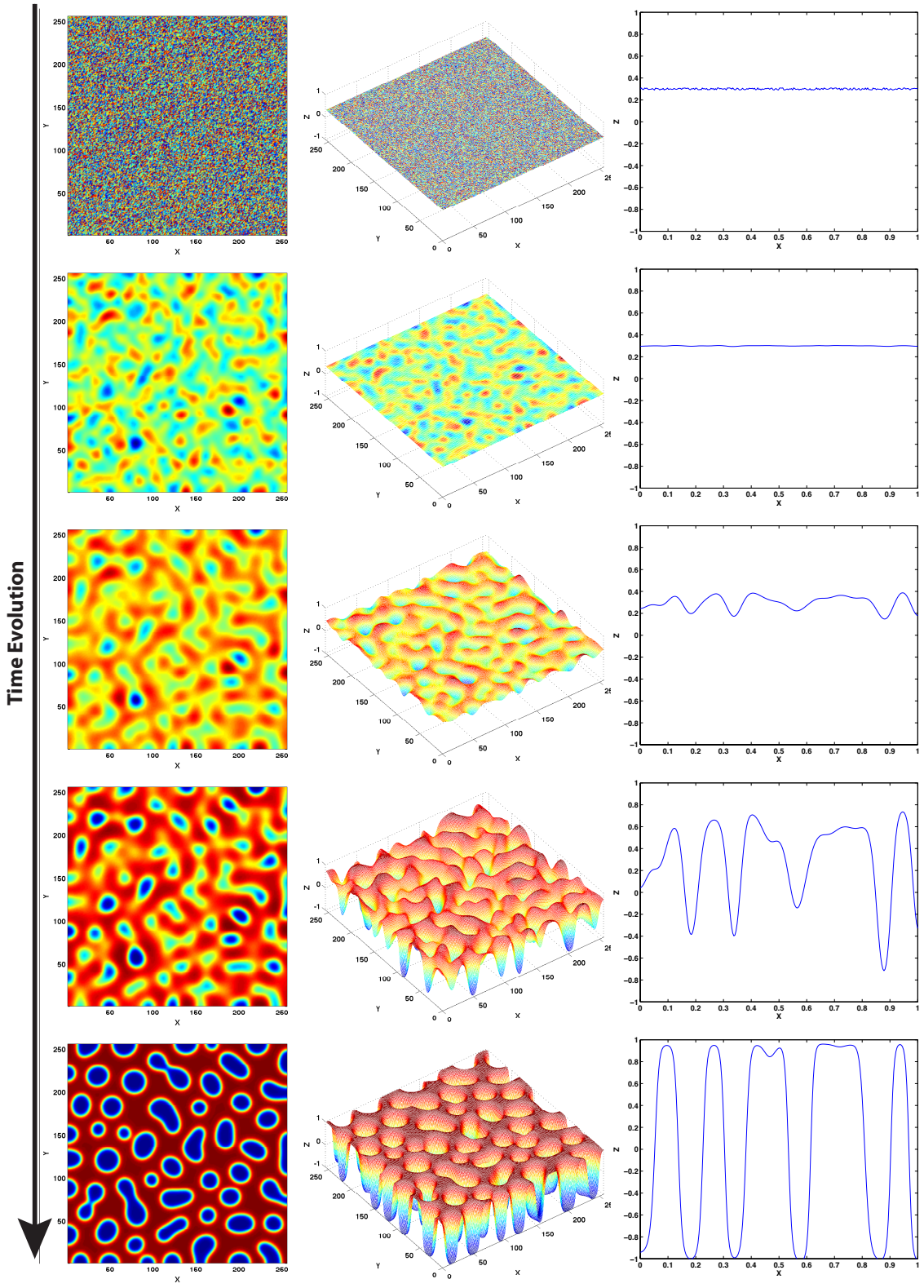

Figure 3.15: Snapshots showing the evolution in time for Cahn-Hilliard equation towards to nucleation process starting with random initial distribution for concentration of mixture. First column shows 2D plots, the second column shows 3D surface plots for the same time steps as first column and in the third column is shown a cross section of the corresponding patterns.

Chapter 4

Modelling and Simulations

4.1 Kinetic Monte Carlo model

4.1.1 Two dimensional model

Kinetic Monte Carlo models are a common tool to investigate a wide variety of dynamical processes [18, 37]. In particular, they have proved to be attractive tools to model adsorption, diffusion, and aggregation in surface science resulting in interfacial growth and structuring like, e.g., the growth of metal layers as atoms arrange after being deposited on surfaces [55, 61, 96]. A schematic representation of Kinetic Monte Carlo using Metropolis algorithm is given in Fig. 4.1 and a detailed introduction is presented in Appendix D.

The approach followed in Ref. [95] to model an evaporating dewetting nanoparticle solution is based on an Ising-type model for the liquid-gas phase transition. To facilitate comparison with previous work we first choose the model to be exactly the same as in Ref. [69] (building on Ref. [95]): The system is described using a two-dimensional lattice gas of two fields n and l. We allow for three types of possible states of a cell – liquid ($l = 1, n = 0$), nanoparticle ($l = 0, n = 1$), and vapour ($l = 0, n = 0$, i.e., cell empty). Thereby liquid/vapour is assigned per 1×1 cell whereas it is assumed that the nanoparticles fill 3×3 cells (see sketch Fig. 4.2) to indicate the larger size of the nanoparticles used in the experiment as compared to the correlation length of the liquid. This detail, however, turns out to be not very relevant as further discussed in the Conclusion.

The energy of a configuration of the two-dimensional assembly of vapour, liquid and nanopar-

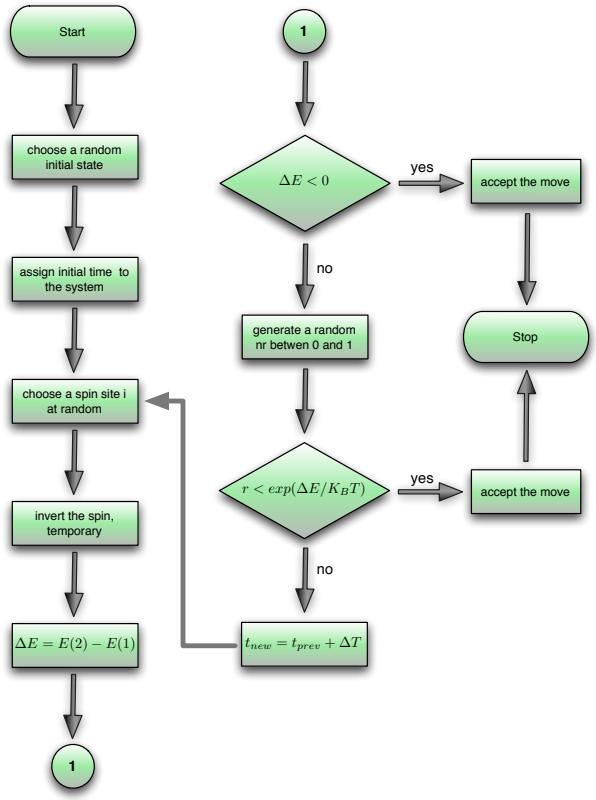

Figure 4.1: Flowchart diagram of Kinetic Monte Carlo using Metropolis algorithm.

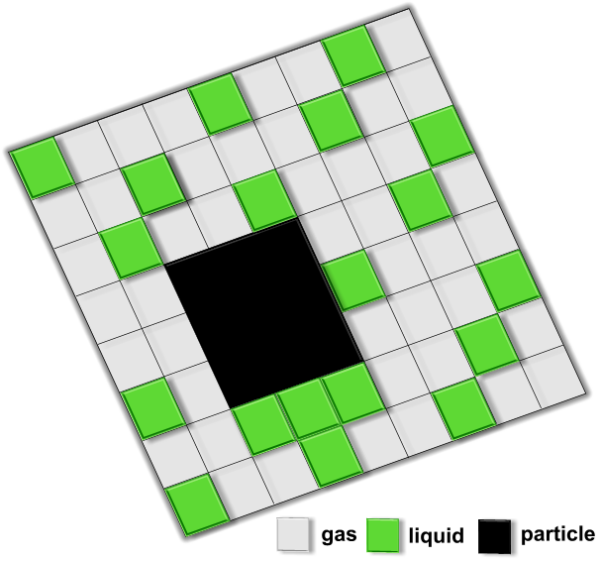

Figure 4.2: Schematic picture of the two-dimensional lattice gas model used: the size of nanoparticle is in our case 3×3, whereas a liquid cell is of size 1×1. The side length of such a cell represents the correlation length of the solvent approximated to be 1 nm [95].

ticles is determined by the Hamiltonian

$$E = -\frac{\varepsilon_{nn}}{2}\sum_{<ij>} n_i n_j - \frac{\varepsilon_{nl}}{2}\sum_{<ij>} n_i l_j - \frac{\varepsilon_{ll}}{2}\sum_{<ij>} l_i l_j - \mu\sum_i l_i \tag{4.1}$$

where ε_{ll}, ε_{nn} and ε_{nl} are the interaction energies for adjacent sites (i, j) filled by (liquid,liquid), (nanoparticle,nanoparticle) and (liquid,nanoparticle), respectively. For fixed interaction strength, the equilibrium state is determined by the chemical potential μ that controls the evaporation and/or condensation of the liquid. We will call $|\mu|$ the driving force as it is primarily responsible for the motion of a dewetting or wetting front. The sums $\sum_{<ij>}$ are taken over all pairs of nearest and next-nearest neighbours. Thereby, the interaction strength of the next nearest neighbours is corrected by a factor $1/\sqrt{2}$ due to their larger distance [69]. In the following we fix $\varepsilon_{ll} = 1$, i.e., we express all energies and the chemical potential in the scale of the liquid-liquid interaction energy.

The energy functional determines the equilibrium state and the energy landscape of the system. The dynamics is determined by the allowed Monte Carlo moves, their relative frequency, and the rules for their acceptance. Two types of moves are allowed: (i) evaporation/condensation of liquid and (ii) diffusion of nanoparticles within the liquid. To simulate the dynamics, the energy loss or gain ΔE related to a potential move is calculated. The move is then accepted with the probability $p_{\text{acc}} = \min[1, \exp(-\Delta E/kT)]$ where k is the Boltzmann constant and T the temperature. The rule implies that any move that decreases the energy of the system is accepted when tried. Any move that increases the energy has a probability corresponding to the related Boltzmann factor. Consistent with the above scales, temperature is expressed in units of ε_{ll}/k. It determines the importance of fluctuations in the system. For $T = 0$ the system is fluctuation-free, i.e. the evolution follows a deterministic gradient dynamics.

Practically, we use a checkerboard Metropolis algorithm to advance the liquid/vapour subsystem; each solvent or vapour cell is examined in turn, and is converted from liquid to vapour or from vapour to liquid with the acceptance probability p_{acc}. After one solvent cycle all particles are considered and a diffusive move is tried. The nanoparticles are free to perform a restricted random walk on the lattice. It is restricted because particles are only allowed to move into wet areas of the substrate, i.e., onto cells with $l = 1$. This is a very important rule and models zero diffusivity of the particles on a dry substrate. If such a "forbidden" move is tried, the particle is left at rest and the next particle is considered. The diffusivity or mobility of the nanoparticles inside the liquid is controlled by the number of times each particle is examined after one solvent cycle. This computational ratio M of particle and solvent cycles reflects the

physical ratio of time scales for evaporation and diffusion. Large M, for instance, indicates that diffusion is fast as compared to evaporation, i.e., it stands for a large diffusion constant of the nanoparticles or/and a low evaporation rate for the liquid. It therefore represents a low effective viscosity of the solution.

The model is used in the following to first review some general results for a homogeneous system without and with nanoparticles (Section 4.2). Then we focus on a parametric analysis of the fingering instability (Section 4.3). A few typical Kinetic Monte Carlo simulations results for the final dried-in nanoparticle structures are shown in Fig. 4.3.

4.1.2 Pseudo-3D model

Even if the 2D model can reproduce numerous nanoparticle arrangements quantitatively and qualitatively it is not able to reproduce the patterns where several structures and/or several length scales coexist like the ones shown in Fig. 4.4. Martin et al, [70], develop a pseudo 3D model by including a dependency of the chemical potential μ on mean solvent density (liquid coverage) in the original 2D Kinetic Monte Carlo model, Eq. (4.1), where μ, the effective chemical potential, defines only the equilibrium state of the solvent.

The hamiltonian of the system is given by:

$$E = -\frac{\varepsilon_{nn}}{2}\sum_{<ij>} n_i n_j - \frac{\varepsilon_{nl}}{2}\sum_{<ij>} n_i l_j - \frac{\varepsilon_{ll}}{2}\sum_{<ij>} l_i l_j - \mu(\nu)\sum_i l_i \tag{4.2}$$

where ε_{ll}, ε_{nn} and ε_{nl} are the interaction energies for adjacent sites (i, j) filled by (liquid,liquid), (nanoparticle,nanoparticle) and (liquid,nanoparticle), respectively, and ν is the fraction of liquid that has converted to vapour. This introduces a global coupling as ν is a global measure that then determines the local dewetting behaviour.

By running the simulations and exploring the parameter space of this *pseudo-3D* model, one can obtain nucleation process in which holes are surrounded by smaller nucleated holes, as illustrated in Fig. 4.4.

In order to obtain the patterns shown in Fig. 4.4 for the chemical potential μ is used the following expression:

$$\mu(\nu) = \mu_0 + (0.1\mu_0 \cdot \nu^{0.7}) \tag{4.3}$$

where μ_0 is the initial chemical potential and ν represents the position of the centre.

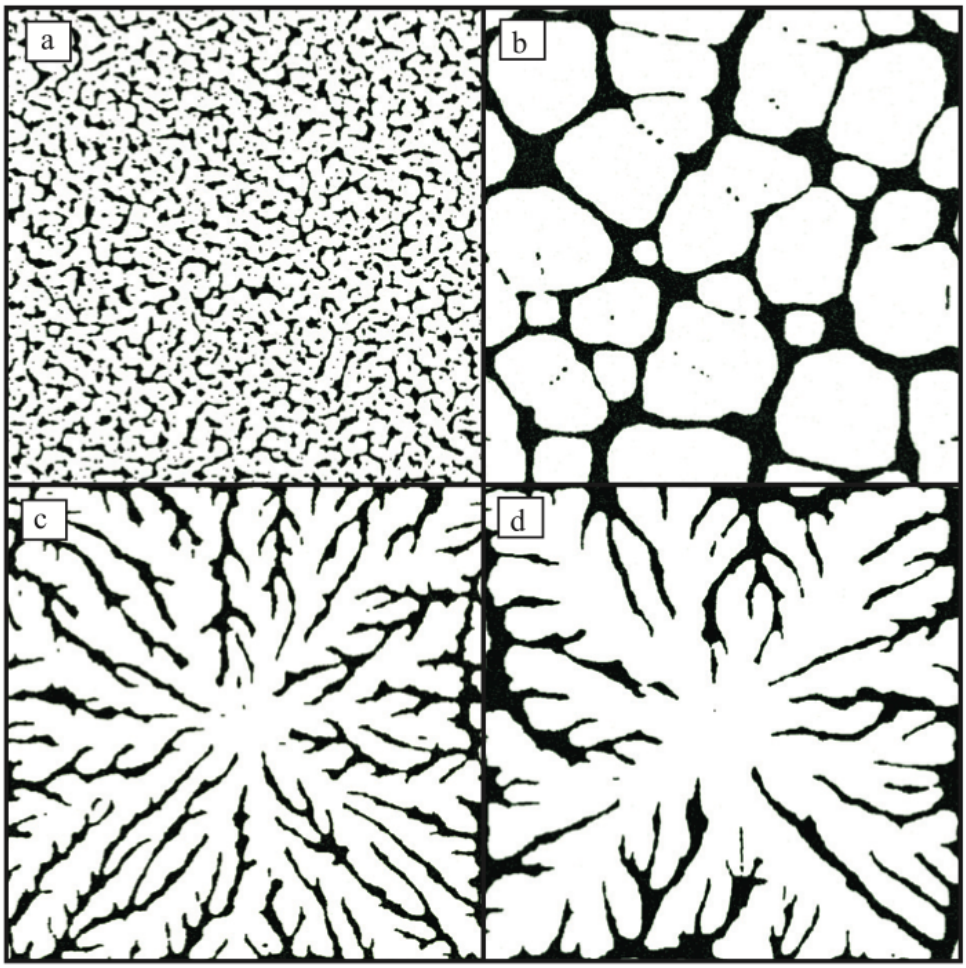

Figure 4.3: Typical KMC results for the final dried-in nanoparticle structures resulting from the evaporative dewetting processes of nanoparticle solutions (nano-fluids) in the case of (a) a spinodal-like process at $\mu = -2.55$, (b) nucleation and growth of holes at $\mu = -2.3$, (c) unstable fronts at $\mu = -2.3$ and low mobility $M = 5$, and (d) unstable fronts at $\mu = -2.3$ and medium mobility $M = 10$. The starting configuration in (a) and (b) is a homogeneous liquid film with uniformly distributed particles whereas in (c) and (d) a hole at the centre is nucleated by hand. The remaining parameters are ((a), (b)) $M = 50$, $\varepsilon_{nl} = 2.0$, $\varepsilon_{nn} = 1.5$, $\phi = 0.2$, $kT = 0.3$, MC steps = 500, lattice size 1200x1200; ((c), (d)) $\varepsilon_{nn} = 2.0$, $\varepsilon_{nl} = 1.5$, $\phi = 0.2$, $kT = 0.2$, MC steps = 3000, lattice size 1200x1200. Lattice sites occupied by particles are coloured black, and the empty sites are coloured white.

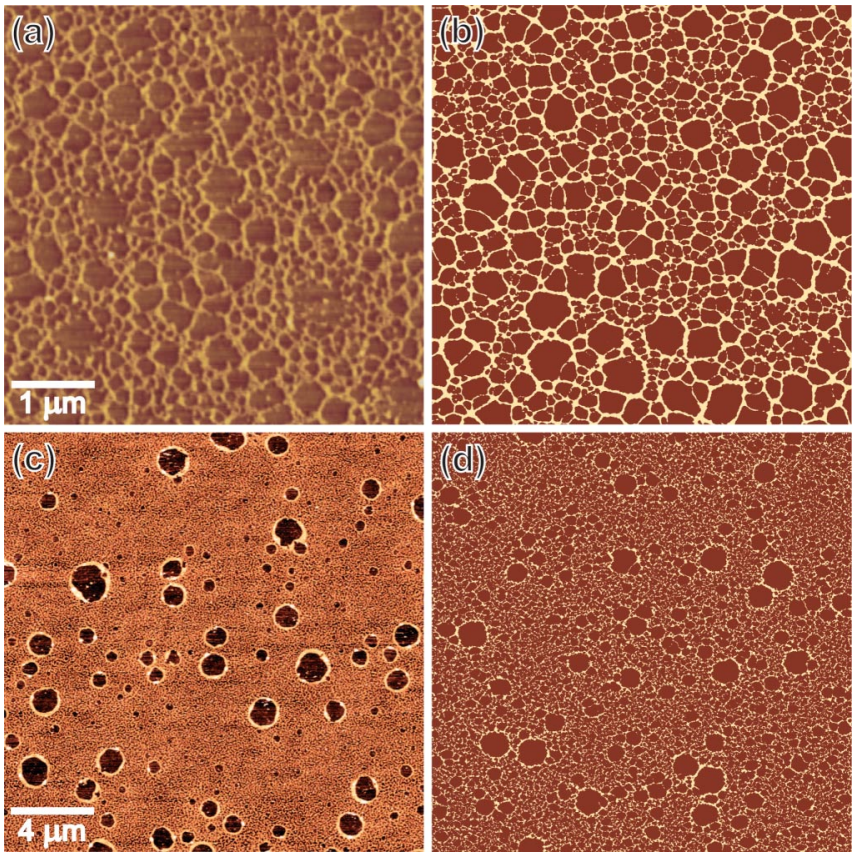

Figure 4.4: (a) An AFM image of a two-level cellular structure formed by spin-casting gold nanoparticles in toluene onto a silicon substrate, (b) a simulated structure formed by linking the chemical potential (μ) to the solvent density [in the form $\mu(\nu) = \mu_0 + (0.1\mu_0 \cdot \nu^{0.7})$, where ν is the fraction of solvent that has become vapour, and μ_0 is the value of μ at the beginning of the simulation], (c) an AFM image of gold nanoparticles spun onto silicon from chloroform, and (d) a simulated image with a much stronger coupling between μ and solvent coverage [in the form $\mu(\nu) = \mu_0 + (0.5\mu_0 \cdot \nu^{0.7})$], (Courtesy of C. P. Martin).

Finally, one can mention that the *pseudo-3D* model introduced by Martin et al. [70] can be used to produce patterns shown in Fig. 4.4 which are not possible to be obtained with the 2D model or even with Yosef-Rabani's 3D model, but experimentally can be seen. The discussed model is a simpler alternative to a fully 3D model, considered by Sztrum et al. [120, 139].

4.1.3 Three dimensional model

Extending Rabani's original 2D model, Yosef and Rabani develop a fully 3D model [139, 120], that allows them to reproduce by simulations ring-shaped nanoparticle assemblies observed experimentally. The 3D model introduces a third spatial dimension by considering the last few layers of solvent above the substrate during evaporation.

A nucleation site is inserted in a given location on the surface before the evaporation process, where that hole will grow following dewetting. An important aspect is that the global evaporation rate of the solvent, the hole nucleation and as well the hole growth rate can be modified separately.

The improved 3D model reproduces the formation of fingering holes in sub-monolayers of colloidal nanoparticles, in a parameter range that agrees with the experimental conditions.

One major issue with the 3D model of Yosef and Rabani is that one needs to introduce an initial hole to see a growing hole. Nucleation does not take place naturally as it does experimentally.

4.1.4 Justification of usage for 2D model

The simple two-dimensional kinetic Monte Carlo model described above is based on two key assumptions: (1) that the relevant processes can be captured by a two-dimensional setting neglecting changes in the film thickness of the evaporating film; and (2) that all relevant dynamics are a result of the diffusion of nanoparticles and of the evaporation of the solvent. Convective motion of the solution is entirely neglected. A refined model increases the spatial range of considered energetic interactions including next-nearest neighbours [69] but otherwise uses the same basic assumptions. Considering the strong assumptions, the agreement with experiments is amazingly good [95, 69]. As we shall now discuss, recent experiments using the meniscus technique (described above) may explain why.

In Ref. [91] the evolution of the branched patterns is followed in real-time using contrast-enhanced video microscopy. The video (complementary material of Ref. [91]) clearly shows

that different processes occur on different scales. First, a macroscopic dewetting front recedes, leaving behind a seemingly dry substrate. The macroscopic front can be transversally unstable resulting in large-scale ($> 100\mu$m) strongly anisotropic finger structures. For fronts that move relatively quickly these macroscopic structures cover all available substrate. However, when at a later stage the macroscopic front becomes slower, those fingers become scarce and "macroscopic fingering" finally ceases. At this stage it is possible to appreciate that the seemingly dry region left behind by the front is not at all dry, but covered by an ultrathin "postcursor" film that is itself not stable. At a certain distance from the macroscopic front the ultrathin film starts to evolve a locally isotropic pattern of holes. The holes themselves grow isotropically in an unstable manner resulting in an array of isotropically branched structures. This indicates that *nearly all* of the patterns described in various publications result from processes in the ultrathin film whose thickness is of the order of the size of the nanoparticles.

Focusing on the structuring of the ultrathin film, we next identify the important dynamical processes. On the mesoscopic scale the dynamics of a thin film of pure liquid can be described by a thin film equation derived using a long wave approximation [88, 54]. In such a model, the temporal change in film thickness h results from the gradient of the convective flow $h^3(\nabla p)/3\eta$ and from an evaporative loss $\beta(\rho\mu_0 - p)/\rho$ [65, 92]. Here, η and ρ are the dynamic viscosity and density of the solvent, respectively, μ_0 is the chemical potential (related to the ambient vapour pressure of the solvent), and β is a rate constant that can be obtained from gas kinetic theory or from experiment [65]. The pressure p contains curvature and disjoining pressures and drives *both* processes – convection and evaporation. The disjoining pressure describes the wettability of the substrate [22, 52, 75, 123]. Due to the thickness dependence h^3, the mobility related to convective motion is large for thick films but decreases strongly with decreasing film thickness whereas the mobility related to evaporation (the rate constant) is a constant. In consequence, it is expected that for a nano-metric film the evaporation term strongly dominates. Using the parameters given in Ref. [65] and assuming a small contact angle of about 0.01, one obtains a cross-over thickness in the lower single digit nanometer range. Below this thickness the solvent dynamics is dominated by evaporation.

This consideration, together with the experimental observation discussed above, justifies the neglect of convective motion in the kinetic Monte Carlo model. Without convection a two-dimensional model is sufficient to cover the essential processes. Note that a refinement proposed in [70] introduces a three-dimensional aspect into the two-dimensional model by making the

chemical potential dependent on mean liquid coverage (i.e., on a parameter related to mean thickness). This amounts to a consideration of the thickness-dependent disjoining pressure in the evaporation term *without* the explicit incorporation of a film thickness.

4.2 Behavior of a homogeneous system

4.2.1 Without nanoparticles

Without nanoparticles the behavior of the model introduced in Section 4.1 is well known, it reduces to the classical Ising model, Eq. (6.47), in two dimensions describing the order-disorder transition in a ferromagnetic system. Using the mapping $\mu \to \mu_0 H - 2$ and $l \to (s+1)/2$ where $s = \pm 1/2$ corresponds to the spin of a cell, μ_0 to the magnetic moment and H to the external magnetic field, all results since Onsager [87] can be used. In particular, an infinitely extended system has a critical point at $\mu_c = -2$ and $kT_c^\infty = 1/[2\ln(1+\sqrt{2})] \approx 0.567$. For temperatures below T_c^∞ at $\mu_{\rm ph} = -2$ the liquid state and the vapour state may coexist, whereas for $\mu < -2$ [$\mu > -2$] eventually the vapour [liquid] state dominates. A chemical potential not equal to -2 corresponds to a non-zero external magnetic field in the ferromagnetic system.

For $T < T_c^\infty$ there exists a first order phase transition at $\mu_{\rm ph}$; systems in the liquid [gas] state are metastable for a certain range below [above] $\mu_{\rm ph}$. Mean field theory as presented, e.g., in Ref. [60] provides the line that is the lower [upper] limit for the existence of metastable liquid [gas] states in the (μ, kT) plane. The two curves fulfil

$$\mu_{\rm ms}^{\pm} = \pm \frac{2}{3} kT \left(\frac{T_c^\infty}{T} - 1 \right)^{3/2} - 2, \tag{4.4}$$

where we set the grid spacing used in Ref. [60] to one.

An overview of the equilibrium phases and the resulting behavior of a straight wetting or dewetting front (as described next) is given in Fig. 4.5. Starting with a liquid covered substrate in a region ($\mu < -2$) where the global energy minimum corresponds to the vapour phase leads to an evaporative dewetting process that either follows a nucleation and growth pathway or results from a spinodal-like process. Typical snapshots illustrating the two processes are shown in Fig. 4.6. Nucleation and growth of holes occurs in the parameter region close to $\mu_{\rm ph} = -2$ where the homogeneous liquid state is still metastable. At smaller $\mu < \mu_{\rm ms}^-$, i.e., at larger driving forces $|\mu|$ a spinodal-like process occurs when starting with a liquid-filled plane. Many very small holes appear at once, and all liquid evaporates very quickly, leaving the substrate

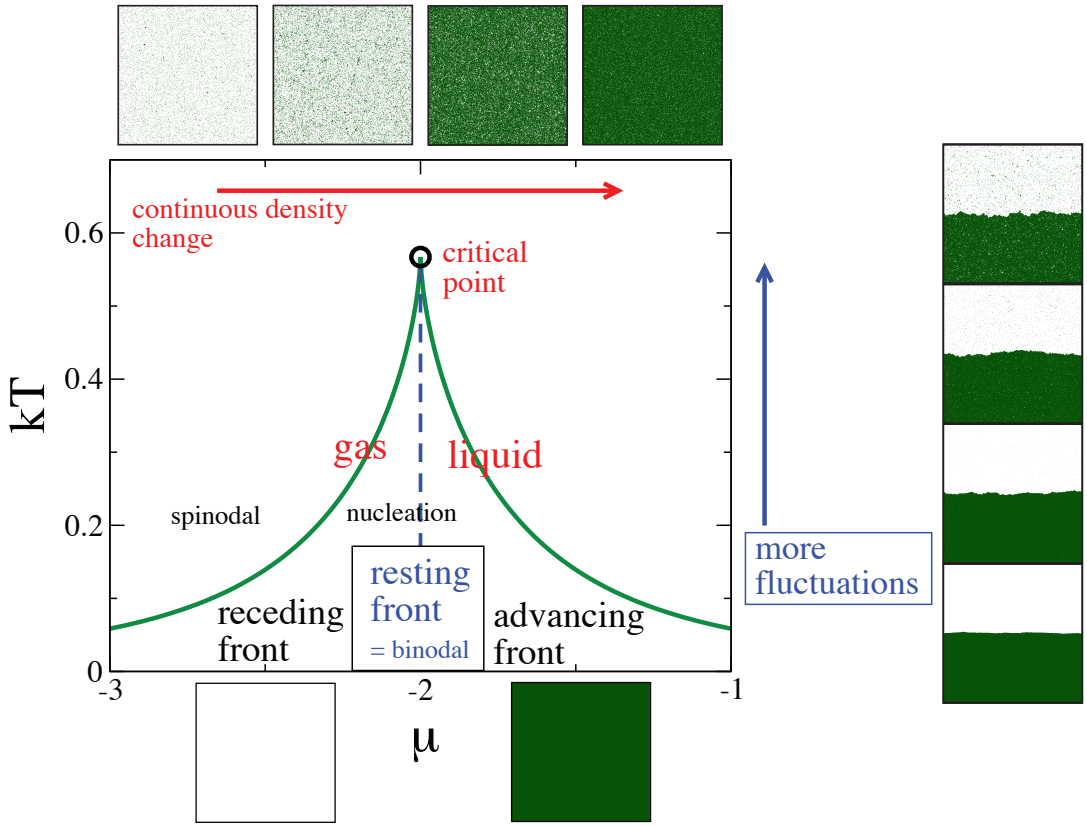

Figure 4.5: Phase diagram without nanoparticles (central panel). A schematic overview of system behavior is given in the plane spanned by the dimensionless chemical potential μ and the dimensionless measure of temperature kT. The liquid and gas phase are indistinguishable above the critical temperature $kT_c = 1/[2\ln(1+\sqrt{2})] \approx 0.57$. The corresponding gradual change of mean density with μ is indicated by the four snapshots of equilibrium states shown in the upper line (from left to right: $\mu = -2.75, -2.25, -1.75$ and -1.25; $kT = 0.8$). Below T_c the system can show a rich dynamics when evolving towards equilibrium. For $\mu > -2$ [$\mu < -2$] the equilibrium corresponds to liquid [gas] as illustrated by the snapshots in the bottom row ($\mu = -1.5$ [$\mu = -2.5$] and $kT = 0.05$), whereas at $\mu_{\rm ph} = -2$ gas and liquid may coexist. At $\mu_{\rm ph}$ a straight front separating gas and liquid does not move on average. However, depending on temperature it fluctuates, as illustrated by the snapshots in the right column (from bottom to top $kT = 0.1, 0.3, 0.45$ and 0.55; $\mu = \mu_{\rm ph} = -2$). A straight liquid front will recede [advance] for $\mu < -2$ [$\mu > -2$], i.e. one is able to study evaporative dewetting [wetting] fronts. Starting, however, with an homogeneous liquid-covered [gas-covered] substrate for $\mu < -2$ [$\mu > -2$] the substrate will empty [fill] via a nucleation or spinodal-like process. The borders between the different processes are indicated as heavy lines (e.g. green line represents μ_{ms}) and are discussed in the main text. All snapshots are obtained from simulations for a small domain size of 300×300 after 1000 kinetic Monte Carlo steps.

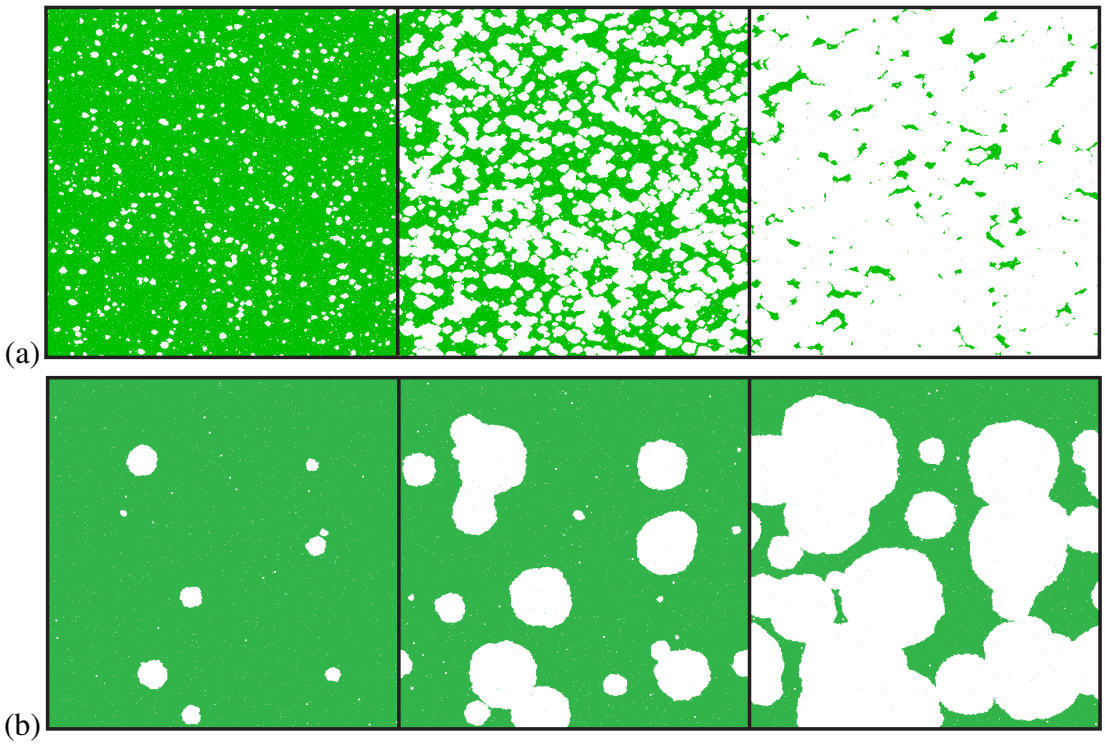

Figure 4.6: Snapshots from typical evaporative dewetting processes without nanoparticles in the case of (a) a spinodal-like process at $\mu = -2.55$ and (b) of nucleation and growth of holes at $\mu = -2.3$. The starting condition in each case is an homogeneous liquid film. The number of Monte Carlo steps is from left to right (a): 5, 10, and 15; (b): 40, 80, and 120; $kT = 0.3$ and the lattice size is 600×600. Liquid is green and the empty substrate is white.

empty. When starting with an homogeneous gas state at $\mu > -2$, similar mechanisms result in a liquid-filled plane.

A straight front separating vapour- and liquid-covered substrate areas remains on average at rest for $\mu = -2$ although it might fluctuate quite strongly. The liquid state will advance and recede for $\mu > -2$ and $\mu < -2$, respectively. For a resting or moving front the temperature ($T < T_c$) determines the strength of the fluctuations that modulate the straight front (see snapshots at the right of Fig. 4.5). The overall picture is similar for circular fronts, however, the exact value of μ that results in a resting front depends on the average curvature of the front (i.e. the size of the hole). A two-dimensional "curvature pressure" enters the balance. Fixing some $\mu_{\rm ms}^{-} < \mu < -2$, a hole in a liquid layer will grow [shrink] above [below] a certain radius $r_c(\mu)$. The growing hole will remain almost circular. Practically, on a square grid in late stages it will become square-like (original model in Ref. [95] where only nearest neighbours are considered). Including next nearest neighbours leaves the holes circular up to a later stage, when

they become octagonal.

4.2.2 With nanoparticles

Having discussed the behavior of the model without particles we now turn our attention towards situations where nanoparticles are present. First, we discuss the equilibrium behavior, followed by an analysis of the evolution of an initially liquid-filled well-mixed homogeneous system.

We expect the particles to influence the location of the liquid-gas phase transition. Inspecting the Hamiltonian, Eq. (4.1), one can estimate the influence using a mean field argument. Let us consider a liquid-filled cell at a straight liquid front. We consider the energy needed to move the front, i.e., to empty the cell. On average a cell at a straight front has two direct neighbours occupied either by liquid or nanoparticles. We replace the nanoparticle occupation number in the liquid-particle interaction term by its mean value, i.e., the coverage ϕ, neglect the particle-particle interaction term as we consider a cell either filled by liquid or gas, and replace one of the liquid occupation numbers in the liquid-liquid interaction term by its mean value for a filled cell $1-\phi$. In this way we can map the model onto the pure liquid-gas case by replacing μ by $\tilde{\mu} = \mu + 2(\varepsilon_{nl} - 1)\phi$. Following this argument we expect the phase transition to occur at $\tilde{\mu} = -2$, i.e., an attractive liquid-nanoparticle interaction ($\varepsilon_{nl} > 0$) stronger than the liquid-liquid interaction ($\varepsilon_{ll} = 1$) implies that the phase transition occurs at $\tilde{\mu}_{\mathrm{ph}} = -2 - (\varepsilon_{nl} - 1)\phi < \mu_{\mathrm{ph}}$. Note, however, that for low particle concentrations (e.g., $\phi = 0.1$) the change is rather small for $\varepsilon_{nl} = 1.5$, i.e. the value used in most of the present work. This agrees with simulations where we have not spotted a significant shift for the used concentrations ≤ 0.2.

The aspect that most interests us here is, however, not the equilibrium behavior but the dynamics of the liquid-gas phase transition. As in Section 4.2.1 we start at a $\mu < -2$ with a liquid covered substrate, i.e., in a region where the final state without nanoparticles corresponds to the vapour phase. Now, however, although the liquid evaporates the nanoparticles remain. Depending on the particular parameter values chosen one finds final structures that do not change any more on short time scales. They might, however, slowly evolve, e.g. by coarsening on long time scales [95]. The final "dried-in" structures depend on the pathway of evaporative dewetting (i.e. on kT, μ, the interaction constants ε_{ij}, nanoparticle concentration ϕ and mobility M) and range from labyrinthine to polygonal network structures or holes in a dense particle layer. Typical snapshots from the evolution of a layer of solution are shown in Fig. 4.7. As before, the evaporative dewetting process of the solvent follows either a nucleation and growth [Fig. 4.7(b)]

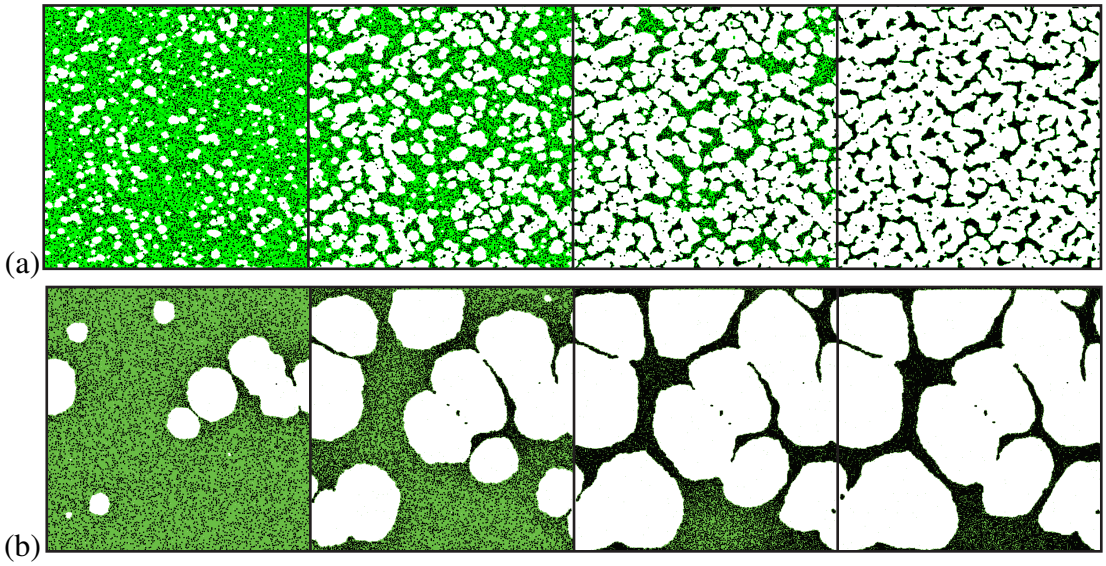

Figure 4.7: Snapshots from typical evaporative dewetting processes with nanoparticles in the case of (a) a spinodal-like process at $\mu = -2.55$ and (b) of nucleation and growth of holes at $\mu = -2.3$. Starting condition homogeneous liquid film with homogeneously distributed particles. The number of Monte Carlo steps is indicated in the individual panels (top: 10, 15, 20, 100 bottom: 100, 200, 300, 400); $\varepsilon_{nn} = 2$, $\varepsilon_{nl} = 1.5$, $M = 50$, $\phi = 0.2$. The remaining parameters are as in Fig. 4.6. Particles are black, liquid is green and the empty substrate is white.

or a spinodal-like [Fig. 4.7(a)] pathway. Following the mean field argument as discussed above, we expect again a shift by $-2(\varepsilon_{nl} - 1)\phi$ for the limiting curve $\mu_{\mathrm{ms}}(kT)$ which separates the two processes in the parameter plane. However, due to fluctuations this border is elusive when scrutinised numerically, therefore we will not try to compare simulations to the prediction.

At first sight, however, one might get the impression that the particles act as a type of passive tracer that preserves the transient volatile dewetting structures of the solvent. This idea was put forward in Refs. [73, 72, 127] in the context of experiments on dewetting aqueous solutions of macromolecules and provides an explanation for some of the basic features of the observed network structures. One can also employ this hypothesis to explain some of the structures observed in the present study, such as the network and spinodal structures shown in Fig. 4.7. The simulations indicate, however, that the nanoparticles are not simply passive tracers. Although the particles primarily just follow the solvent, they play an important role in several phases of the process.

First, the particles may influence the nucleation process in the metastable parameter region, beyond the "shift" in μ predicted by the mean field considerations above. Although our simulations seem to indicate that the nucleation rates actually depend on the particles themselves, we cannot quantify the effect at present. We leave this question for future investigations and focus here on the second and more pronounced influence. Second, for a low mobility of the particles, i.e. for a slow diffusion of particles as compared to the evaporation of the solvent, the nucleated holes might grow in an unstable manner as illustrated in Fig. 4.8. The transverse instability of the dewetting front responsible for this effect is analysed in more detail in the following section.

4.3 Fingering instability

A straight evaporative dewetting front without nanoparticles present moves with a constant mean velocity $\bar{v}$ (averaged over the transverse direction). The velocity only depends on the driving chemical potential. The local velocity, however, fluctuates with temperature. The fluctuations are illustrated in the column of snapshots at the right of Fig. 4.5. Therefore, the local front position also fluctuates around the steadily advancing or receding mean position. The velocity is easily measured numerically for driving forces small enough that the nucleation of additional holes is not very probable during the time of measurement. This is the case for $\mu \geq -2.4$. One finds that the velocity increases linearly with the driving force.

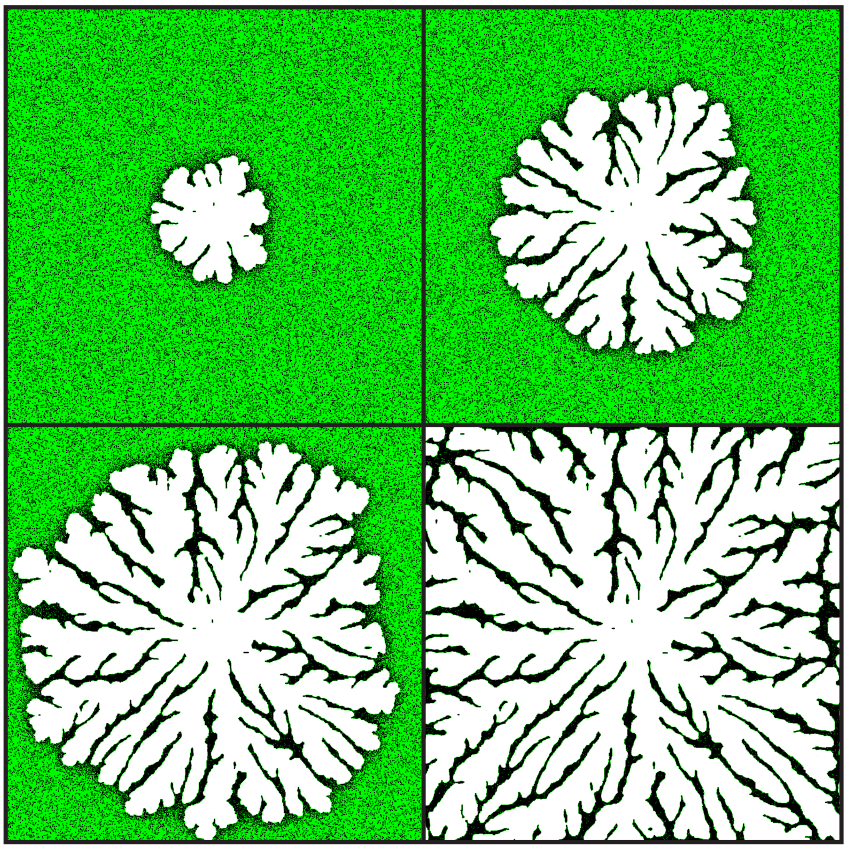

Figure 4.8: Snapshots illustrating the unstable growth of a nucleated hole in a film of nanoparticle solution. The strong branched fingering caused by the nanoparticles can be seen clearly. From top left to bottom right the number of Monte Carlo steps is 450, 1200, 1800, and 3000. Nanoparticle related parameters are $\varepsilon_{nn} = 2$, $\varepsilon_{nl} = 1.5$, $\mu = -2.3$, $M = 5$, $\phi = 0.2$. The remaining parameters are as in Fig. 4.6. Particles are black, liquid is green and the empty substrate is white.

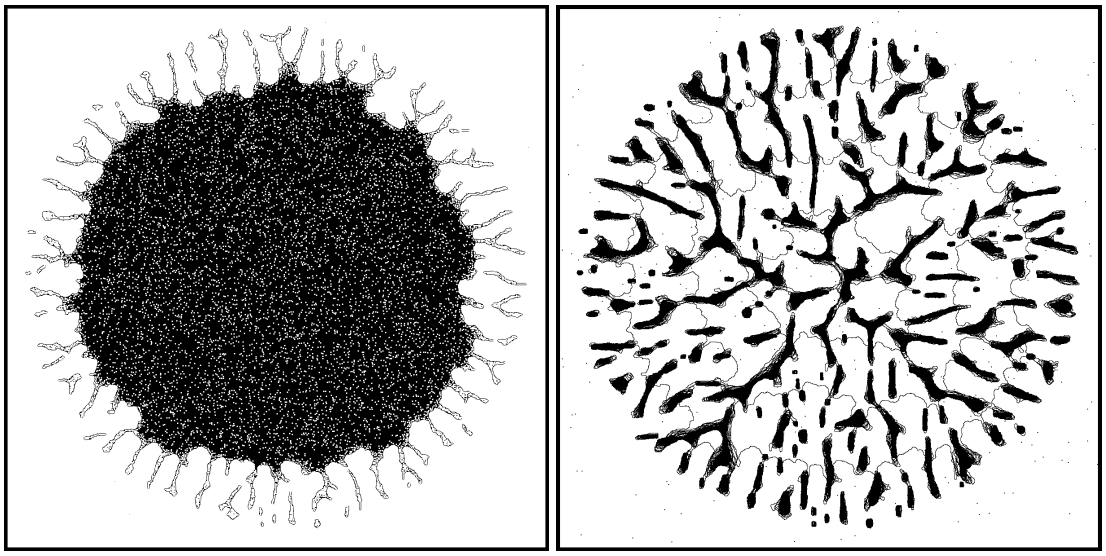

Figure 4.9: Snapshots in time illustrating an unstable droplet. The initial conditions for simulations are a droplet sitting on a horizontal substrate. The fingering caused by the nanoparticles can be seen. Simulations parameters are: the number of Monte Carlo steps is 1000 (left image), 5000 (right image), $\varepsilon_{nn} = 2$, $\varepsilon_{nl} = 1.5$, $\mu = -2.2$, $M = 2$, $\phi = 0.1$, $kT = 0.2$.

Adding diffusing nanoparticles to the solvent changes the front behavior dramatically as it may become transversally unstable. Such an unstable front does not only fluctuate around a continuously receding mean position but fingers stay behind permanently (for the front instability of a growing circular hole, Fig. 4.8, or for simulation of a droplet sitting on a horizontal substrate, Fig. 4.9 and Fig. 4.18). To elucidate the underlying mechanism we will in the next paragraphs discuss the influence of the individual system parameters on the instability, i.e., the influence of chemical potential μ, particle concentration ϕ, and mobility M.

For each dependency we present snapshots of the final dried in nanoparticle structure corresponding to the dried in patterns observed in experiment. We add, however, thin lines that correspond to positions of the dewetting front at equidistant times throughout the evolution. The final branched patterns we characterise in a rather simple but effective manner. We determine an averaged fingers number by dividing the side length of the computational square domain by the fingers number. The latter is obtained by counting the fingers on each line orthogonal to the mean direction of front motion (here the y direction) and averaging over the y-range where fingers exist. The underlying hypothesis that the finger patterns are "stationary" will be discussed and checked below. Attempts to determine a mean distance of fingers employing a 1-D Fourier transform unfortunately did not give meaningful results because of the strong side-branching

(see snapshots below). Note, that the finger number corresponds to a wave number rescaled by $2\pi/L$ where L is the side length of the computational domain (that is fixed throughout this section and corresponds to about 1.2μm.).

4.3.1 Dependence on chemical potential

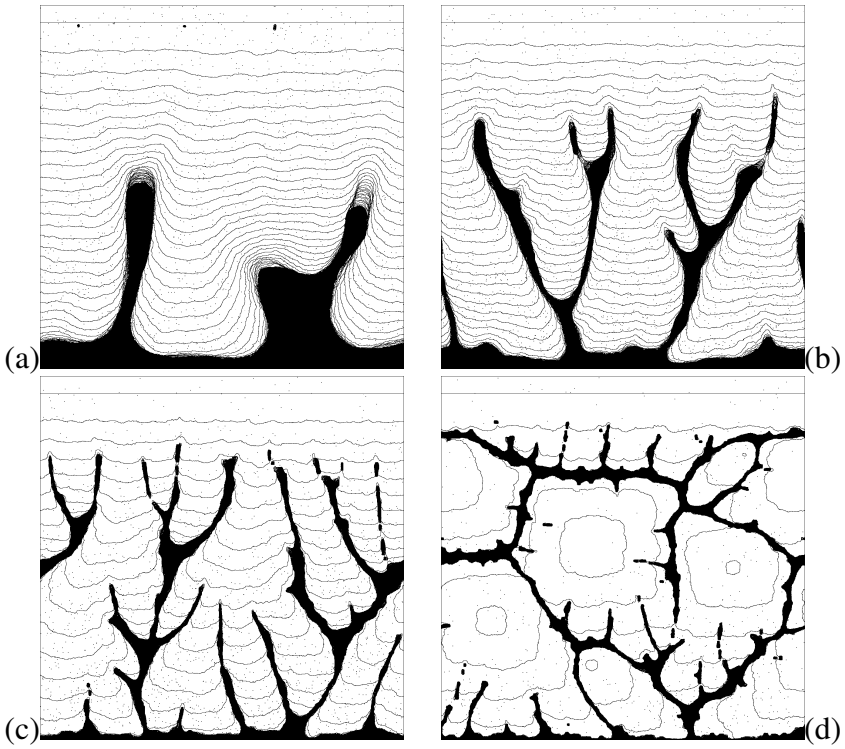

Figure 4.10: Final "dried-in" branched fingering structure for evaporative dewetting of a nanoparticle solution for different driving forces, i.e., chemical potential (a) $\mu = -2.1$, (b) $\mu = -2.2$, (c) $\mu = -2.3$, and (d) $\mu = -2.4$. Thin lines correspond to positions of the dewetting front at equidistant times with $\Delta t = 333$ (a), and $\Delta t = 166$ (b, c, d). The domain size is 1200×1200, $M = 20$, $\phi = 0.1$, $kT = 0.2$, $\varepsilon_{nn} = 2$, and $\varepsilon_{nl} = 1.5$.

First, we focus on the influence of the driving force, i.e., the chemical potential. Fixing the particle concentration to $\phi = 0.1$ and the mobility to $M = 20$, the final structures observed for various values of μ are shown in Fig. 4.10 whereas Fig. 4.12 shows the dependence of the mean finger number on the chemical potential. Fig. 4.11 shows final simulation structures for different values of chemical potential but in the case of a nucleated hole (hole as initial starting condition). The driving force increases for decreasing μ and the number of fingers increases roughly linearly. Again, for $\mu \leq -2.4$ nucleation becomes more probable and we observe a

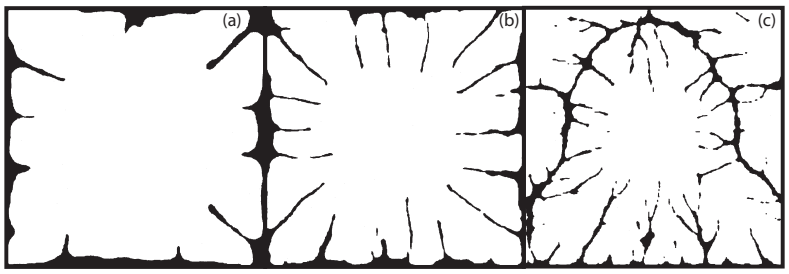

Figure 4.11: Final snapshots illustrating the unstable growth of a nucleated hole in a film of nanoparticle solution for different values of chemical potential: (a) $\mu = -2.2$, (b) $\mu = -2.3$, (c) $\mu = -2.4$. The lattice size is 1200×1200, number of Monte Carlo steps is 3000 and the other simulation parameters are $\varepsilon_{nn} = 2$, $\varepsilon_{nl} = 1.5$, $\phi = 0.1$, $kT = 0.2$, $M = 20$.

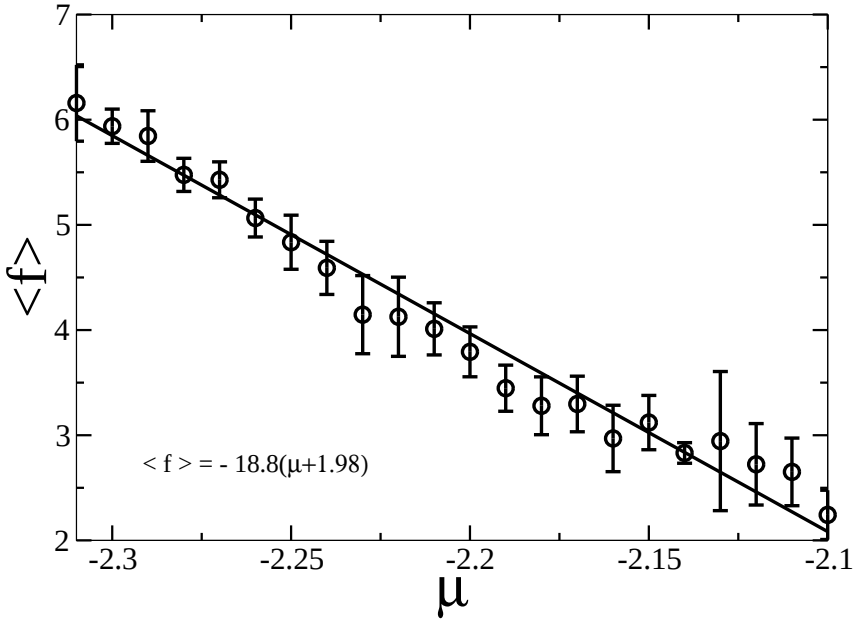

Figure 4.12: Dependence of mean finger number $< f >$ of the final dried in structures (determined as described in the main text) on chemical potential μ. Every data point corresponds to the mean value of 7 simulations; error bars indicate the corresponding standard deviation. The solid line corresponds to a linear mean-square fit with coefficients given in the plot. The remaining parameters are as in Fig. 4.10.

random polygonal network. The side-branches of the polygonal pattern clearly result from the transverse instability [see Fig. 4.10(d)].

Further inspection of Fig. 4.10 results in the following observations:

(i) Both the wavenumber and the growth rate of the front instability increase with decreasing μ. A faster growth translates into longer fingers in the "dried in" structure, i.e., fingers that extend further in Fig. 4.10. Starting from the same initial front position, the fingers appear much earlier in panel (c) than in panels (b) or (a).

(ii) The front contours taken at equidistant times indicate that the front is already strongly disturbed before the instability becomes manifest in a deposited finger, i.e., parts of the front slow down before actually stopping (and depositing material). This is especially well visible in Fig. 4.10(a).

(iii) The dried-in fingering structure is not entirely frozen as the chosen parameters values are in a "fluxional" regime [95]. This is especially well visible at the tips of the fingers in Fig. 4.10(a) that continue to retract very slowly, or in Fig. 4.10(b) where a thin part of the rightmost finger breaks and slowly retracts as well. Eventually, this will lead to a long-time coarsening of the finger structure.

(iv) It is remarkable that even when fingers are left behind the local distance between consecutive front contours seems to be constant in each of the panels [beside the regions discussed in (iii)]. One expects, however, that the front velocity depends on the local particle concentration and the mobility of the particles. The observation of a constant velocity indicates that the front instability is related to an auto-optimisation of the front velocity. This is analogous to an effect described for dewetting polymer films [102]. There, a moving dewetting front "expels" part of the liquid rim and leaves the liquid behind in the form of deposited droplets. The instability avoids a slowing down of the dewetting front. Here, some of the particles that the evaporative dewetting front collects are expelled and deposited in fingers when too many are collected by the front.

Measurements of the front velocity for different μ and particle concentrations indeed show that the mean velocity is constant and depends linearly on μ, Fig. 4.15.

Next steps are to study and discuss the influence of the other two important parameters (particle concentration and mobility) on fingering instability. Also we have to establish the role of attraction strengths between nanoparticle (ε_{nn}) and between nanoparticle and liquid (ε_{nl}) on front instabilities.

4.3.2 Dependence on particle concentration

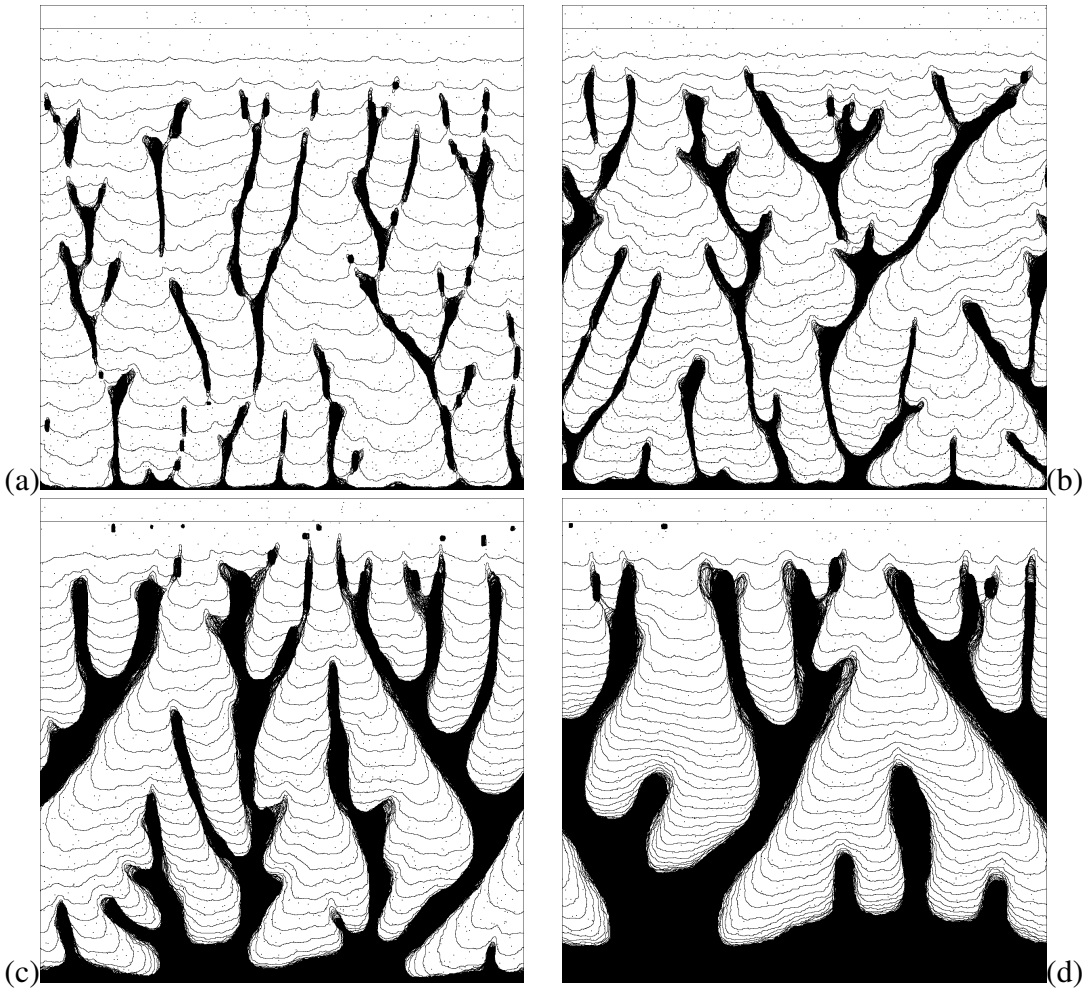

Figure 4.13: Final "dried in" branched fingering structure for evaporative dewetting of a nanoparticle solution for different nanoparticle concentration (a) $\phi = 0.05$, (b) $\phi = 0.10$, (c) $\phi = 0.20$, and (d) $\phi = 0.30$. Thin lines correspond to positions of the dewetting front at equidistant times with $\Delta t = 166$ (a, b), $\Delta t = 333$ (c) and $\Delta t = 500$ (d). The domain size is 1200×1200, $M = 10$, $\mu = -2.2$, $kT = 0.2$, $\varepsilon_{nn} = 2$, and $\varepsilon_{nl} = 1.5$.

We have also examined the influence of the nanoparticle concentration ϕ on the fingering. Fixing the chemical potential at $\mu = -2.2$ and the mobility at $M = 10$, the final structures are shown for various values of ϕ in Fig. 4.13. Fig. 4.14 shows final "dried in" branched fingering structure for evaporative dewetting of a nanoparticle solution for different nanoparticle concentration but in the case where the simulations are started with an initial circular hole as starting condition. From an initial inspection of Fig. 4.13 and Fig. 4.14 one might get the erroneous impression that the finger number increases with concentration. However, the statistics of many runs shows that the number is nearly independent of the particle concentration. The fingers

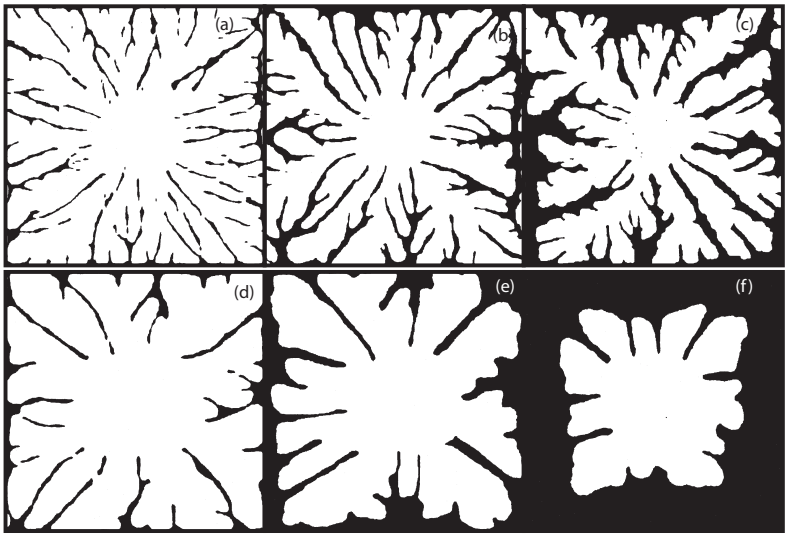

Figure 4.14: Final snapshots illustrating the unstable growth of a nucleated hole in a film of nanoparticle solution for different values of concentration. From left to right the concentration of nanoparticle is $\phi = 0.1$, $\phi = 0.2$, $\phi = 0.3$. Top row is for $\mu = -2.3$ and the bottom row is for $\mu = -2.2$. The lattice size is 1200×1200, number of Monte Carlo steps is 3000 and the other simulation parameters are $\varepsilon_{nn} = 2$, $\varepsilon_{nl} = 1.5$, $kT = 0.2$, $M = 10$.

only become thicker with increasing concentration. This indicates that the fingering is controlled by the "dynamical" parameters responsible for the ratio of the time scales for diffusion of the particles and motion of the evaporative front (i.e., mobility and chemical potential). As the influence of the chemical potential has already been established in Section 4.3.1 we focus below in Section 4.3.3 on the influence of mobility.

Before we do so we summarise in Fig. 4.15 results for the dependence of the global average front velocity on chemical potential and particle concentration. For all investigated concentrations the velocity decreases linearly with increasing chemical potential, i.e., with decreasing driving force. If we fix the chemical potential, the dewetting process is slower for higher particle concentrations. This implies that the finger number is not directly related to the mean front velocity, a result that will be discussed in the Conclusion.

4.3.3 Dependence on mobility

Fixing the particle concentration at $\phi = 0.1$ and the chemical potential at $\mu = -2.2$, we show in Fig. 4.16 the final structures observed for selected values of mobility, M. Fig. 4.17 shows also final simulation structures for different values of mobility but in the case of circular

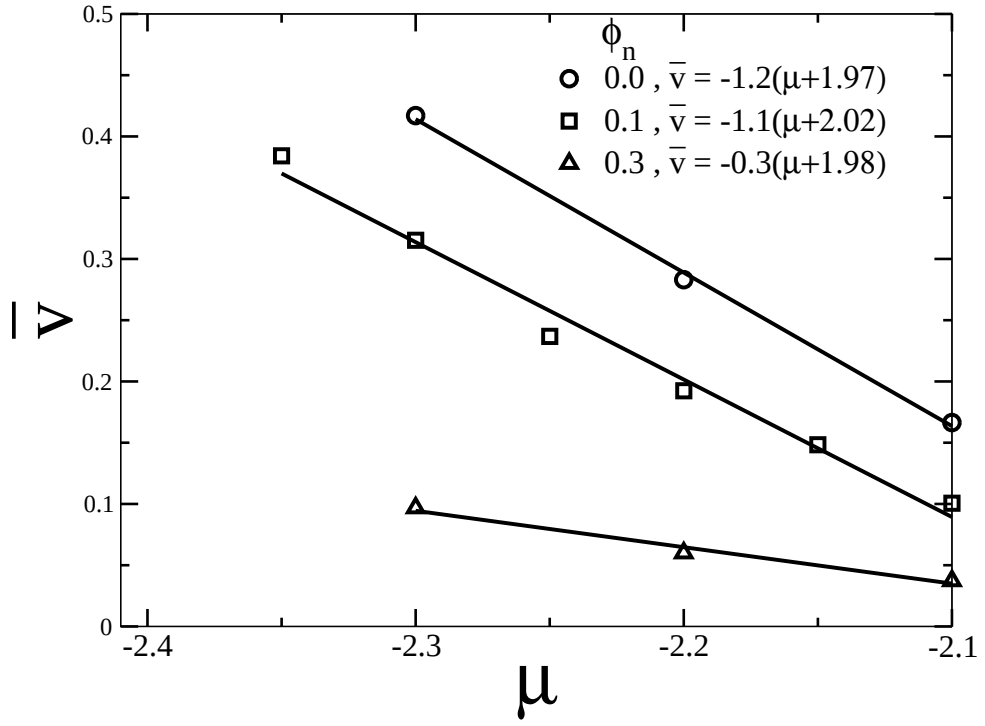

Figure 4.15: Dependence of mean front velocity on chemical potential μ and for selected particle concentrations ϕ as given in the legend. The thin lines correspond to linear regression fits with coefficients as given in the plot. The used domain size is 1200×1200, $M = 20$, $kT = 0.2$, $\varepsilon_{nn} = 2$, and $\varepsilon_{nl} = 1.5$. The velocity is averaged over 7000 MC steps or the number of steps it takes to "dry" the substrate, whichever is smaller.

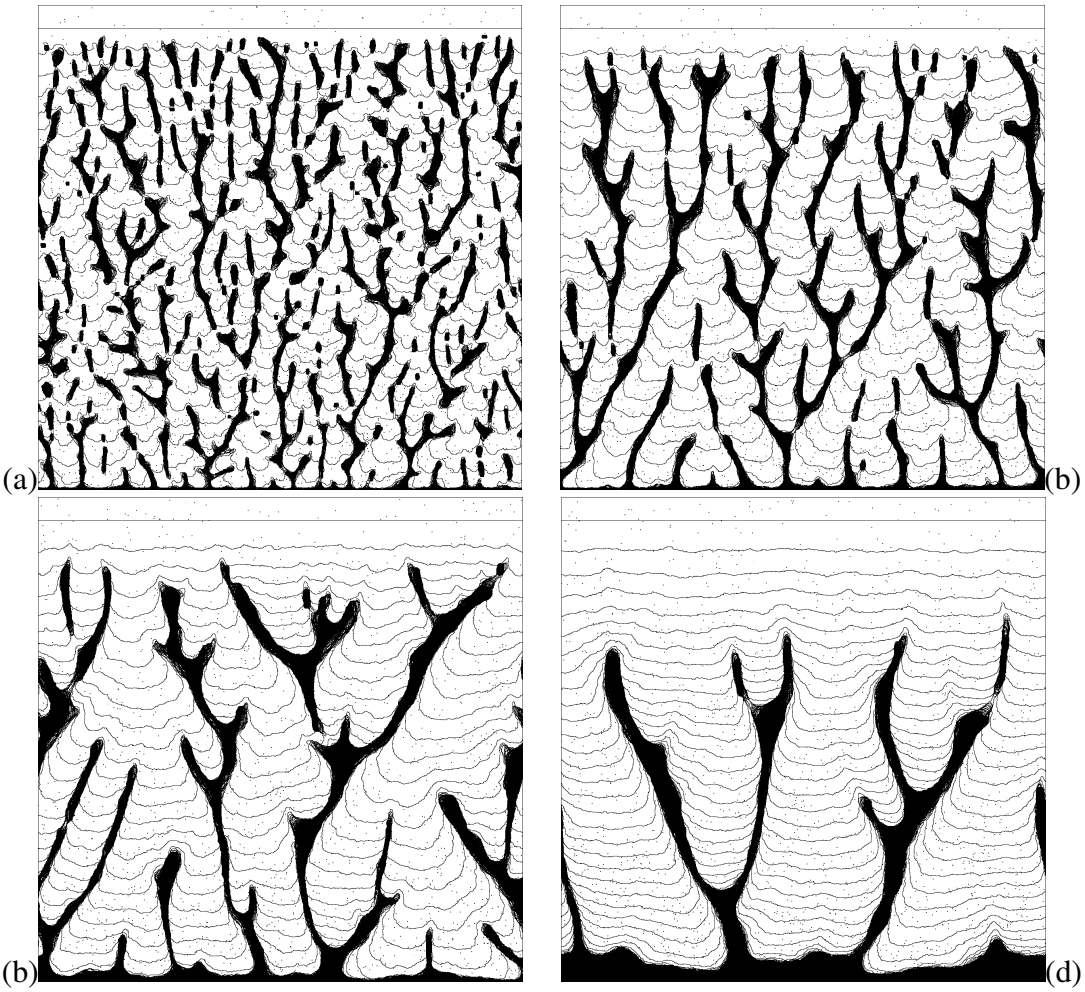

Figure 4.16: Final dried in branched fingering structure for evaporative dewetting of a nanoparticle solution for different nanoparticle mobilities (a) $M = 2$, (b) $M = 5$, (c) $M = 10$, and (d) $M = 20$. Thin lines correspond to positions of the dewetting front at equidistant times with $\Delta t = 166$. The domain size is 1200×1200, $\phi = 0.1$, $\mu = -2.2$, $kT = 0.2$, $\varepsilon_{nn} = 2$, and $\varepsilon_{nl} = 1.5$.

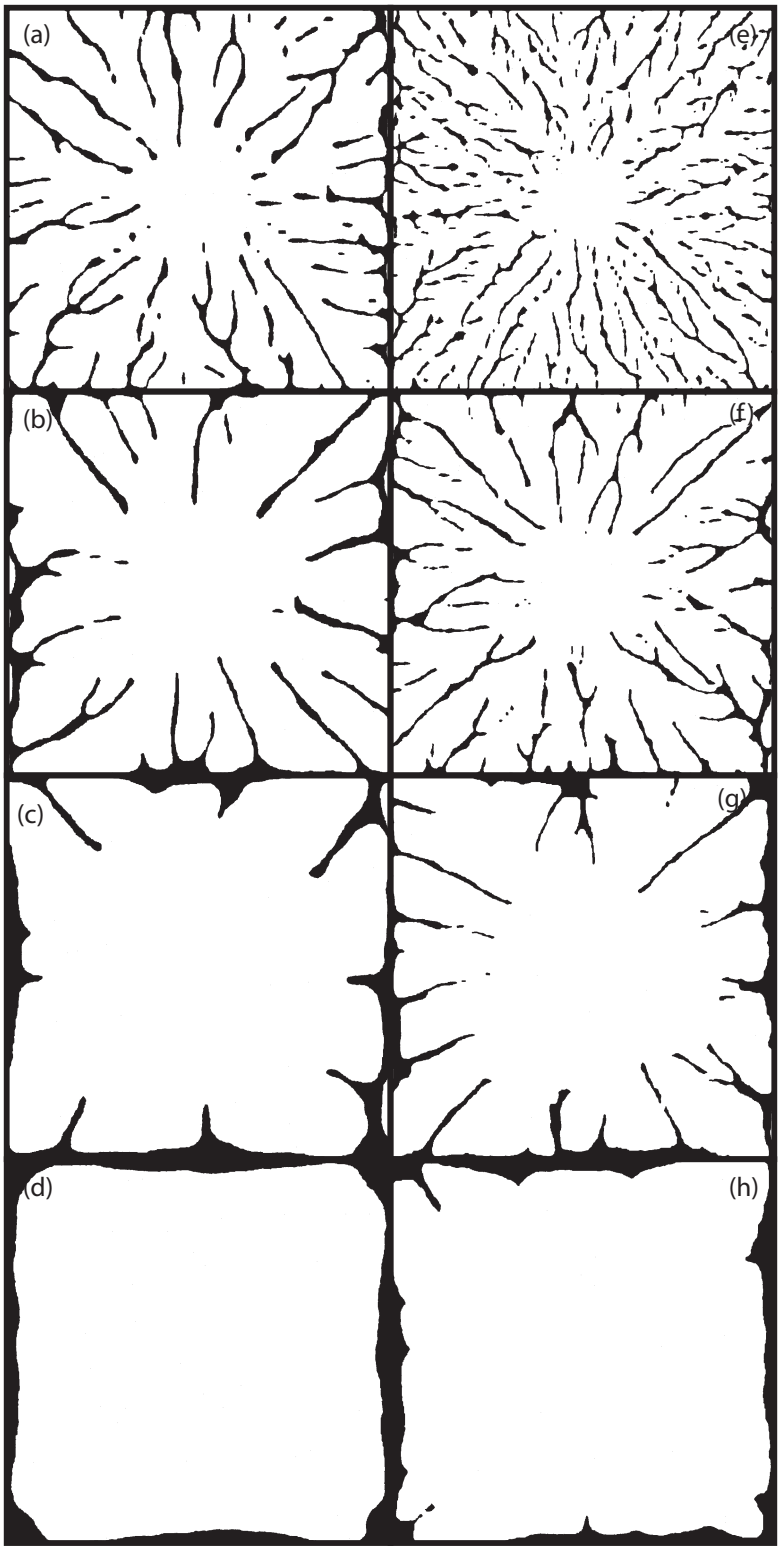

Figure 4.17: Final snapshots illustrating the unstable growth of a nucleated hole in a film of nanoparticle solution for different values of mobility M. From top to bottom the mobility value is $M = 5$, $M = 10$, $M = 20$, $M = 40$. For the left column $\mu = -2.2$ and for the right column $\mu = -2.3$. The lattice size is 1200×1200, number of Monte Carlo steps is 3000 and the other simulation parameters are $\varepsilon_{nn} = 2$, $\varepsilon_{nl} = 1.5$, $\phi = 0.1$, $kT = 0.2$.

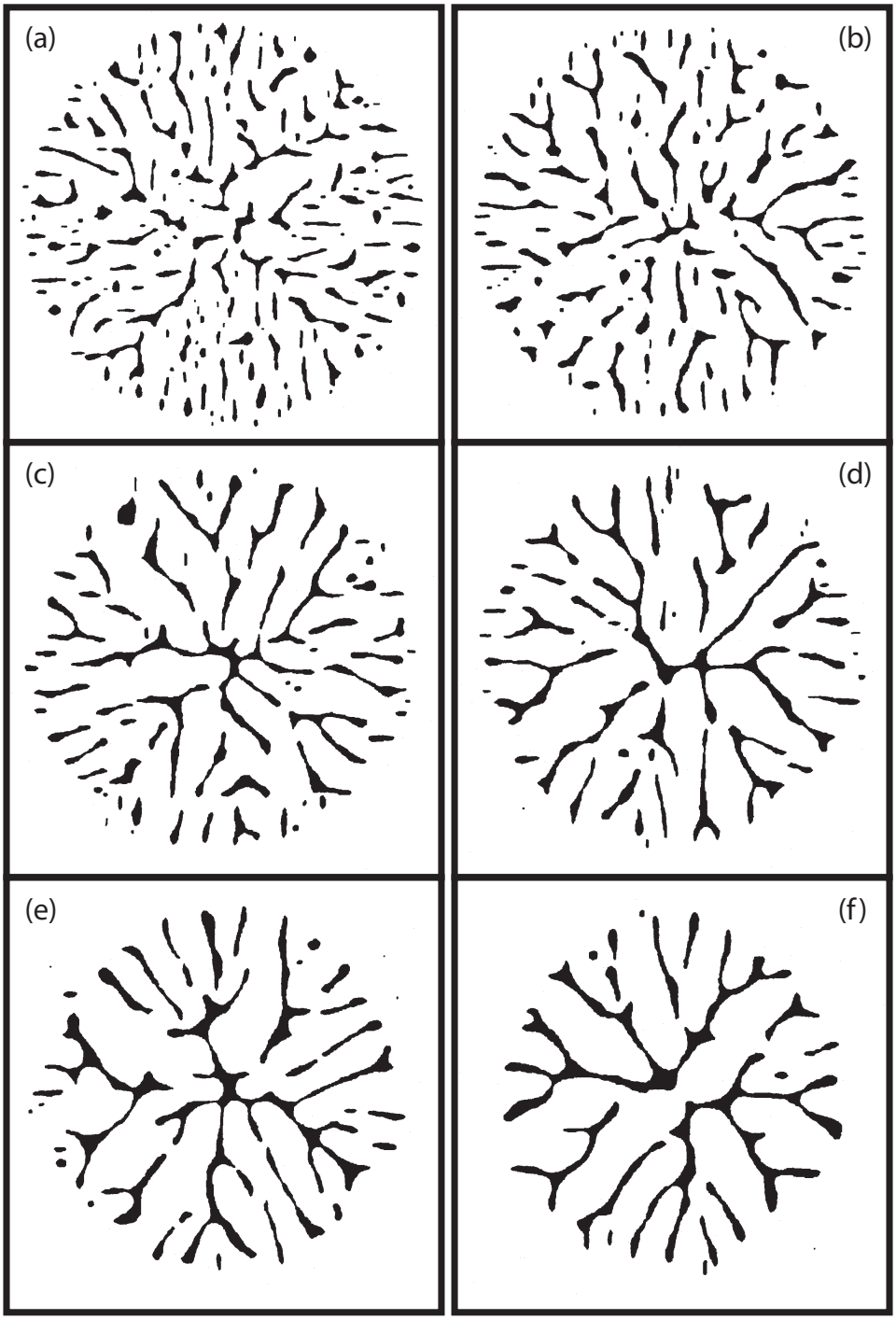

Figure 4.18: Final nanoparticle structures for an unstable droplet for different values of mobility, M: (a) $M = 2$, (b) $M = 3$, (c) $M = 4$, (d) $M = 5$, (e) $M = 6$, (f) $M = 7$. The others simulations parameters are: the lattice size is 1200×1200, number of Monte Carlo steps is 5000, $\varepsilon_{nn} = 2$, $\varepsilon_{nl} = 1.5$, $\varepsilon_{ll} = 1$, $\mu = -2.2$, $\phi = 0.1$, $kT = 0.2$. Increasing mobility (from (a) to (f)) the number of fingers is decreased. These results are discussed in detail in the next sections of this chapter.

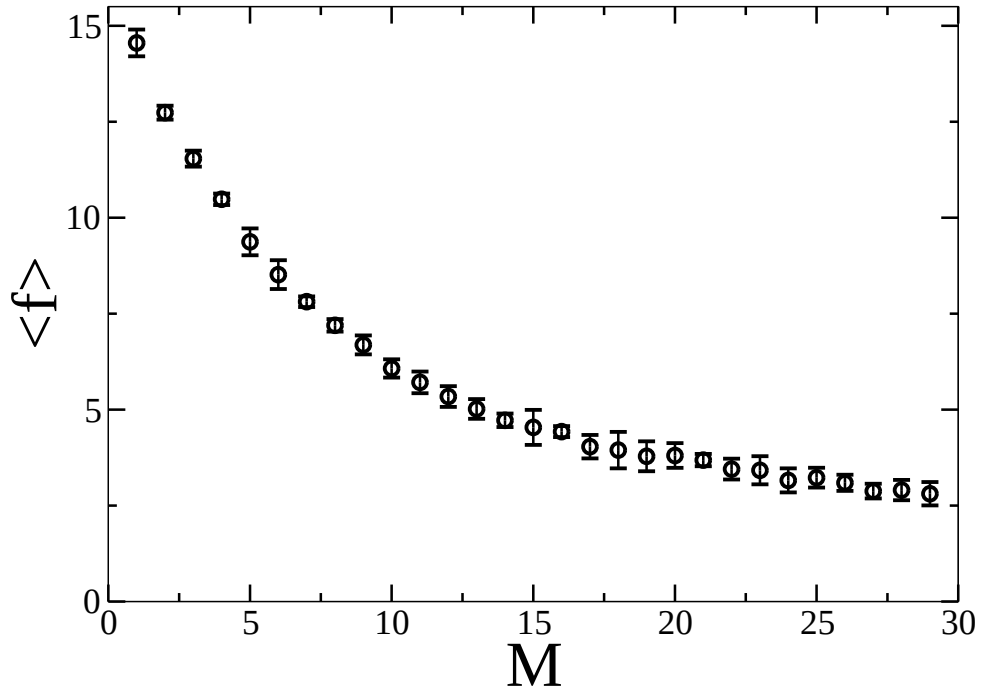

Figure 4.19: Dependence of mean finger number $< f >$ of the final dried in structures on particle mobility M. Every data point corresponds to the mean value of 7 simulations; error bars indicate the corresponding standard deviation. The remaining parameters are as in Fig. 4.16.

hole as initial condition, and Fig. 4.18 for a droplet sitting on horizontal substrate. Fig. 4.19 shows the dependence of mean finger number on mobility. One sees at once that mobility is very influential in the fingering process. For decreasing mobility of the particles the number of fingers increases strongly. As was observed for the influence of the chemical potential, the growth rate of the instability increases with increasing finger number, i.e., decreasing mobility. This is manifest in Fig. 4.16 by the later emergence of fingers for larger M, i.e., in the increasing distance of the finger tips from the upper domain boundary.

The systematic picture that emerges from the preceding three sections allows us to identify the primary factors influencing the fingering instability. It becomes obvious that they are of dynamical nature. Mobility is the major factor. The faster the nanoparticles can diffuse away from the dewetting front, the less likely the instability becomes as the front is not fast enough to "collect" the particles efficiently. This directly corresponds to the observation that the fingering becomes more intense with increasing driving force, i.e., lower chemical potential. Then the relative diffusivity is held constant (mobility M) but the mean front speed increases with decreasing μ. The greater the number of particles collected at the moving front, the more likely become lateral density fluctuations that lead to self-amplifying variations of the local front ve-

locity. Note, however, that up to this point we kept all the interaction parameters ε_{ij} fixed. We expect them to influence the feedback loop because, for example, a stronger particle-particle interaction ε_{nn} should support clustering. But one has to be cautious because the process is of dynamic character. Therefore it is difficult to predict whether a larger ε_{nn} implies less or more fingers. This question will be discussed below in Section 4.3.5.

Next, however, we will check the assumption of stationarity of the finger patterns that we have used above to introduce the measure of the mean finger number.

4.3.4 Stationarity of finger pattern

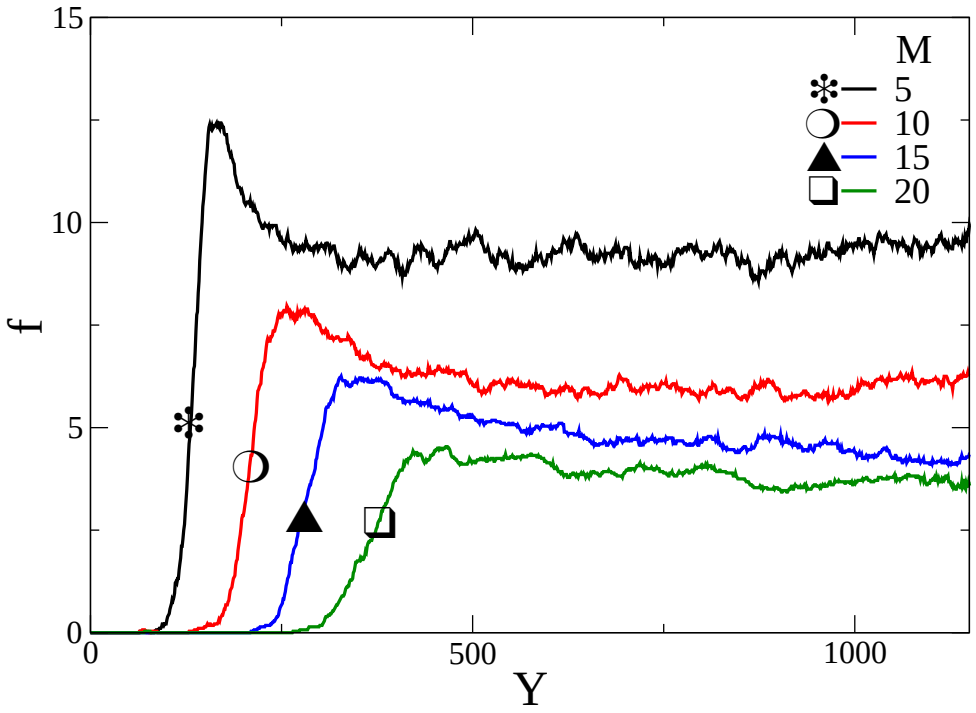

Figure 4.20: Dependence of finger number on streamwise coordinate (i.e., y-direction) for various values of mobility as given in the legend. As the structures are fixed when they stay behind the front increasing y also indicates increasing time. The figure may be read as a space-time plot of the fingering at the moving dewetting front. Each curve corresponds to the average of 28 runs. The remaining parameters are as in Fig. 4.16.

In Sections 4.3.1 to 4.3.3 we have used the mean finger number to characterise the parameter dependency of the fingering patterns. We noted that it only represents a trustworthy measure if the fingering process is stationary. By "stationary" we mean that the main properties of the pattern do not depend on the streamwise position. In other words the moving dewetting front

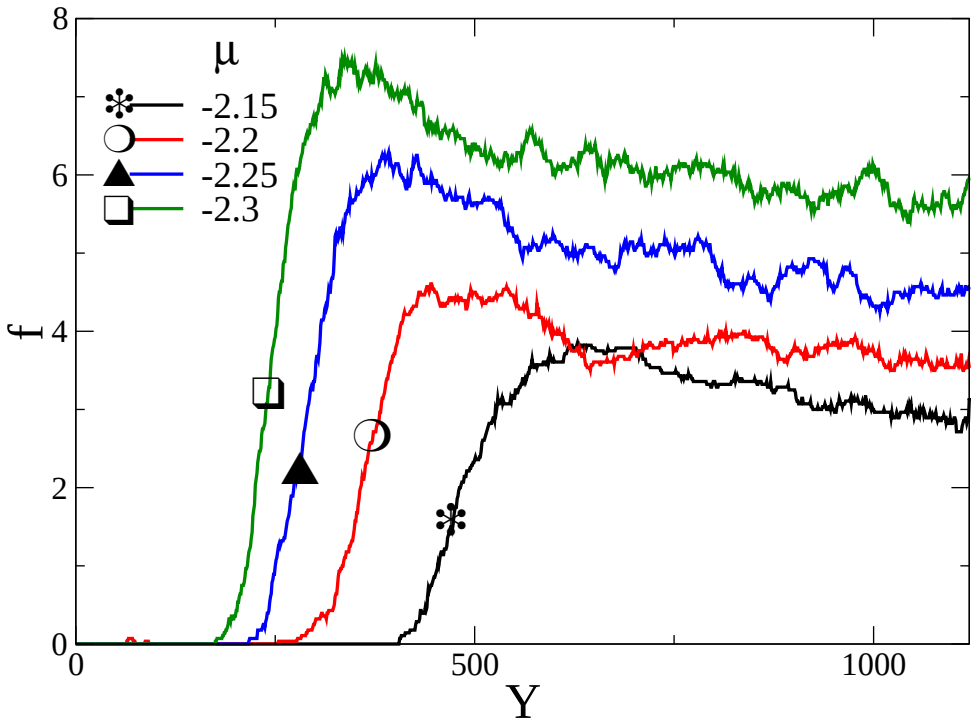

Figure 4.21: Dependence of finger number on streamwise coordinate (i.e., y-direction) for various values of the chemical potential as given in the legend. Each curve corresponds to the average of 28 runs. The remaining parameters are as in Fig. 4.10.

moves on average with a constant velocity and deposits on average the same amount of material in the same number of fingers.

To check this strong assumption we plot in Figs. 4.20 and 4.21 the dependence of finger number on the streamwise co-ordinate (y-co-ordinate) for various values of the mobility and chemical potential, respectively. To smooth out fluctuations each curve represents the mean of 28 runs. As the fingers stay fixed after being deposited behind the front, an advance in y also indicates passing time. We note in passing that all "snapshots" above that show dried-in final structures can as well be read as space-time plots tracking the particle-deposition at the moving dewetting front. Inspecting the curves we note that they have some properties in common: (i) finger number starts from zero at some value $y = y_s$ well behind the initial position of the front at $y = 60$; (ii) the finger number grows exponentially on a typical length scale related to the (linear) growth rate of the fingering instability; (iii) a maximal finger number is reached before the number decreases again and settles onto a stationary level. The decay corresponds to a small coarsening of fingers and can be seen in several of the snapshots above. (iv) Fluctuations around the stationary level are small, i.e., on average as many new fingers are created (branch tips in

the final image) as vanish when fingers join pairwise (at the branching points).

Our conclusion is that the mean finger number as used above is a valid measure because the y-range where the initial overshooting occurs is relatively small, and also the overshoot itself is normally below 20% of the mean stationary value. The resulting error is small as compared to the natural variance that we found between different runs. Note, however, that for several curves in Fig. 4.21 the decay after the initial maximum is relatively slow and the stationary value is not reached for our system size. This corresponds to a very slow coarsening of fingers as the front recedes.

4.3.5 Influence of interaction parameters

We have mentioned in Section 4.2 the hypothesis (put forward in [127] for a related system) that the ongoing pattern formation and the properties of the receding dewetting front mainly result from the dynamics of the liquid-gas phase transition. The nanoparticles were seen as passive tracers. This describes well the situation in the spinodal-regime (taking into account that the mean field parameters are slightly changed by the particles). We have then shown that this picture has to be amended because the particles have an important influence during crucial phases of dewetting. Most notably, they are solely responsible for the transverse instability of the dewetting front leading to the branched finger patterns analysed in detail in the present Section 4.3.

The analysis up to now has been performed by fixing the interaction parameters ε_{ij} at convenient values: the liquid-liquid interaction serves as an energy scale, i.e., $\varepsilon_{ll} = 1$; the particles attract each other slightly more than particles attract liquid ($\varepsilon_{nn} = 2$, $\varepsilon_{nl} = 1.5$). This ensures that particle-liquid phase separation does not generally occur in the bulk solution, but also that particle clusters are likely to form at higher particle concentrations. This resembles the situation in the experiments and was also used in most computations in Refs. [95, 69].

In the following we will analyse the influence of ε_{nn} and ε_{nl} on the fingering instability. A few simulation snapshots for different values of ε_{nn} are given in Fig. 4.22 for the case of nucleated hole (a small circular hole is considered as initial starting condition for the simulations). In particular, we are interested in a possible coupling of the front instability and the demixing of particles and liquid. In our scaling ($\varepsilon_{ll} = 1$), demixing will occur for large ε_{nn} (at fixed ε_{nl}) or small ε_{nl} (at fixed ε_{nn}), i.e., for large ratios ε_{nn} / ε_{nl}.

Fig. 4.23 presents results for the average number of fingers when changing ε_{nn} in the range

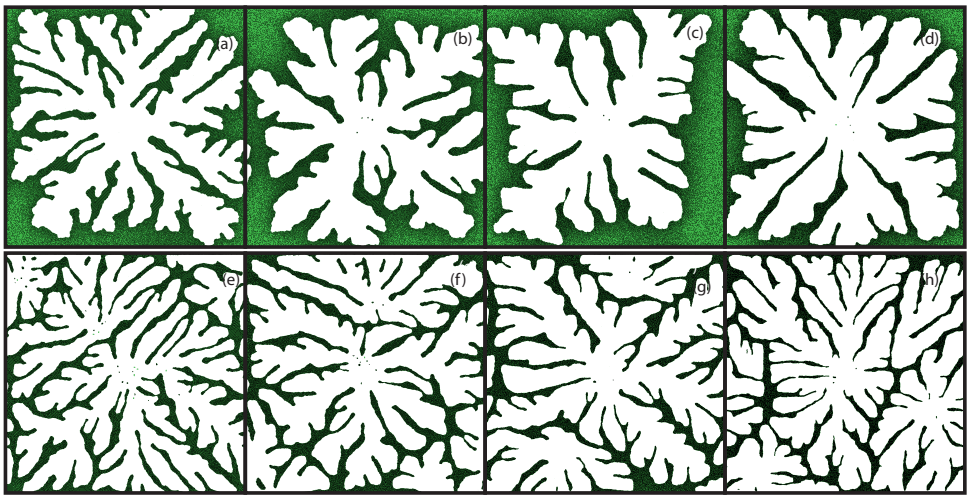

Figure 4.22: Snapshots illustrating fingering structure for different values of ε_{nn} in the case of hole as initial starting condition. The corresponding values for ε_{nn} are from left to right: $\varepsilon_{nn} = 1.5$, $\varepsilon_{nn} = 1.6$, $\varepsilon_{nn} = 1.7$, $\varepsilon_{nn} = 1.8$. Top row corresponds to $\mu = -2.3$ and the bottom row is for $\mu = -2.4$. The number of Monte Carlo steps is 3000 and the remaining parameters are: domain size 1200×1200, $kT = 0.2$, $M = 5$, $\phi = 0.2$, $\varepsilon_{nl} = 1.5$. Particles are black, liquid is green and the empty substrate is white.

between 1.4 and 2.5. Inspecting the figure one can distinguish four regions:

(i) At small $\varepsilon_{nn} < 1.95$ the particular strength of the interaction has nearly no influence; only a slight decrease of the finger number with increasing ε_{nn} is discernible. We call this the "transport regime" as only the transport properties play a role. A few simulation snapshots for this case are given in Fig. 4.22.

(ii) In an intermediate region $1.95 < \varepsilon_{nn} < 2.15$ the finger number increases steeply by about a factor of three. Fingers emerge at the receding front and there is no demixing at all going on in the liquid bulk behind the front. What we see is still a pure front instability that is, however, strongly influenced by the ratio of interaction parameters. We interpret this as a front-induced demixing that leads to fingering. In other words, the front itself acts as a "nucleation site" for demixing. We call this a "demixing-induced front instability". Note, however, that fingering still leads to a strongly anisotropic fingering pattern. Although the fingers break at some places they do in general not break up into small nanoparticle islands.

(iii) Increasing ε_{nn} further above 2.15, the finger number decreases again till about $< f >=$

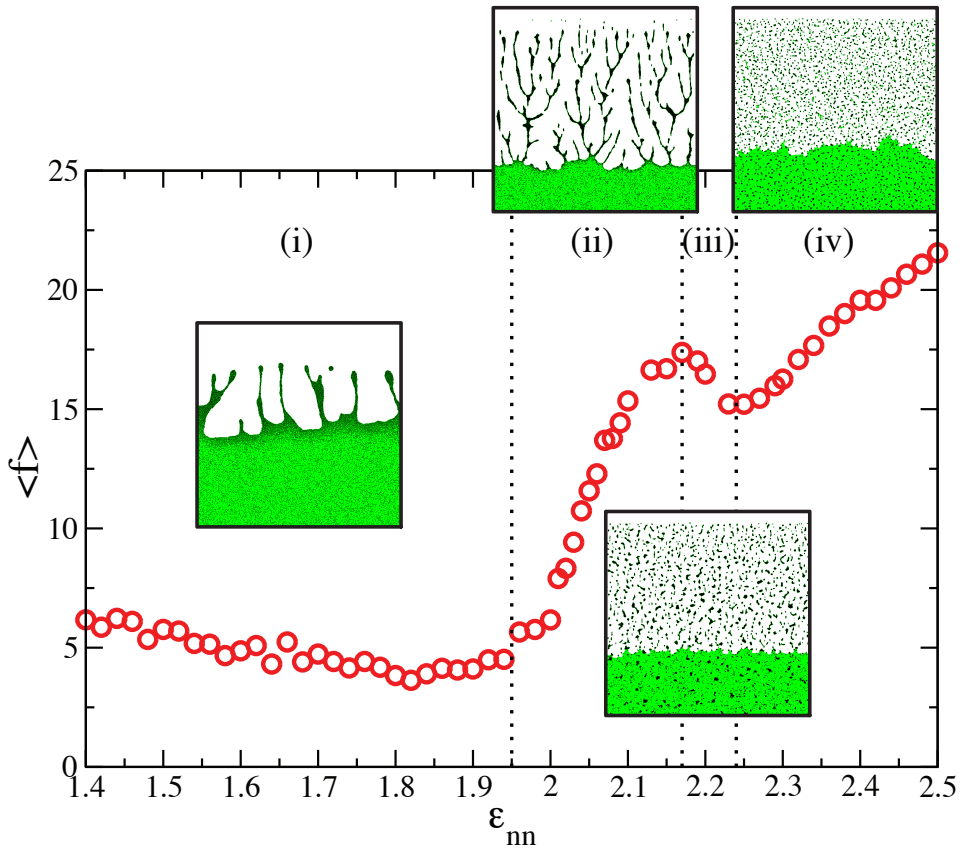

Figure 4.23: Dependence of the mean finger number on the particle-particle interaction strength ε_{nn}. The regions marked (i) to (iv) are discussed in the main text. The remaining parameters are: domain size 1200×1200, $kT = 0.2$, $M = 20$, $\mu = -2.2$, $\phi = 0.1$, $\varepsilon_{nl} = 1.5$. The insets give typical snapshots obtained in the four different regions. Particles are black, liquid is green and the empty substrate is white.

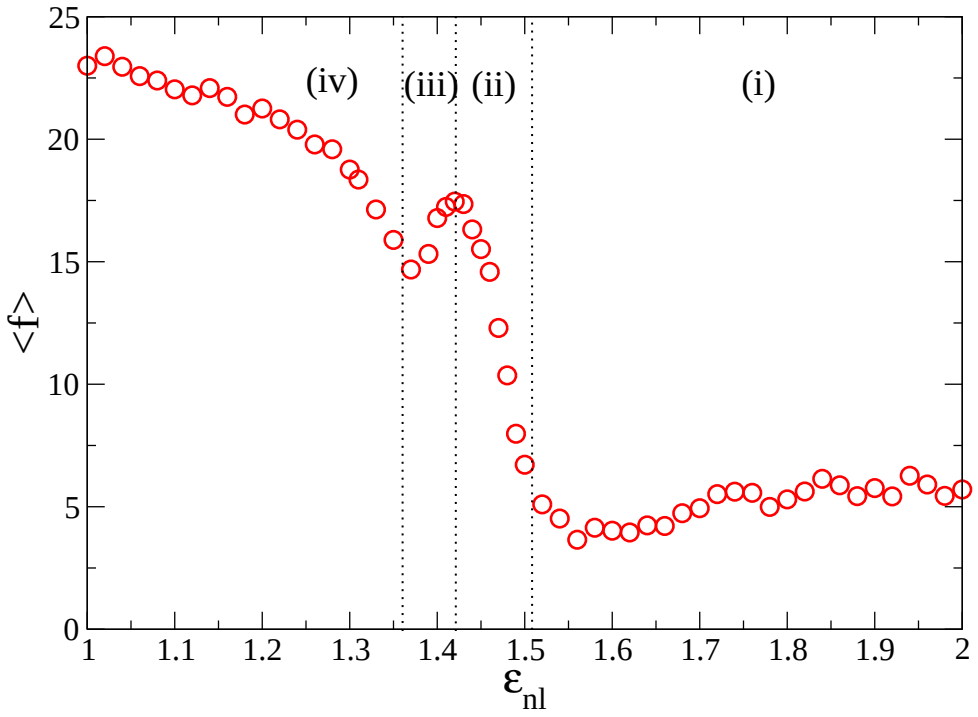

Figure 4.24: Dependence of the mean finger number on the particle-liquid interaction strength ε_{nl}. The regions marked (i) to (iv) are discussed in the main text. The remaining parameters are as in Fig. 4.23 and $\varepsilon_{nn} = 2.0$.

15 at about $\varepsilon_{nn} = 2.25$. This is mainly a geometric effect resulting from our one-dimensional finger counting routine. It reflects the fact that the fingers break up increasingly and the "dried in" nanoparticle pattern starts to look more and more isotropic. Demixing of particles and liquid occurs already in the the bulk liquid behind the front.

(iv) Beyond $\varepsilon_{nn} = 2.15$ fluid and particles demix already in the bulk in a homogeneous manner, the remaining dried-in structure of nanoparticle islands is isotropic, and the emerging demixing length scale decreases with increasing ε_{nn}. The "finger number" is one way to count the islands. Note, however, that it is not an adequate measure to study those isotropic structures (that are not of central interest here). The front resembles a liquid front receding inside a porous medium (formed by the nanoparticle islands).

Our interpretation of the ongoing physical processes is confirmed by Fig. 4.24 showing the dependence of the average number of fingers on the liquid-particle interaction strength ε_{nl} in the range between 1.0 and 2.0 for fixed $\varepsilon_{nn} = 2.0$. A similar sequence of regions (i) to (iv) is found; this time however, with decreasing interaction parameter. This agrees well with the considerations in the start of this section.

4.4 A genetic algorithm approach

If all possible variables are taken into account, the parameter space of our simulations is very large, even with the inclusion of the dynamical chemical potential is still quite large. In order to replicate a specific experimental result, simulations require a slow process of trial and error. A solution to this problem has been developed, [113], and it is briefly described here, how a combination of a Monte Carlo model with a genetic algorithm (GA) can be used to tune the evolution of a simulated self-organising nanoscale system toward a predefined non-equilibrium morphology. The principle is simple, basically, a target structure is provided and a population of morphologies is generated from a random set of parameters. The similarities of each morphology with the target is measured and a second generation of morphology is produced, repeating the process until a desired level of "fitness" is reached. A pseudocode of the algorithm including the details, is shown in Fig. 4.25.

Image morphometry, specifically, Minkowski functional analysis is used as the basis of the fitness function for the genetic algorithm. Evolved simulation parameters produce simulated nanoparticle patterns which closely match the target images taken from experimental data and replicate a number of morphological measures. The results provide an important bridge between simulation and experiment in the study of self-organising nano-structured systems and, moreover, bring us closer to the concept of software control of matter.

A set of four patterns is defined, each demonstrating different morphological families, taken from experimental images (see Fig. 4.26). These four patterns were the targets that the GA needed to reverse engineer by finding a suitable set of parameters for the MC simulator. For any of the given targets, the GA was run for 100 generations using a population of 20 individuals. Each individual comprised a candidate parameter set for the MC simulator. On each target pattern we run the GA ten times. In every case, the simulator was run for 1000 Monte Carlo cycles. Fig. 4.26 shows representative results from the GA runs that are characterised by the striking similarity to their respective targets; the results for the island and labyrinth targets are particularly good and taking into account that both the experimental and simulated patterns arise from a stochastic process (i.e., for a given parameter set two distinct runs will produce similar yet not identical behaviours) the cell and worm patterns are also remarkably close to their experimental objective. Fig. 4.27 shows how the evolution progressed in each case with plots of the fitness function over the generations.

This work has presented evolutionary computation as a method for designing target mor-

```
while (stopping condition not fulfilled)
  parents = select parents from population
  with a defined probability
    'mate' the parents to form (usually) two children
  else
    children = parents
  with a defined probability
    mutate children
  insert children into population
  evaluate and cull population
```

(a) Pseudo-code

Parent selection:	roulette wheel
Crossover operator:	uniform
Probability of crossover:	0.7
Mutation operator:	BCG^{26}
Mutation rate:	0.3
Stopping condition:	after 100 generations
Replacement strategy:	$(\mu+\lambda)$, with $\mu = 16$ and $\lambda = 8$

(b) GA system parameters (where μ represents the population size and λ the number of offspring produced in each generation)

Figure 4.25: Genetic algorithm pseudocode with details.

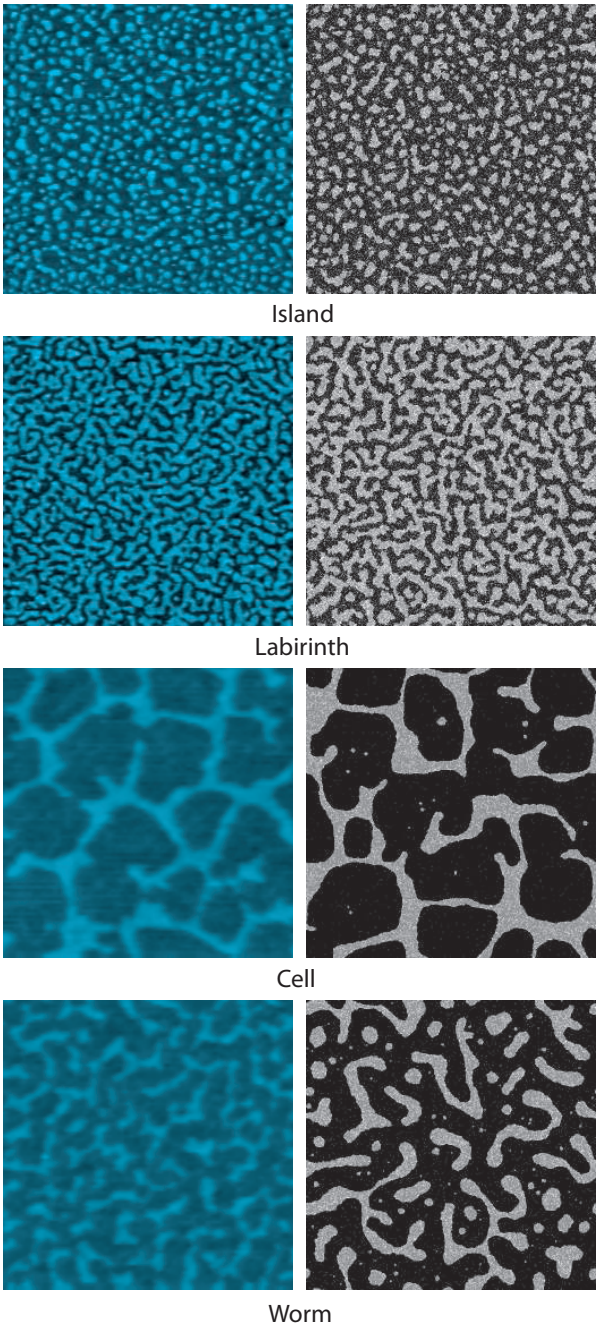

Figure 4.26: Characterisation of the evolved patterns using the Minkowski functional-based fitness function. The left column shows the target, i.e., experimental, images. The right column shows self-organised patterns mimicking the experimental data. These patterns were evolved using the evolutionary algorithm described.

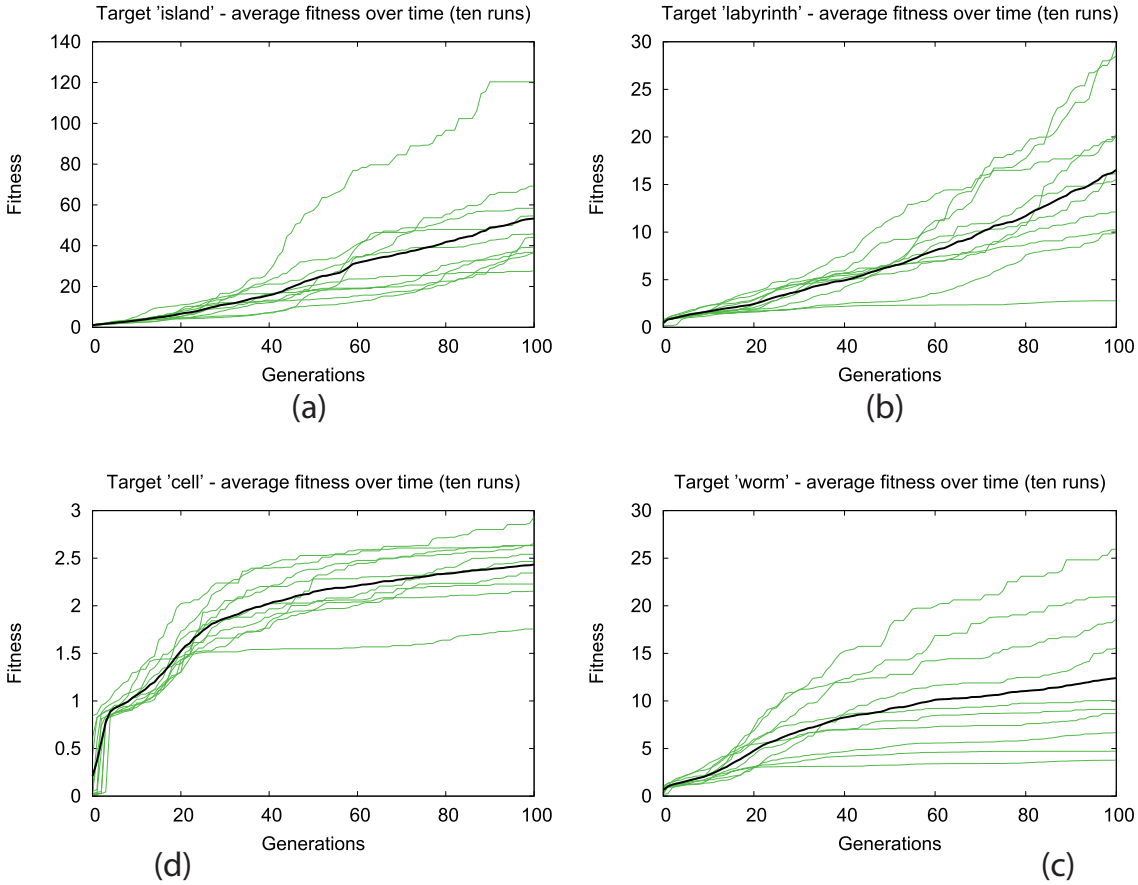

Target	Average fitness	Best fitness	Worst fitness	Fitness deviation
Island	111.9305	460.6708	36.07952	126.0549
Labyrinth	36.51094	84.49821	2.851095	27.09551
Cell	2.742406	3.632334	1.934135	0.427782
Worm	20.88366	50.97714	3.824032	17.15378

Figure 4.27: Population dynamics of the genetic algorithm. Each experimental image is used as a target in ten independent runs of the GA. Panels (a)-(d) show the average population fitness as a function of time ("generations") of each run as well as the average evolution (black line). The table shows, for each experimental target, the average, best and worst fitness parameters.

phologies of self-organising nano-structured systems. Minkowski functionals is used to direct the evolution in search of simulated patterns that closely mimic those observed experimentally. The simulation is also able to produce a number of patterns that are more uncommon in experiments, such as branched structures reminiscent of viscous fingering. The obvious next step is to couple the GA directly to an experiment rather than a simulator.

4.5 Control of 2D pattern formation via surface inhomogeneities

In the present section we describe how it is possible to obtain a highly localised control of 2D pattern formation in colloidal nanoparticle arrays employing surface inhomogeneities that are created by atomic force microscope (AFM)-induced oxidation [70]. In addition to representing a new technique for nanostructure control, the experiments and associated simulations provide key insights into the mechanisms of surface inhomogeneity-directed self-organisation in nanoparticle systems. Whereas nanoscale surface features drive the rupture of the solvent nanoparticle film, microscale oxide features on an otherwise hydrophobic surface retard solvent evaporation, providing important complementary strategies for spatial control of dewetting dynamics. It is shown that a simple modification of the Hamiltonian introduced by Rabani et al. [95] can reproduce important experimentally observed patterns not captured by the original algorithm.

Experiments are based on AFM-induced oxidation of hydrogen-passivated Si(111) surfaces. Oxidation was carried out using PtIr-coated silicon probes at a bias of -10 V and in 70% humidity. Octanethiol-passivated Au nanoparticles of $\approx 2nm$ core diameter ($\pm 8\%$) were prepared in toluene. For experiments involving rapid solvent evaporation, a 25 μl droplet of an appropriately diluted solution (typical concentration values ranged from 0.1 mg/ml to 1 mg/ml) was placed on the locally oxidised substrate and the sample subsequently spun at 4000 rpm. Slow evaporation was induced by keeping the solvent in a meniscus on the sample by means of a small Teflon ring.

The 2D Ising model simulations are capable of replicating a large number of the nanoparticle structures seen in experiment. In particular, certain classes of cellular structures are reproduced with an accuracy that renders them statistically indistinguishable from experiment. There are, however, a number of common experimental phenomena that cannot be simulated by this

method and which are of key importance to our studies of directed dewetting. For example, Fig. 4.4(a) shows a structure that is frequently observed in experiments. A radially averaged 2D Fourier transform, Fig. 4.28, reveals that the pattern exhibits not just one but two preferred cell sizes, each having a relatively wide distribution. A detailed examination of the parameter space has shown that it is not possible to reproduce this structure by means of the simulations described in Chapter 4.

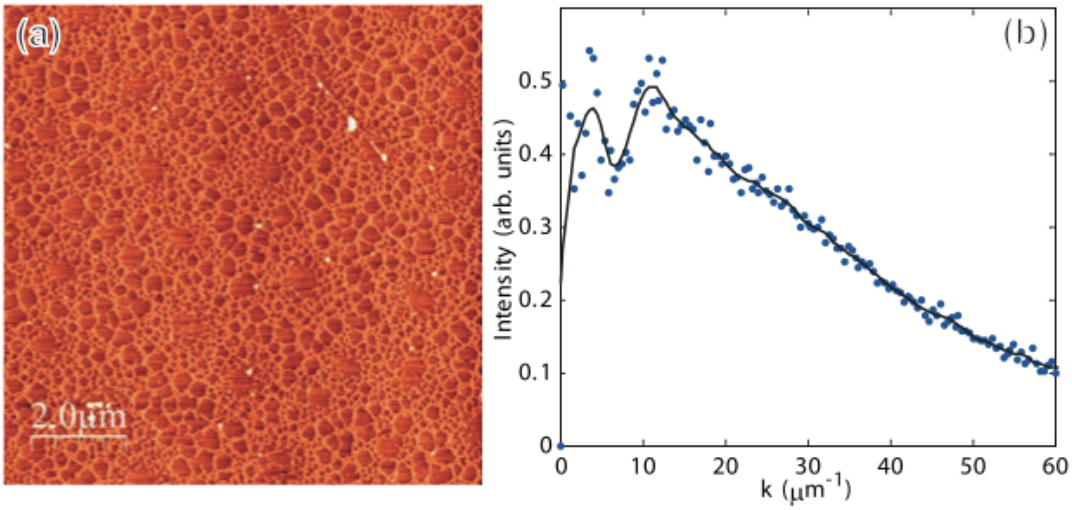

Figure 4.28: (a) An AFM image of a two-level cellular structure formed by spin-casting gold nanoparticles in toluene onto a silicon substrate, (b) a radially-averaged two-dimensional fast Fourier transform of (a), (Courtesy of C. P. Martin).

One can find that a simple change to the Hamiltonian of the original 2D model is sufficient to capture the resulting partial 3D nature. By making the chemical potential an explicit function of the global solvent density, we can model an increase in μ as the solvent layer thins during evaporation. This density dependence corresponds to a thickness dependent disjoining pressure in our pseudo-3D approach, accounting for substrate wettability in continuum models. As a result, the solvent evaporates with a rate inversely proportional to its coverage, Fig. 4.4. Fig. 4.4(b) shows the result of this modification, which matches the experimental image not just qualitatively, but also quantitatively.

Increasing the coupling between μ and solvent coverage, Fig. 4.4(d), replicates the effect of using chloroform in the experiments, Fig. 4.4(c),. Importantly, the nanoparticle rings in these simulated structures are formed spontaneously, without the manual introduction of nucleation sites described by Yosef and Rabani. The behavior of the solvent plays a critical role in

determining the nature of the nanoparticle patterns; to a large extent, the particles are merely passengers on the tide of the solvent, and their final positions describe the history of flow and evaporation. Modifying the surface of the substrate to perturb the behavior of the solvent must therefore lead to a modification of the nanoparticle structures. Fig. 4.33(a) shows the striking effect on nanoparticle organisation of an AFM-oxidized 4x4 μm^2 square on the bare substrate. Typical snapshots from simulations illustrating the result of a simulation with $|\mu|$ lower outside the oxide area are shown in Fig. 4.29 and with $|\mu|$ lower on the oxide area are presented in Fig. 4.30. Dependence on mobility is illustrated in Fig. 4.32. The starting condition for figures is an homogeneous liquid film. There is an extremely sharp transition from a cellular structure on the oxide to a broken wormlike pattern elsewhere. Given that the edge of the oxide region should in principle represent a steep gradient in wettability, with strong implications for dewetting mediated pattern formation, the lack of a region denuded of nanoparticles at the edge of the oxide is intriguing.

Simulations indicate that cellular networks are generated by slower solvent evaporation than that which occurs in the formation of labyrinthine structures. This would suggest that evaporation is somehow retarded by the presence of the oxide; i.e., the solvent finds the oxide areas more wettable. Fig. 4.33(b) shows the result of spatially varying the value of μ, such that $|\mu|$ is very slightly (6%) lower on the oxide than in the surrounding area, with an interface region comprising a $100nm$ linear transition. This equates to a greater wettability in the region of the oxide. The image shown in Fig. 4.33(b) matches the experimental result extremely well.

Fig. 4.34(a) shows nanoparticle patterns formed in the presence of oxide rings of $1\mu m$ diameter. It is possible to reproduce this effect in the simulations by completely removing sections of solvent and nanoparticles from regions representing the oxide rings prior to the start of the simulation. This is similar to the technique employed by Yosef and Rabani, [139]. The importance of dewetting nucleated by a gradient in wettability has been discussed in more details for thin polymer films on heterogeneous substrates, [58, 13]. A simulation including this modification, and also a solvent density-dependent chemical potential, see Fig. 4.4, is shown in Fig. 4.34(b). This process of directed dewetting enables confinement within specific nanoscale surface regions without the need for chemical functionalisation of the nanoparticles. Fig. 4.34(c) shows a similar simulation but instead of rings, linear parallel stripes are considered.

The ability to control pattern formation by locally directing solvent dewetting is an important development on the road to self-organised nanoparticle devices. A lack of requirement for

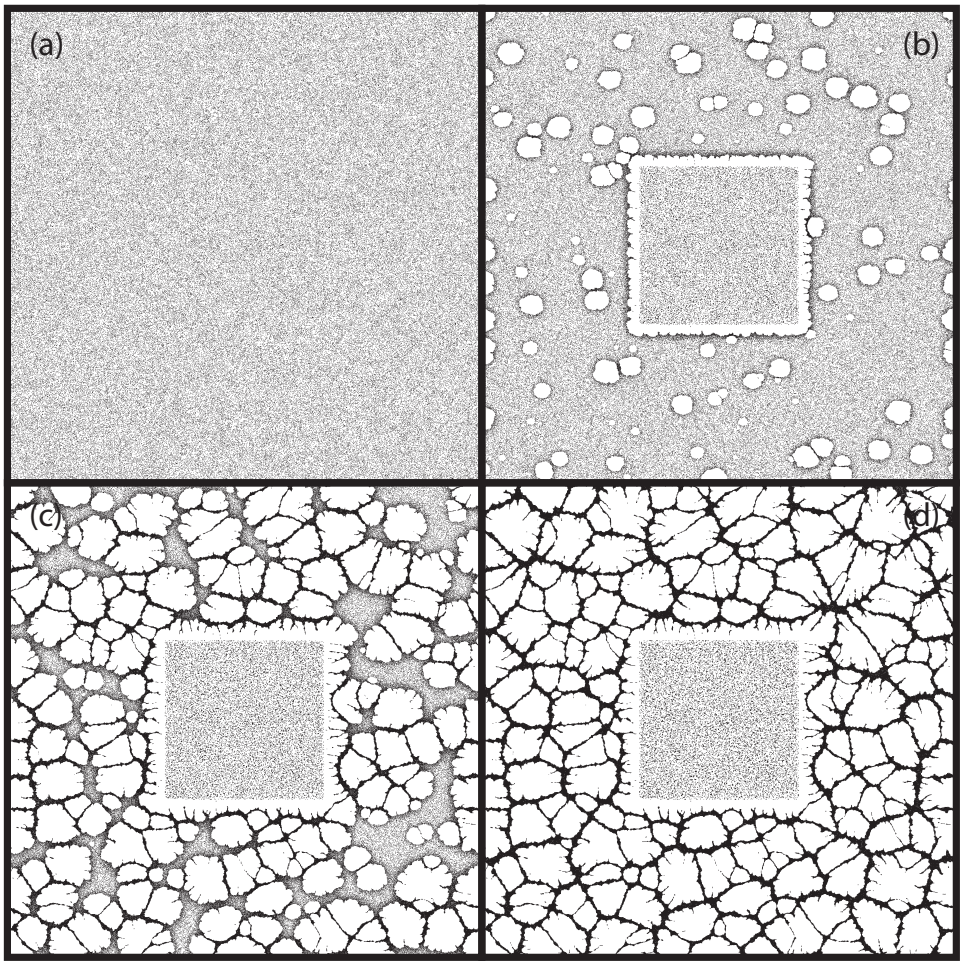

Figure 4.29: Typical snapshots from simulations illustrating the result of a simulation with μ lower outside of oxide area. The starting condition is an homogeneous liquid film. The simulation parameters are: the number of Monte Carlo steps (a) initial starting condition, (b) 96, (c) 240, (d) 496, domain size 3000×3000, $kT = 0.2$, $M = 20$, $\mu = -2.5$. $\phi = 0.2$, $\varepsilon_{nl} = 1.5$, $\varepsilon_{nn} = 2.0$, $\varepsilon_{ll} = 1.0$.

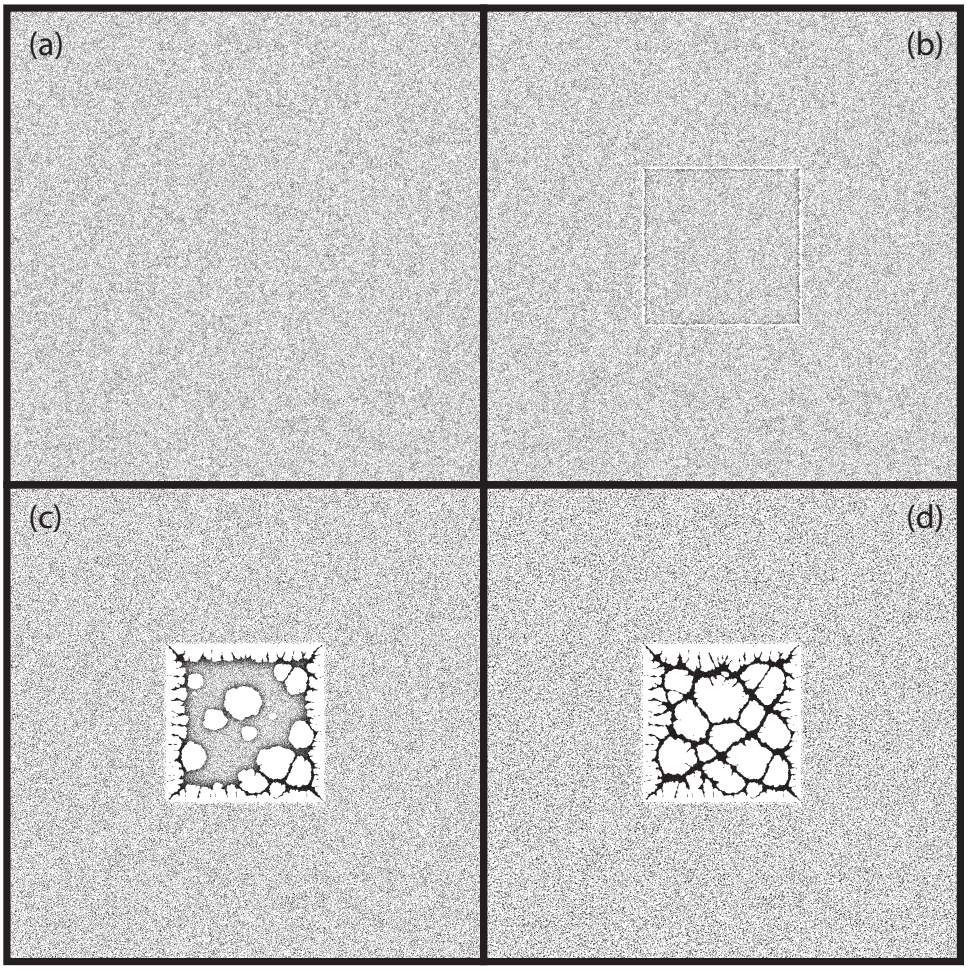

Figure 4.30: Typical snapshots from simulations illustrating the result of a simulation with μ lower on the oxide area. The starting condition is an homogeneous liquid film. The simulation parameters are: the number of Monte Carlo steps (a) initial starting condition, (b) 16, (c) 176, (d) 496, domain size 3000×3000, $kT = 0.2$, $M = 20$, $\mu = -2.5$. $\phi = 0.2$, $\varepsilon_{nl} = 1.5$, $\varepsilon_{nn} = 2.0$, $\varepsilon_{ll} = 1.0$.

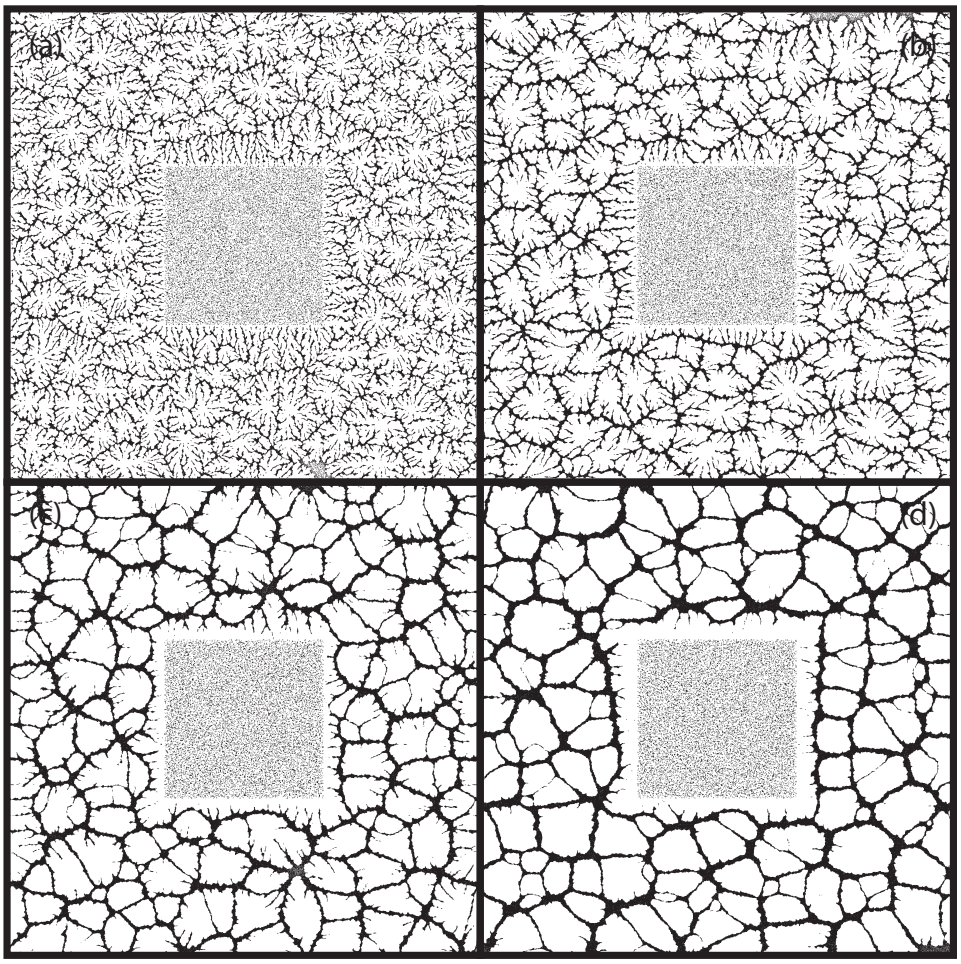

Figure 4.31: Typical snapshots from simulations illustrating the result of a simulation with μ lower outside of the oxide area for different mobility values (a) $M = 5$, (b) $M = 10$, (c) $M = 20$, (d) $M = 30$. The starting condition is an homogeneous liquid film. The other simulation parameters are: the number of Monte Carlo steps 500, domain size 3000×3000, $kT = 0.2$, $M = 20$, $\mu = -2.5$. $\phi = 0.2$, $\varepsilon_{nl} = 1.5$, $\varepsilon_{nn} = 2.0$, $\varepsilon_{ll} = 1.0$.

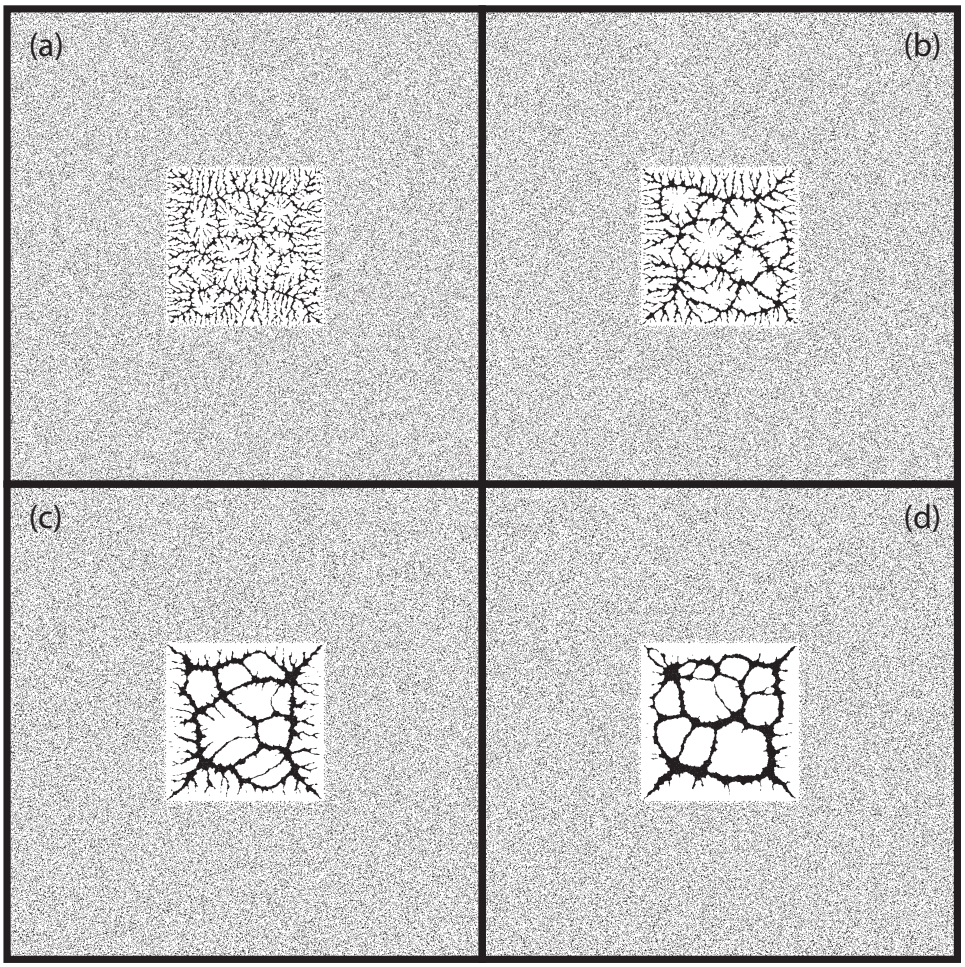

Figure 4.32: Typical snapshots from simulations illustrating the result of a simulation with μ lower on the oxide area for different mobility values (a) $M = 5$, (b) $M = 10$, (c) $M = 20$, (d) $M = 30$. The starting condition is an homogeneous liquid film. The other simulation parameters are: the number of Monte Carlo steps 500, domain size 3000×3000, $kT = 0.2$, $M = 20$, $\mu = -2.5$. $\phi = 0.2$, $\varepsilon_{nl} = 1.5$, $\varepsilon_{nn} = 2.0$, $\varepsilon_{ll} = 1.0$.

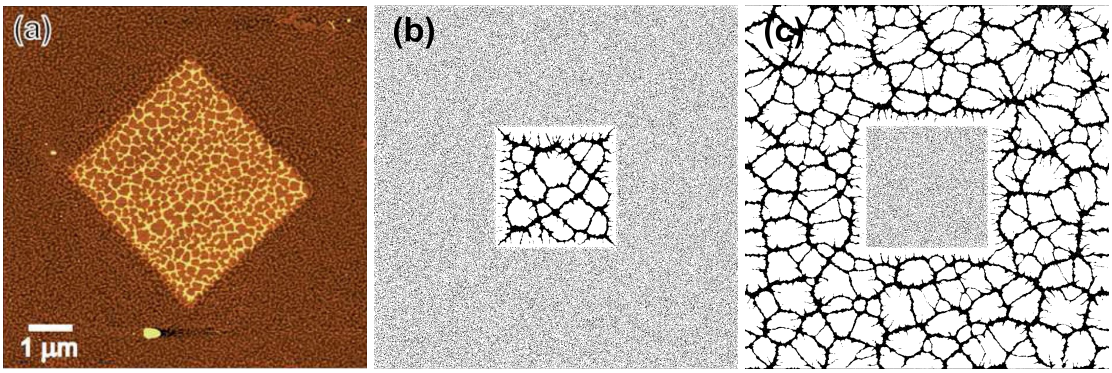

Figure 4.33: (a) An AFM image of gold nanoparticles spun from toluene onto H:Si(111) with an AFM-patterned $4\mu m$ x $4\mu m$ square of oxide in the center, (Courtesy of C.P.Martin), (b) the result of a simulation with μ lower on the oxide area and (c) the result of a simulation with μ lower outside of oxide area. The simulation parameters, for (b) and (c), are: the number of Monte Carlo steps 496, domain size 3000×3000, $kT = 0.2$, $M = 20$, $\mu = -2.5$. $\phi = 0.2$, $\varepsilon_{nl} = 1.5$, $\varepsilon_{nn} = 2.0$, $\varepsilon_{ll} = 1.0$.

Figure 4.34: (a) An AFM image showing the effect of $1\mu m$ diameter rings of oxide on nanoparticle pattern formation. The oxide features in the image are almost entirely free of Au nanoparticles and a denuded zone extends round each ring for a further $100nm$. In the regions between the rings, the Au nanoparticle layer forms a network arising from nucleated dewetting of the solvent. (b) A simulation in which sections of solvent and particles have been removed (indicated in white) to approximate the effect of dewetting from the oxide regions before the realm of the simulation, (Courtesy of C. P. Martin). (c) A similar simulation but instead of rings linear parallel stripes are considered.

particle functionalisation allows this technique to be employed with a wide range of different particle types. The approach described in this section thus opens up a rich new parameter space in directing the assembly of nanoparticle arrays.

Chapter 5

Binary Mixture

After introducing, in the previous chapter, a Kinetic Monte Carlo model used to study a wide diversity of dynamical processes and discussing our results which are in good agreement with the experimental observations, in this chapter we discuss an extension of the single component model towards binary mixtures. The study provides a starting point for further future investigations into the possibility of guiding the self-assembly of a binary mixture by controlled evaporation of the solvent. A schematic representation of the extended model is given in Fig. 5.1.

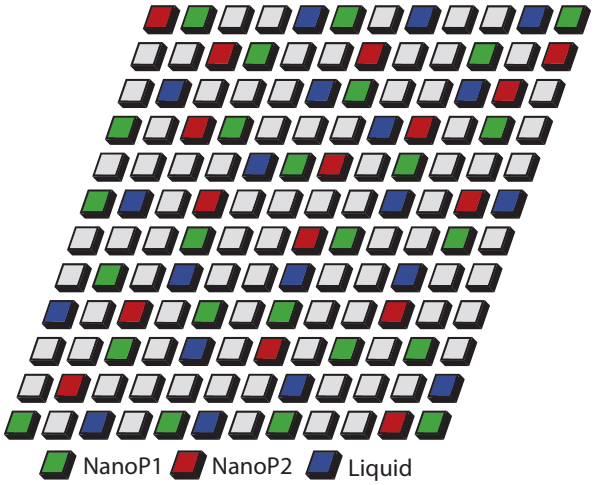

Figure 5.1: Schematic picture of the two-dimensional lattice gas model used: the size of nanoparticle and of a liquid cell is of size 1x1: the liquid is represented as blue squares, nanoparticle type I is shown as green square and the nanoparticle type II is show as red square. The side length of such a cell represents the correlation length of the solvent approximated to be 1 nm.

This type of mesoscopic, or coarse-grained approaches, have the advantage of spanning length scales sufficient for analysing pattern formation within the sample and can also reveal the structures in the material. Using these approaches one can capture, as well, how the system evolves starting from the initial conditions and reaching a final state in a computationally reasonable timescales. For a continuum model to describe the coupled decomposition and profile evolution of a free surface film of a binary mixture see Ref. [126]. The model is based on model-H describing the coupled transport of the mass of one component (convective Cahn-Hilliard equation) and momentum (Navier-Stokes-Korteweg equations) supplemented by appropriate boundary conditions at the solid substrate and the free surface.

The model used to study the self-assembly process of a binary mixture is basically the same as in the previous case for just one type of nanoparticle but there are some modification in the Hamiltonian of the system. Additionally, new terms appear in the Hamiltonian, terms introduced in order to describe the interaction of the second type of nanoparticle with the solvent, the interaction between type II nanoparticles and, as well, the interaction between nanoparticle type I and nanoparticle type II. The Hamiltonian of the system, in this extended case, is given by:

$$\begin{aligned} E = & -\frac{\epsilon_{n1n1}}{2}\sum_{<ij>} n_i n_j - \frac{\epsilon_{n1l}}{2}\sum_{<ij>} n_i l_j - \frac{\epsilon_{ll}}{2}\sum_{<ij>} l_i l_j - \mu\sum_i l_i \\ & - \frac{\epsilon_{n2n2}}{2}\sum_{<ij>} n_i n_j - \frac{\epsilon_{n2l}}{2}\sum_{<ij>} n_i l_j - \frac{\epsilon_{n1n2}}{2}\sum_{<ij>} n_i n_j \end{aligned} \tag{5.1}$$

where $n1$ and $n2$ are the mixture components (nanoparticle type I and nanoparticle type II, respectively), ϵ_{n2n2}, ϵ_{n1n2}, ϵ_{n2l} are the attraction strengths between two adjacent sites that are occupied by type II nanoparticle, nanoparticle type I and nanoparticle type II, or nanoparticle type II and solvent. The other parameters are the same as in the case where the simulations are conducted with just one type of nanoparticles. Also in this case, the equilibrium state of the solvent is defined by μ, the chemical potential, and T, the temperature of the system. The model relies on a Monte Carlo algorithm, where nanoparticles perform a random walk across the lattice. A key assumption that nanoparticles can only move into "wet" sites, is kept here as well. Once adsorbed on the surface, nanoparticles are immobile.

Another difference, here, is that a given mobility is assigned to each type of nanoparticles, so, instead of just one mobility for nanoparticle, in the current case we have two mobilities, one for each type of nanoparticles, M_1 and M_2.

As can be seen in the expression of the Hamiltonian, Eq. (5.1), the number of total parameters for the system is quite big (about twelve parameters), and, there is a need to introduce a new strategy. This simplification should provide a way to be able to explore the full parameter space in order to find, first, a correspondence between the exact parameters values which has been used in the previous chapter, to find similar simulation morphologies, and in the next step to be able to find new simulation structures which should be specific to binary mixture. With regards to this thesis, only the first steps have been undertaken, where an analogy with the previous case is found, and an additional small subset of parameters is explored, but exploring the parameter space in details is left as future work.

The parameter simplification scheme proposed is the following:

- $\epsilon_{ll} = \epsilon_{nn} = \epsilon_{nl} = 1$
- $M_1 = M_2$
- $\epsilon_{n1l} = \epsilon_{n2l}$
- $\epsilon_{n1n1} = \epsilon_{n2n2} = \epsilon_{n1n2}$

Based on this scheme, the problem is reduced to a system which should have a similar behaviour as the system studied in previous chapter.

Using this extended model, a range of structures were produced. A few examples of simulated pattern formation are represented in Fig. 5.2, Fig. 5.3, Fig. 5.4 and Fig. 5.5. Fig. 5.5 shows final structures obtained from simulations, starting with an empty stripe, for different values of $\epsilon_{n1n1} = \epsilon_{n2n2} = \epsilon_{n1n2}$. Fig. 5.5 shows that fingering process is favourable (a)-(b), for small epsilon values, the fingering process competes with demixing process (c)-(d), and demixing process is favourable, there is no fingering anymore (e)-(f).

Fig. 5.6, top, presents results for the average number of fingers when changing $\epsilon_{n1n1} = \epsilon_{n2n2} = \epsilon_{n1n2}$ in the range between 1.5 and 2.1. We distinguish the same regions as in Fig. 4.23. In Fig. 5.6, bottom, we plot the dependence of finger number on the streamwise co-ordinate (y-co-ordinate) to check that the moving dewetting front moves on average with a constant velocity and deposits on average the same amount of material in the same number of fingers which is in agreement with the simulations for unary system described in previous chapter.

Running simulations with the parameter simplification scheme proposed above yields to the same behavior as in the case of one component simulations, as we expected. Now the next step

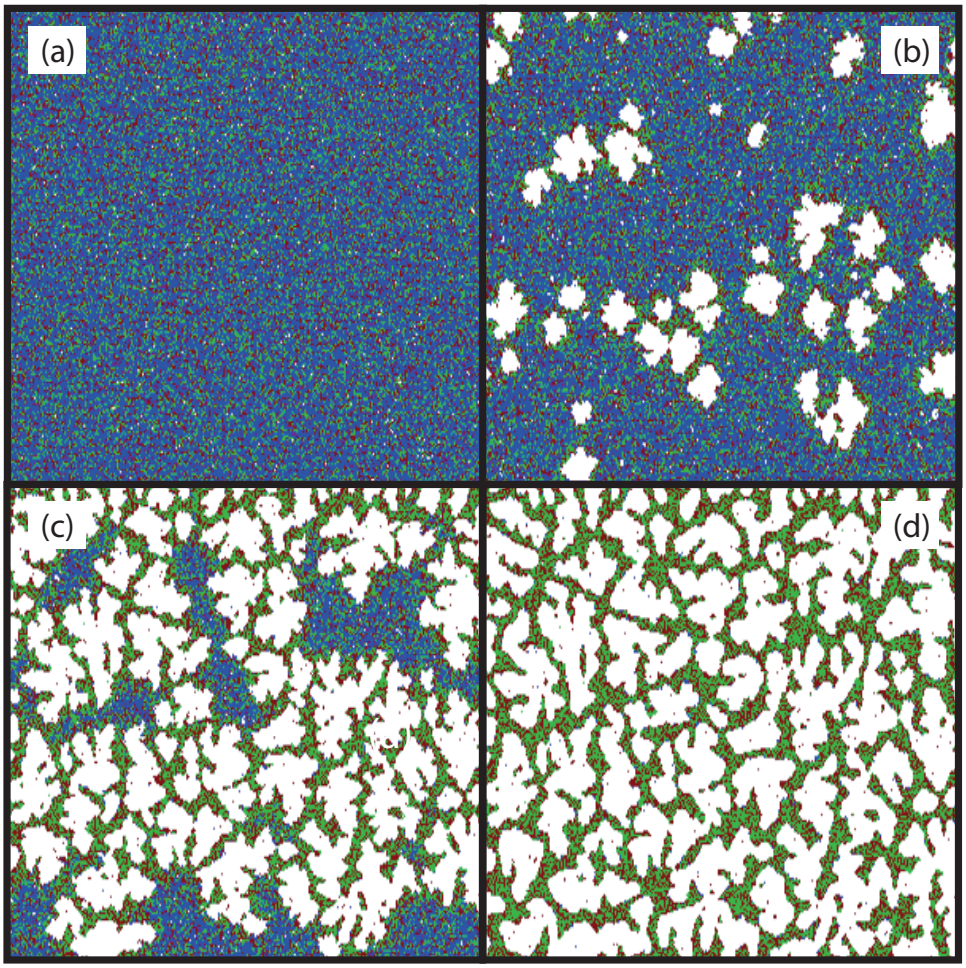

Figure 5.2: Snapshots obtained from simulations: (a) k=0, (b) k=60, (c) k=140, (d) k=600. Lattice size is 300x300 and the other simulation parameters are: $\epsilon_l = 1, \mu = -2.3, kT = 0.3, M = 3, coverage_{n1} = 0.2, coverage_{n2} = 0.2, \epsilon_{n1l} = 0.8, \epsilon_{n2l} = 0.8, \epsilon_{n1n1} = 1, \epsilon_{n2n2} = 1, \epsilon_{n1n2} = 1$.

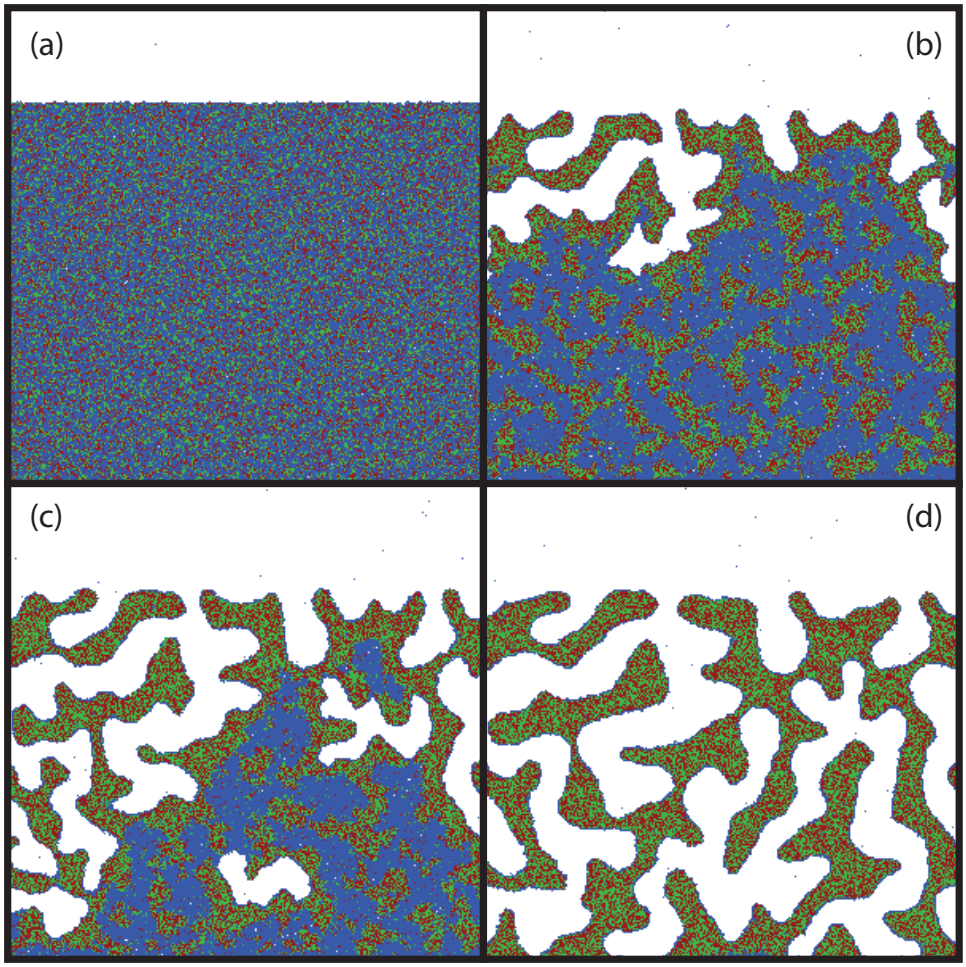

Figure 5.3: Snapshots obtained from simulations, starting with an empty stripe: (a) k=0, (b) k=2700, (c) k=4500, (d) k=9000. Lattice size is 300x300 and the other simulation parameters are: $\epsilon_l = 1, \mu = -2.3, kT = 0.3, M = 3, coverage_{n1} = 0.2, coverage_{n2} = 0.2, \epsilon_{n1l} = 1.5, \epsilon_{n2l} = 1.5, \epsilon_{n1n1} = 2, \epsilon_{n2n2} = 2, \epsilon_{n1n2} = 2$.

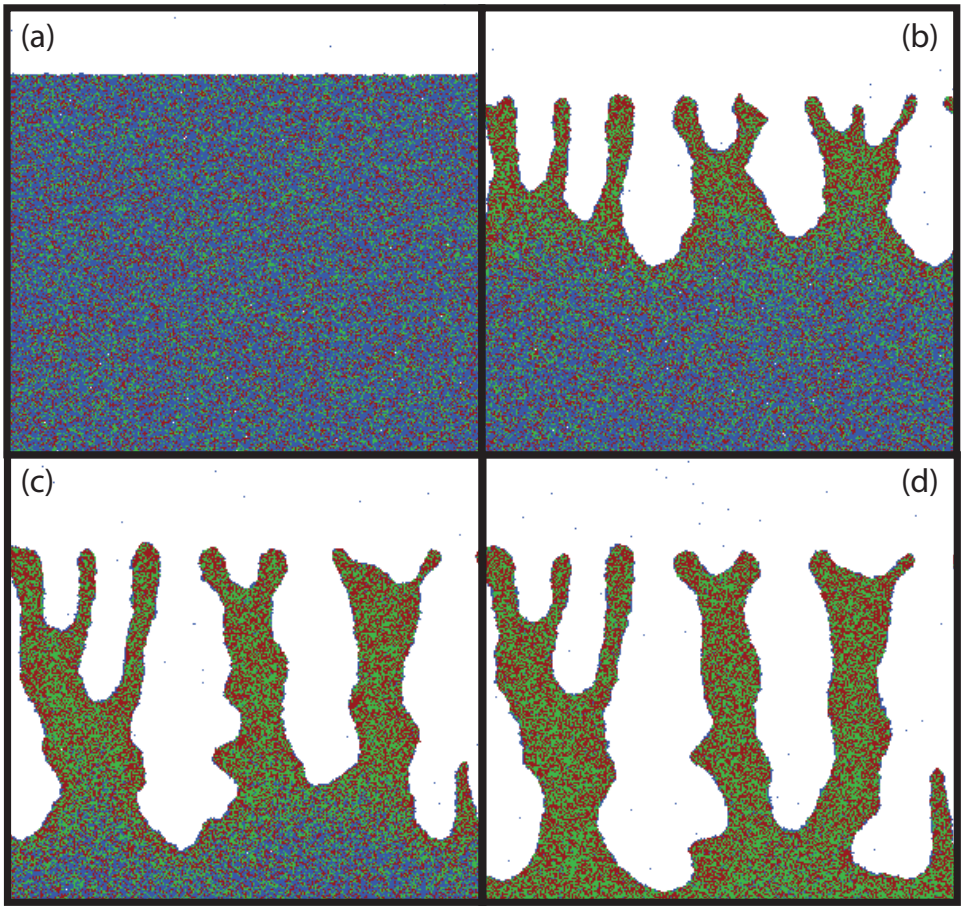

Figure 5.4: Branched fingering structure for evaporative dewetting of a binary mixture: (a) k=0, (b) k=2000, (c) k=4000, (d) k=6000. Lattice size is 300x300 and the other simulation parameters are: $\epsilon_l = 1, \mu = -2.3, kT = 0.3, M = 3, coverage_{n1} = 0.2, coverage_{n2} = 0.2, \epsilon_{n1l} = 1.2, \epsilon_{n2l} = 1.2, \epsilon_{n1n1} = 1.3, \epsilon_{n2n2} = 1.3, \epsilon_{n1n2} = 1.3$.

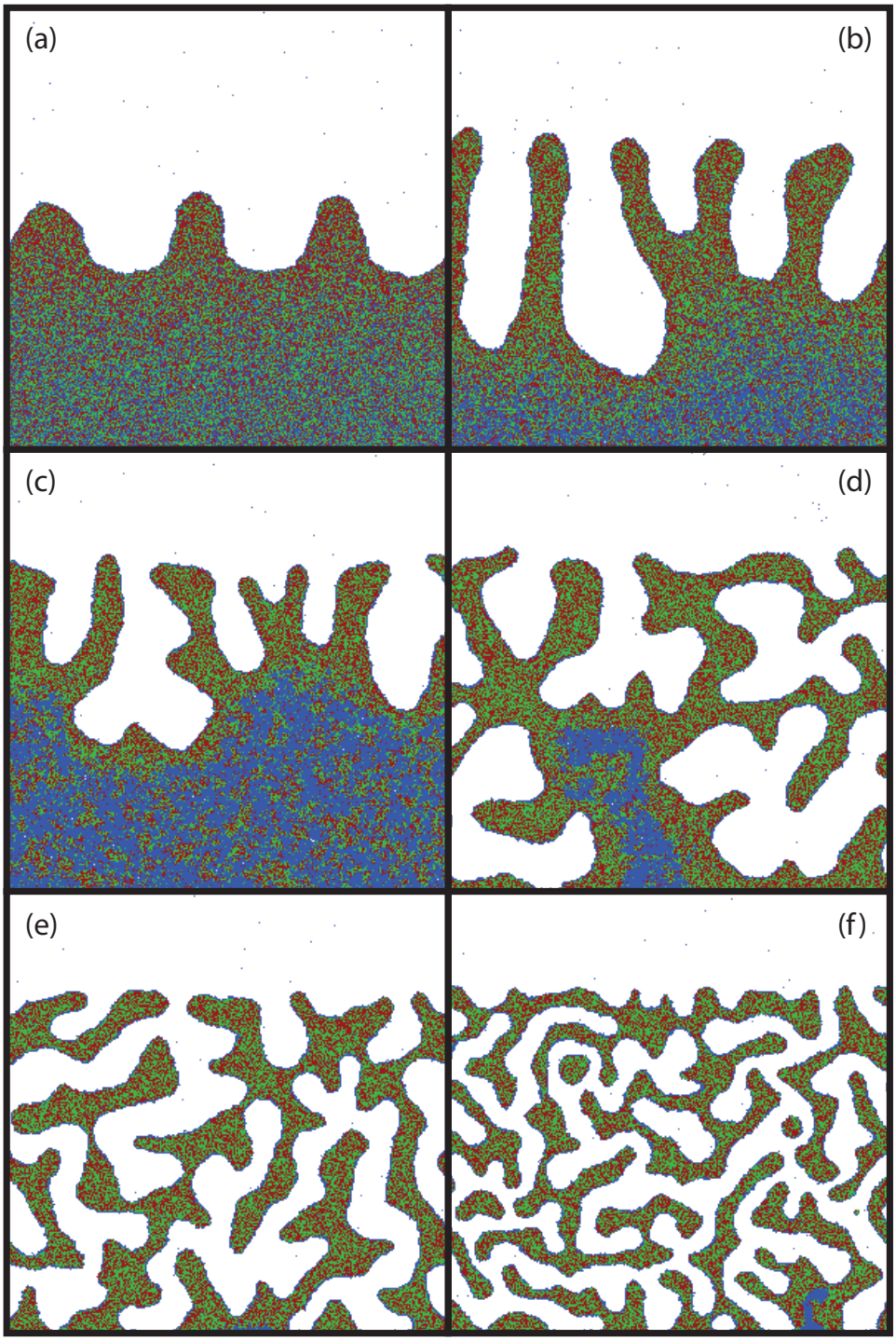

Figure 5.5: Final snapshots obtained from simulations, starting with an empty stripe, for different values of $\epsilon_{n1n1} = \epsilon_{n2n2} = \epsilon_{n1n2}$: (a) 1.5, (b) 1.7, (c) 1.9, (d) 1.95, (e) 2.0, (f) 2.2. The number of Monte Carlo steps is 9000 and the other simulation parameters are: lattice size is 300x300, $\epsilon_l = 1, \mu = -2.3, kT = 0.3, M = 3, coverage_{n1} = 0.2, coverage_{n2} = 0.2, \epsilon_{n1l} = 1.5, \epsilon_{n2l} = 1.5$.

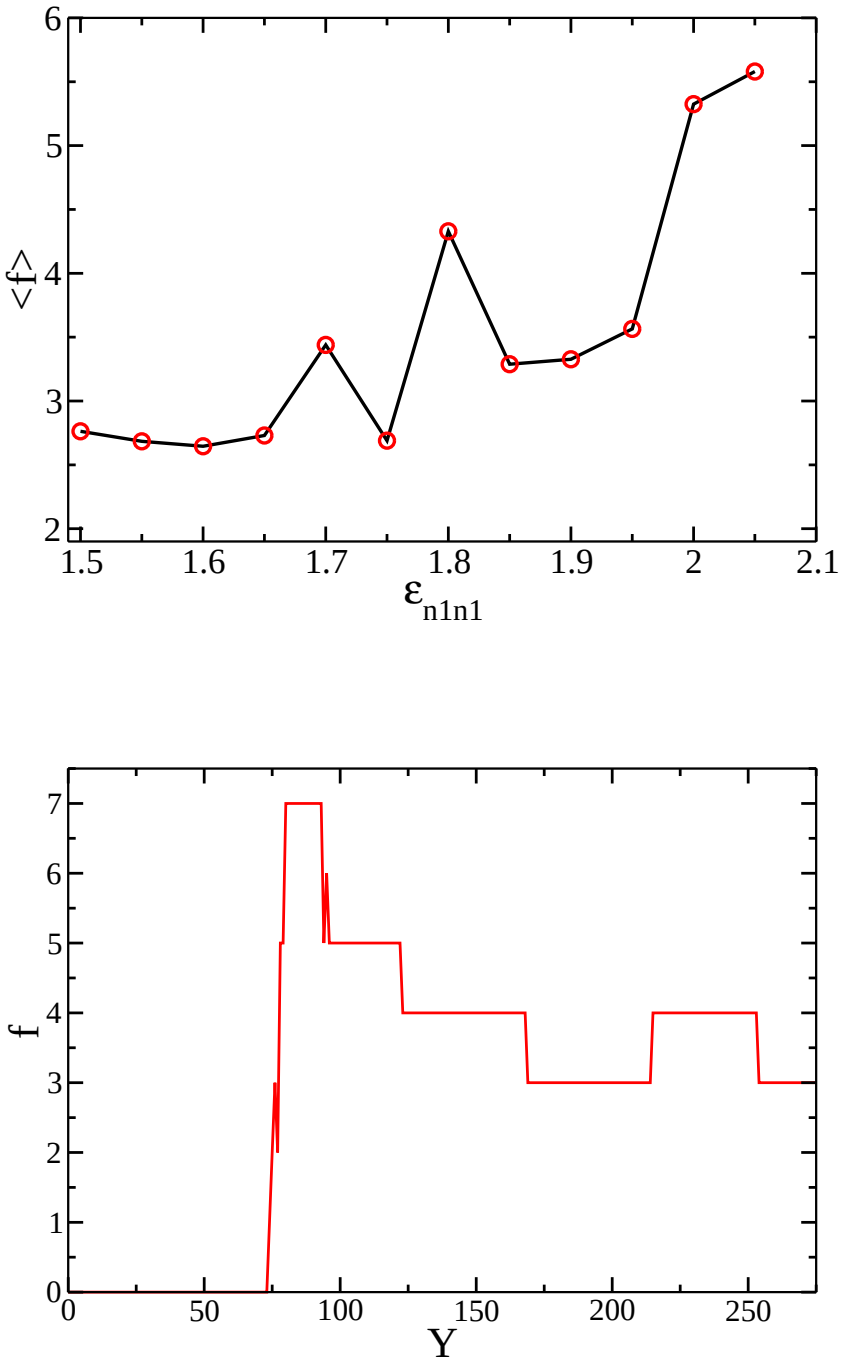

Figure 5.6: Top: Dependence of the mean finger number on the particle-particle interaction strength $\epsilon_{n1n1} = \epsilon_{n2n2} = \epsilon_{n1n2}$, Bottom: dependence of finger number on streamwise coordinate (i.e., y-direction) - the figure may be read as a space-time plot of the fingering at the moving dewetting front.

is to go a bit further to see how the binary system behaves if we modify different parameters, i.e. interaction between nanoparticle type I and nanoparticle type II, or for different values of interaction parameters between nanoparticles and liquid, etc, in this way one can see different fingering patterns which can not be seen with the previous model.

The first range of parameters which we modified are the interaction energy between nanoparticle type I and liquid to be smaller than the interaction energy between nanoparticle type II and liquid. Typical fingering structures from simulations with these changes in parameters are shown in Fig. 5.7. If ϵ_{n1l} is smaller compared with ϵ_{n2l} then can be observed a small coarsening process (a)-(b) but the number of fingers is the same, and if the values for ϵ_{n1l} are increased we can see a decrease in the number of fingers and the coarsening process is not present anymore in bulk, (d)-(g). The front expels first the nanoparticles with the bigger interaction energy which aggregates in small domains which contain that type of nanoparticles. The front lets behind the formed coarsened domains and it continues to develop forming a fingering structure. If the value of ϵ_{n1l} is closer to the value of ϵ_{n2l} there are no clear fingers. Another observation which can be made just looking to the simulation snapshots is that the dewetting front velocity is about two times faster if ϵ_{n1l} is smaller compared with ϵ_{n2l}, i.e. comparing (a) and (h). To have a complete developed fingering pattern the number of monte Carlo should be about two times bigger.

Fig. 5.8 shows the opposite case of Fig. 5.7, the case where ϵ_{n1l} is bigger compared with ϵ_{n2l}, and for this range of parameters values, the fingering process does not occur even if the front fluctuates. The front velocity is constant.

The interaction energies between different type of nanoparticles and between the same type of nanoparticles have a very important role for fingering process as illustrated in Fig. 5.9. If $\epsilon_{n1n1} = \epsilon_{n2n2} = \epsilon_{n1n2} = 1.7$, Fig. 5.9(a), a nice finger structure can be obtained, but if a smaller value is considered, i.e. $\epsilon_{n1n1} = \epsilon_{n2n2} = \epsilon_{n1n2} = 1.3$, Fig. 5.9(b), the fingering process is not present and can be seen a relatively strong front fluctuation.

The second range of parameters which we considered is the case where the interaction between different type of nanoparticles, ϵ_{n1n2}, is bigger or smaller than the interaction between the same type of nanoparticles ($\epsilon_{n1n1} = \epsilon_{n2n2}$). The result from simulations is shown in Fig. 5.10 and Fig. 5.11.

If $\epsilon_{n1n2} < \epsilon_{n1n1} = \epsilon_{n2n2}$ then clustering process occurs, the fingers are broken after a few simulation steps, particles of similar type will form small clusters, Fig. 5.10(a)-(c). If the value

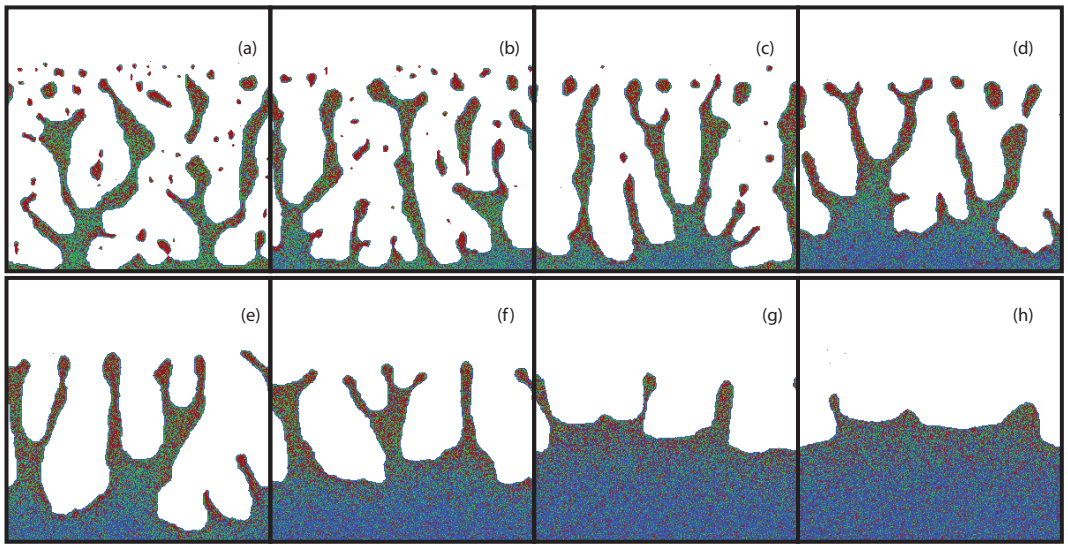

Figure 5.7: Fingering structures for evaporative dewetting front of a binary mixture for $\epsilon_{n1l} < \epsilon_{n2l}$. $\epsilon_{n2l} = 1.9$ and ϵ_{n1l} values are: (a) 1.1, (b) 1.2, (c) 1.3, (d) 1.4, (e) 1.5, (f) 1.6, (g) 1.7, (h) 1.8. Lattice size is 300x300 and the other simulation parameters are: Monte Carlo steps 5000, $\epsilon_l = 1, \mu = -2.3, kT = 0.2, M = 2, coverage_{n1} = 0.1, coverage_{n2} = 0.1, \epsilon_{n1n1} = 1.7, \epsilon_{n2n2} = 1.7, \epsilon_{n1n2} = 1.7$.

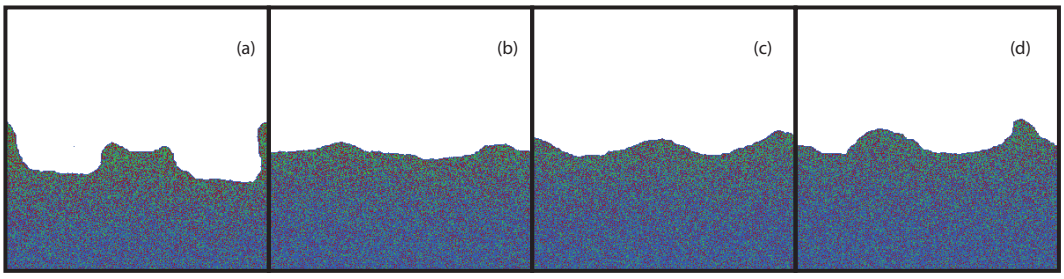

Figure 5.8: Fingering structures for evaporative dewetting front of a binary mixture for $\epsilon_{n1l} > \epsilon_{n2l}$. $\epsilon_{n2l} = 1.5$ and ϵ_{n1l} values are: (a) 1.7, (b) 1.8, (c) 1.9, (d) 2.0. Lattice size is 300x300 and the other simulation parameters are: Monte Carlo steps 5000, $\epsilon_l = 1, \mu = -2.3, kT = 0.2, M = 2, coverage_{n1} = 0.1, coverage_{n2} = 0.1, \epsilon_{n1n1} = 1.3, \epsilon_{n2n2} = 1.3, \epsilon_{n1n2} = 1.3$.

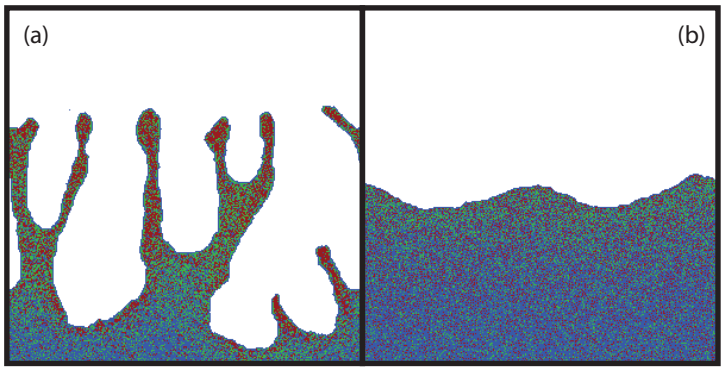

Figure 5.9: Fingering structures for evaporative dewetting front of a binary mixture for different $\epsilon_{n1n1} = \epsilon_{n2n2} = \epsilon_{n1n2}$ (a) 1.7, (b) 1.3. Lattice size is 300x300 and the other simulation parameters are: Monte Carlo steps 5000, $\epsilon_l = 1, \mu = -2.3, kT = 0.2, M = 2, coverage_{n1} = 0.1, coverage_{n2} = 0.1, \epsilon_{n1l} = 1.5, \epsilon_{n2l} = 1.9$.

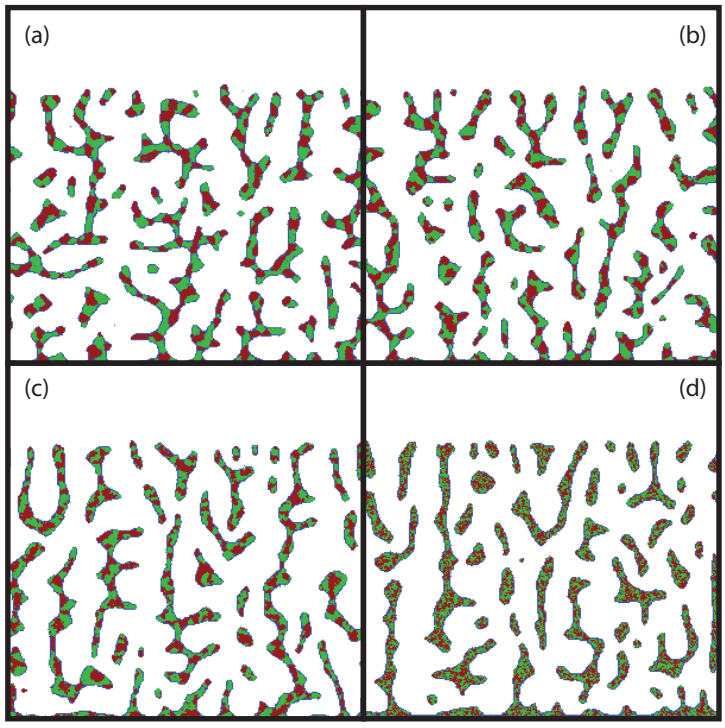

Figure 5.10: Fingering structures for evaporative dewetting front of a binary mixture for $\epsilon_{n1n2} < \epsilon_{n1n1} = \epsilon_{n2n2} = 1.7$. ϵ_{n1n2} values are: (a) 1.1, (b) 1.3, (c) 1.4, (d) 1.6. Lattice size is 300x300 and the other simulation parameters are: Monte Carlo steps 5000, $\epsilon_l = 1, \mu = -2.3, kT = 0.2, M = 2, coverage_{n1} = 0.1, coverage_{n2} = 0.1$.

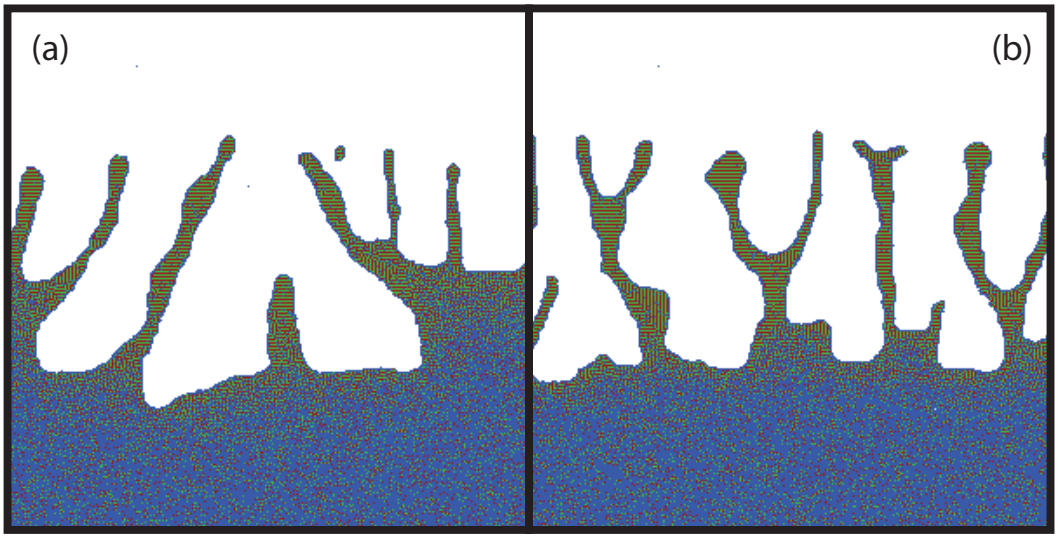

Figure 5.11: Fingering structures for evaporative dewetting front of a binary mixture for $\epsilon_{n1n2} >> \epsilon_{n1n1} = \epsilon_{n2n2} = 1.3$. ϵ_{n1n2} values are: (a) 2.1, (b) 2.2. Lattice size is 300x300 and the other simulation parameters are: Monte Carlo steps 5000, $\epsilon_l = 1, \mu = -2.3, kT = 0.2, M = 2, coverage_{n1} = 0.1, coverage_{n2} = 0.1$.

of ϵ_{n1n2} is closer to the value of ϵ_{n1n1} and ϵ_{n2n2} then these nanoparticle clusters will not be visible anymore, but the fingers are still broken.

In the other case, where $\epsilon_{n1n2} >> \epsilon_{n1n1} = \epsilon_{n2n2}$, illustrated in Fig. 5.11, one can observe that the fingering process occurs, being more favorable than clustering, but nanoparticles of the same type organise in horizontal stripes.

Simulation of a binary mixture is an out-of-equilibrium problem where we should take into account the dynamic treatment of different coupled phase transitions, three in our case: drying process (the evaporation of the solvent), coarsening effect (formation of specific domains), and a type of ordering within the domains, formation of superlattices.

Considering the case when all interactions between the nanoparticles are equal, one can see that, the resulting structural morphologies are well described by using just a simplified single-component model. However, if we consider the other cases, presented in this chapter, where the interactions are larger/smaller then the interactions between nanoparticles of identical type, it is observed that coarsening process of the nanoparticle domains plays an important role and it seems that it is strongly coupled with the fingering process, Fig. 5.10 and Fig. 5.7.

In a binary mixture (a system with two components), the equilibrium morphology is determined by the interaction between the two types of nanoparticles considered. The coarsening

process of nanoparticles depends on the value of ϵ_{n1n2}. If $\epsilon_{n1n2} < \epsilon_{n1n1} = \epsilon_{n2n2}$, the system has a tendency to separate into different type of random shape domains which are rich in nanoparticles type I, and domains which are rich in nanoparticles type II, Fig. 5.10. Looking further to Fig. 5.10, one can observe that the coarsening domains are not present anymore (phase separation process does not appear) if the interaction between nanoparticles type I and nanoparticles type II is 1.6, Fig. 5.10(d). In the opposite case, where $\epsilon_{n1n2} > \epsilon_{n1n1} = \epsilon_{n2n2}$, even if the coarsening process is still observed the movement of the evaporative dewetting front also triggers a separation of the nanoparticles inside the fingers into very regular, horizontal or vertical stripes, Fig. 5.11. This can be seen as a micro-phase separation on the length scale of the computational grid.

The simulations presented in this section are meant to show how a simple extension of our Kinetic Monte Carlo model can be applied in order to simulate the behavior of a binary mixture. We discussed the simplest case of the extended model where similar patterns can be obtained as in the one type nanoparticle model, but also a few different sets of parameters are explored. Of course that there are many parameters which can be varied, and an in depth exploration of the complete parameter space should be done in the future and a quantitative analysis, as well.

Having these simulation results for a system of binary mixture, even if they really look promising, in the absence of experimental results, one can not say if the results will really be in agreement with the experimental work.

Chapter 6

Summary and Outlook

The present work has focused on pattern formation observed in various experimental settings involving dewetting and drying nano-fluids on solid substrates. In addition to polygonal networks and spinodal-like structures, branched structures have been reported in the experiments.

First, we have presented different dewetting experiments and have also frequently employed experimental spin coating method and meniscus technique. The necessary theoretical approaches have also been introduced and a short introduction has been given into thin film theory for pure liquids and the Cahn-Hilliard description of the decomposition of a mixture.

We have employed a kinetic Monte Carlo model to study pattern formation driven by the interplay of evaporating solvent and diffusing nanoparticles. A justification of the usage of a model that only includes dewetting by evaporation but not by convective motion of the solvent has been given based on experimental observations and scaling considerations derived from a mesoscopic continuum model. The model has first been used to analyse the influence of the nanoparticles on the basic dewetting behavior, i.e., on spinodal dewetting, but also on dewetting by nucleation and growth of holes. While it is true that the nanoparticles help to image the basic dewetting patterns (such as the labyrinthine structure resulting from spinodal evaporative dewetting or the random polygonal network resulting from nucleation and growth), they *shift* the bimodal and spinodal line in the chemical potential by a small amount that can be estimated using a mean field argument. In consequence, they influence the nucleation rate. Although in the present work we have not focused on this aspect, it should be further scrutinised in the future. More importantly, the nanoparticles strongly destabilise straight or circular dewetting fronts in the nucleation regime.

We have checked that the results obtained are generic in the sense that small changes in the

model set-up do not change the behavior qualitatively. In particular, we used an independently written code for 1×1 nanoparticles to ensure that the nanoparticle size is not a crucial element. The present work assumed 3×3 nanoparticles to allow for simple comparison with already published results [95, 69, 70].

A crucial rule used in the algorithm is the contrast in the mobility of the nanoparticles, i.e., the assumption that they do not diffuse onto the dry substrate. If one lifts this rule and tries to bound the nanoparticles stronger into the liquid by increasing the particle-liquid interaction strength, i.e., one strongly increases the energetic bias of the particles towards the retracting liquid, no front instability has been found. This explains why Ising-type models for grain growth that include mobile diffusing impurities, to our knowledge have never reported instabilities of domain boundaries caused by the diffusing impurities [115, 134, 43]. In all these models the impurities diffuse equally well in the two phases. They might, however, be energetically biased towards one of the phases or towards the phase boundary. Our present results on evaporating nanoparticle solutions suggest that unstable domain boundaries might also be found in the ordering dynamics of a ferromagnetic system with diffusing impurities under the influence of an external field if the mobility of the impurities strongly depends on the phase.

Further, we have described briefly how the combination of a Monte Carlo model with a Genetic Algorithm (GA) can be developed and used to tune the evolution of a simulated self-organising nanoscale system toward a predefined non-equilibrium morphology. We have shown that evolutionary computation can be employed as a method for designing target morphologies of self-organising nano-structured systems.

As the last main section, highly localised control of 2D pattern formation in colloidal nanoparticle arrays via surface inhomogeneities created by atomic force microscope (AFM) induced oxidation has been presented and some simulations have been shown.

The final section has shown how the simplest one-component model can be extended further, by including a second type of nanoparticles, transforming it in a two-component system. It is observed that the coarsening process competes with the fingering process, and in some cases, for specific values of interaction parameters, the coarsening domains are not visible anymore. If the value of interaction parameter between nanoparticles type I and nanoparticles type II is larger than the value of the interaction parameter between nanoparticles of the same type, one may obtain rather regular, horizontal or vertical stripe patterns that resemble a micro-phase separation process within the fingers. Even if only a few results of some test cases have been

shown, the entire parameter space being considerable larger, the results looks promising and there are open avenues for future research.

We conclude that Kinetic Monte Carlo simulations have allowed us the study of the processes that lead to the production of particular nanoparticle morphologies. Future experiments that study fingering using imposed straight dewetting fronts would be of high interest.

Appendix A

Derivation of Thin Film Evolution Equation

The following steps are necessary for derivation of the film thickness evolution equation in long wave approximation: the transport equation for the momentum density (Navier-Stokes) and continuity equations are written together with appropriate boundary conditions. In order to obtain dimensionless equations we should apply scaling. A non-dimensional parameter $\epsilon = h/L$ is introduced for long wave scaling, where h and L are the vertical and horizontal length scales as illustrated in Fig. 6.1. The continuity equation is used, finally, to get the film thickness evolution equation.

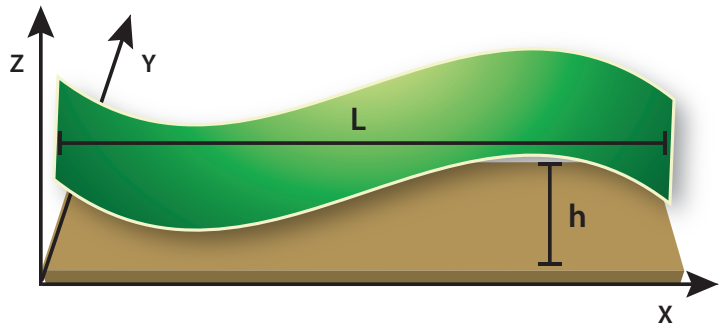

Figure 6.1: A simple representation of thin film length scales.

Basic equations and boundary conditions

The starting point for the derivation of the thin film equation is to write down the transport equation for the momentum density (Navier-Stokes equation):

$$\rho\frac{d\vec{v}}{dt} = \nabla.\bar{\tau} + \vec{f}, \tag{6.1}$$

where $\vec{v} = \begin{pmatrix} u \\ w \end{pmatrix}$ is the velocity field, $\vec{f} = \begin{pmatrix} f_1 \\ f_2 \end{pmatrix}$ is the body force field and $\nabla = \begin{pmatrix} \partial_x \\ \partial_z \end{pmatrix}$.
The stress tensor has the form:

$$\bar{\tau} = -p\bar{I} + \eta(\nabla\vec{v} + (\nabla\vec{v})^T), \tag{6.2}$$

where $p(x, z)$ denotes the pressure field and $\bar{I}$ is the identity tensor. The parameters ρ and η are the density and the dynamic viscosity of the fluid.

Boundary conditions are set at the solid substrate and at the free surface. The appropriate boundary conditions for the continuous film considered here are as follows [124].

At the substrate, ($z = 0$), the no-slip and no-penetration condition is considered:

$$\vec{v} = 0. \tag{6.3}$$

This condition implies that at the solid boundary the fluid will have zero velocity relative to the boundary and the solid substrate is impermeable to the fluid - it “sticks” to the surface.

At the free surface, ($z = h(t, x)$), the kinematic boundary condition is considered:

$$w = \partial_t h + u\partial_x h \tag{6.4}$$

and the condition for force equilibrium:

$$\bar{\tau} \cdot \vec{n} = \vec{n}K\gamma + \vec{t}\partial_s\gamma, \tag{6.5}$$

where $\partial_s = \vec{t} \cdot \nabla$, $p_L = -K\gamma$ is the Laplace or curvature pressure and $\partial_s\gamma$ is the variation of the surface tension along the surface. The normal and tangent vector of the surface are

$$\begin{aligned} \vec{n} &= \frac{1}{\sqrt{1 + (\partial_x h)^2}}(-\partial_x h, 1), \\ \vec{t} &= \frac{1}{\sqrt{1 + (\partial_x h)^2}}(1, \partial_x h). \end{aligned}$$

The curvature of the surface is

$$K = \frac{\partial_{xx} h}{(1 + (\partial_x h)^2)^{3/2}}.$$

Now one can write the vectorial boundary condition (6.5) as two scalar conditions, by simply projecting it onto $\vec{n}$ and $\vec{t}$, respectively:

$$\vec{t} \; : \; (u_z + w_x)(1 - h_x^2) + 2(w_z - u_x)h_x = \partial_s \gamma (1 + h_x^2)/\eta; \tag{6.6}$$

$$\vec{n} \; : \; p + \frac{2\eta}{1 + h_x^2}[-u_x h_x^2 - w_z + h_x(u_z + w_x)] = -\frac{\gamma h_{xx}}{(1 + h_x^2)^{3/2}}. \tag{6.7}$$

Dimensionless groups (numbers)

In the following table a general set of scaling parameters is given [124]:

Dimensionless	t'	x'	z'	p'	$\vec{v}$
Scale	$t_0 = \frac{l}{U_0}$	l	l	$P_0 = \rho U_0^2$	U_0
Dimensional	$t = t_0 t'$	$x = lx'$	$z = lz'$	$p = P_0 p$'	$\vec{v} = U_0 \vec{v'}$

Referring to the momentum transport equations (6.1), the following expression for its x component can be given:

$$\rho \frac{U_0^2}{l}(u'_t + u'u'_x + w'u'_{z'}) = -\frac{\rho U_0^2}{l} p'_{x'} + \eta \frac{U_0}{l^2}(u'_{x'x'} + u'_{z'z'}) + \rho g \sin\alpha, \tag{6.8}$$

where $\vec{f} = \rho\vec{g} = \rho g(\sin\alpha, \cos\alpha)$ is assumed for a film on an inclined surface with inclination angle α.

One can introduce the dimensionless numbers of Reynolds and Froude:

$$Re = \frac{U_0 l \rho}{\eta}, \qquad Fr = \frac{U_0^2}{lg}. \tag{6.9}$$

Using the just introduced non-dimensional numbers, the two components of equation (6.1) become:

$$\begin{aligned} u_t + uu_x + wu_z &= -p_x + \frac{1}{Re}(u_{xx} + u_{zz}) + \frac{\sin\alpha}{Fr}; \\ w_t + ww_x + ww_z &= -p_z + \frac{1}{Re}(w_{xx} + w_{zz}) - \frac{\cos\alpha}{Fr}, \end{aligned} \tag{6.10}$$

where the dashes are dropped for simplicity.
In this case the Reynolds numbers stands for the ratio of the selected velocity scale and the viscous one, and the Froude number corresponds to the squared ratio of the selected velocity scale and the gravitational one.

This scaling is general unless the used scales l and U_0 are specified. All scales in the table above correspond to the same length l and velocity U_0. However, this is not compulsory. For example, a set of appropriate scales for the case of thin film flowing on an inclined substrate exist, any of which leads to different expressions for the dimensionless numbers. Thus, different limits of the model can be estimated with the different scalings [124]. We will use the so called "viscous" scaling based on the viscous velocity scale:

$$U_0 = \frac{\eta}{\rho l}. \tag{6.11}$$

It implies

$$\frac{1}{Re} \to 1, \qquad G := \frac{1}{Fr} \to \frac{gl^3\rho^2}{\eta^2}, \tag{6.12}$$

where G is the Galilei number.

The introduced scaling brings us to the following form of the momentum equations:

$$u_t + uu_x + wu_z = -p_x + u_{xx} + u_{zz} + G\sin\alpha,$$

$$w_t + uw_x + ww_z = -p_z + w_{xx} + w_{zz} - G\cos\alpha. \tag{6.13}$$

The non-dimensional tangential and normal boundary conditions (6.6) and (6.7) become:

$$(u_z + w_x)(1 - h_x^2) + 2(w_z - u_x)h_x = -\frac{l\gamma\Delta T}{U_0\eta l}(T_x + h_x T_z)(1 + h_x^2)^{1/2}; \tag{6.14}$$

$$p + \frac{2}{1 + h_x^2}[-u_x h_x^2 - w_z + h_x(u_z + w_x)] = -\frac{1}{Ca}\frac{h_{xx}}{(1 + h_x^2)^{3/2}} - \Pi, \tag{6.15}$$

where $Ca = \frac{\eta^2}{\gamma_0 l\rho}$ is the capillary number [88].

Π is the so-called "disjoining pressure" which may play an important role for the behavior of ultrathin films (see chapter 3 for more details about disjoining pressure). It is normally included as an additional pressure term $\Pi = -\frac{dF}{dh}$, where $F(h)$ is an additional energy dependent on the film thickness. The disjoining pressure can be introduced in the normal force boundary

condition as an addition to the curvature pressure, or as an additional body force in the Navier-Stokes equation [22]. It can be calculated for specific intermolecular interactions. If a long-range apolar van der Waals interaction is considered, the disjoining pressure has the form

$$\Pi(h) = \frac{A}{6\pi h^3}, \tag{6.16}$$

where A is the Hamaker constant giving the strength of the interaction, which can be calculated from the optical indices of the involved materials [52].

Long-wave scaling

The next step is crucial for the derivation of a simplification of the Navier-Stokes equation for the thin film geometry.

This procedure is based on asymptotic reduction of the full set of governing equations and boundary conditions and brings us to a simplified nonlinear evolution equation. The model obtained may not have the mathematical complexity of the original free-boundary problem, but it still preserves many of the important physical features of the described system [124].

In the case of thin film geometry all length scales parallel to the substrate L (e.g. periods of surface waves or drop length), are large if compared to the film thickness l. This observation prompts us to introduce the smallness parameter ϵ, defined as follows:

$$\epsilon = \frac{l}{L}, \qquad l \ll L.$$

Now, the scale l can be replaced by two separate scales for the two coordinates x and z:

$$x = Lx' = \frac{l}{\epsilon}x', \qquad z = lz'. \tag{6.17}$$

Because of continuity, the velocity components also scale differently:

$$u = U_0 u', \qquad w = \epsilon U_0 w'. \tag{6.18}$$

The time is scaled as

$$t_0^{new} = \frac{U_0}{L} = \frac{\epsilon U_0}{l} = \epsilon t_0. \tag{6.19}$$

The rescaled non-dimensional momentum equations have the form ($u_x, u_t, u_z, w_x, w_z, w_t$ are derivatives)

$$\begin{aligned} \epsilon(u_t + uu_x + wu_z) &= -\epsilon p_x + \epsilon^2 u_{xx} + u_{zz} + G\sin\alpha; \\ \epsilon^2(w_t + uw_x + ww_z) &= -p_z + \epsilon^3 w_{xx} + \epsilon w_{zz} - G\cos\alpha; \end{aligned} \tag{6.20}$$

$$u_x + w_z = 0.$$

The boundary conditions become

$$\begin{gathered}(u_z + \epsilon^2 w_x)(1 - \epsilon^2 h_x^2) + 2\epsilon^2(w_z - u_x)h_x = 0; \\ p + \frac{2}{1+\epsilon^2 h_x^2}[-\epsilon^3 u_x h_x^2 - \epsilon w_z + \epsilon h_x(u_z + \epsilon^2 w_x)] = -\frac{1}{Ca}\frac{\epsilon^2 h_{xx}}{(1+\epsilon^2 h_x^2)^{3/2}}; \\ w = h_t + u h_x.\end{gathered} \tag{6.21}$$

Small inclination or horizontal substrate

The standard procedure for solving the rescaled momentum equations involves expansion of all fields as series in ϵ so the equations can be solved order by order. The resulting non-linear partial differential equation [5] explicitly contains ϵ so it consists of terms of different order. The approach used here for studying the situation of thin liquid film on a slightly inclined or horizontal solid substrate suggests that all physically interesting effects enter the lowest order equations. To achieve this, the dependent variables and dimensionless numbers are rescaled [89]. A new $O(1)$ variable is introduced, considering the inclination of the substrate small ($\alpha \ll 1$):

$$\alpha' = \frac{\alpha}{\epsilon} \approx \frac{\sin\alpha}{\epsilon} \quad \Longrightarrow \quad \sin\alpha \to \epsilon\alpha', \quad \cos\alpha \to 1 - O(\epsilon^2)$$

After choosing

$$Ca' = \frac{Ca}{\epsilon^2}; \qquad \vec{v} = \frac{\vec{v'}}{\epsilon},$$

where the fact that for small α all velocities are small is taken into account. Now we can drop the dashes and write the lowest order in ϵ of the transport equations:

$$u_{zz} = p_x - G\alpha, \tag{6.22}$$

$$p_z = -G. \tag{6.23}$$

The continuity equation reads

$$u_x + w_z = 0. \tag{6.24}$$

The boundary condition at $z = 0$ is

$$u = w = 0. \tag{6.25}$$

The boundary conditions at the surface $z = h(x)$ are written as

$$w = \partial_t h + u\partial_x h, \tag{6.26}$$

$$u_z = 0, \tag{6.27}$$

$$p = -\frac{h_{xx}}{Ca} + \Pi. \tag{6.28}$$

After solving the system the pressure and velocity fields are obtained:

$$p(x,z) = -Gz + Gh - \Pi(h) - \frac{h_{xx}}{Ca}, \tag{6.29}$$

$$u(x,z) = \left(\frac{z^2}{2} - zh\right)(p_x - G\alpha). \tag{6.30}$$

Finally, from the kinematic boundary condition and continuity equation we obtain

$$\partial_t h = -\partial_x \Gamma, \qquad \Gamma = \int_0^h u dz. \tag{6.31}$$

Here Γ has the meaning of flow in the laboratory frame. Substituting (6.29) and (6.30) into (6.31), can be obtained the thickness evolution equation for a film on a slightly inclined substrate:

$$\partial_t h = -\partial_x \left\{ \frac{h^3}{3} \left[\partial_x \left(\frac{h_{xx}}{Ca} - Gh - \Pi(h) \right) + G\alpha \right] \right\}. \tag{6.32}$$

If Ca is eliminated by a further rescaling, a more general form can be given:

$$\partial_t h = -\partial_x \{ Q(h) \partial_x [\partial_{xx} h - \partial_h f(h)] + \chi(h) \} \tag{6.33}$$

where $Q(h)$ is a mobility factor and $\chi(h)$ represents a generalised driving parallel to the substrate. The use of slip boundary conditions at the substrate leads to a different Q and χ but has no effect on the equation otherwise. The term in square brackets represents the negative of a pressure consisting of the Laplace term $\partial_{xx} h$ and an additional contribution $-\partial_h f(h)$ written as the derivative of a local free energy. The latter has to be specified for the respective studied problem.

Appendix B

Continuation Software: Auto 2000

B.1 Continuation procedure

In this section the principle of continuation is introduced and the application on the software package auto200 to solve thin film equation, Eq. (3.11), is explained including the developed C code.

The continuation techniques, also called path following methods, are in common use for parametric analysis of dynamical systems, in particular to study steady and stationary solutions and their bifurcations. A numerical continuation is an algorithm which takes as input a system of parametrized nonlinear equations and an initial solution, and gives, as result, a set of points which correspond to the solution. Numerical continuation is a method of computing approximate solutions of a system of parameterised nonlinear equations. Numerical continuation techniques has a great degree of acceptance in the study of chaotic dynamical systems. The reason for this acceptance is from the fact that different non-linear dynamical systems behave in a deterministic and predictable manner within a range of parameters which are included in the equations of the system. However, for a certain parameter value the system starts behaving chaotically and hence it become necessary to follow the parameter in order to be able to decipher the occurrences of when the system starts being non-predictable, and what exactly (theoretically) makes the system become unstable.

Even if several software packages which include continuation techniques have been developed, here, we use the package auto2000, based on a C code (the previous version, AUTO97 being based on a FORTRAN 77 code) which was developed by Doedel et al. [31, 28, 29], and it is available from the Applied Mathematics Department at the California Institute of Technology and form the Computer Science Department at Concordia University. The details of the applied

principles are highly technical and beyond the scope of this appendix.

AUTO can be employed to perform a limited bifurcation analysis of algebraic systems

$$f(u,p) = 0, \qquad f(\cdot,\cdot), u \in R^n, \tag{6.34}$$

and of systems of ordinary differential equation (ODEs) of the form

$$u'(t) = f(u(t),p), \qquad f(\cdot,\cdot), u(\cdot) \in R^n, \tag{6.35}$$

Here p denotes one or more free parameters.

In some cases it can be used to determine steady and stationary solution (as e.g. travelling waves) for partial differential equations (PDE).

Specifically, for Eq. (6.34) the program can compute solution branches, locate branch points and automatically compute bifurcation branches, locate Hopf bifurcation points, locate folds (limit points) and continue these in two parameters.

For ODE, Eq. (6.34), it can compute branches of stable and unstable periodic solutions and compute the Floquet multipliers, which determine stability, along these branches. Starting data for the computation of periodic orbits are generated automatically at Hopf bifurcation points. AUTO accepts only first order systems of autonomous ODEs, then, one can rewrite the system into the suitable standard form. Furthermore, the suitable boundary conditions have to be given. Having specified the ODE system in standard form with boundary and integral conditions AUTO then tries to find stationary solutions to the discretized system, by using a combination of Newton and Chord iterative methods. When the solution has converged AUTO proceeds along the solution branch by a small step in the parameter space and restarts the iteration. Usually the problem which arise is to provide AUTO with an initial nonuniform solution, from where the continuation can proceed. In the most cases the continuation can start at the bifurcation point where the uniform solution will change its stability and to give AUTO a periodic solution (e.g. a sine or cosine function with a very small amplitude). AUTO also computes eigenvalues which are used to detect bifurcations.

In the last case, for PDE, the program can trace branches of spatially homogeneous solutions and as well can compute curves of stationary solutions these being subject of user-specified boundary conditions.

The next section will present the complete code for thin film equation with the necessary comments.

The corresponding thin film thickness equation (for which the source code in the next section is given) is:

$$\partial_t h \;=\; -\partial_x \left\{ Q(h)\, \partial_x \left[\partial_{xx} h - \partial_h f(h) \right] + Q(h)\alpha \right\} \tag{6.36}$$

where

$$\partial_h f(h) = \Pi(h) \tag{6.37}$$

or

$$\partial_h f(h) = -\Pi(h) \tag{6.38}$$

but this is a question of conventions.

B.2 Complete AUTO200 code for thin film equation

```
/*
Numerical analysis of thin film equation (with disjoining pressure)
The disjoining presure is defined as:
disj = bb/hh^3 - 1/h^6 where bb > 0
*/

/* standard files which have to be included */
#include <stdlib.h>
#include <stdio.h>
#include <sys/stat.h>
#include "auto_f2c.h"

int func (integer ndim, const doublereal *u, const integer *icp,
          const doublereal *par, integer ijac,
          doublereal *f, doublereal *dfdu, doublereal *dfdp)
{
/* variable declaration */
  doublereal hh, hx, hxx, xx;
  doublereal hu, eps, bb, per, c0, alp, vv;
  doublereal tpi, loga, qq, disj, disj0, disjh, disjh0, gradterm;
```

```
/* assing for the variables and parameters a useful name */
  hu = par[0];
  hh = u[0]+hu;
  hx = u[1];
  hxx = u[2];
  tpi = (doublereal)8.0*atan(1.0);

/* defining "eps" which is a "virtual parameter" that
"virtually" transforms the conservative in a dissipative
system (with the same solutions)
*/
  eps = par[1];
  bb = par[2];
  per = par[4];
  c0 = par[5];
  alp = par[40];
  vv = par[41];

/* define the disjoining pressure, "disj" */
  qq = pow(hh,3.0);

  disj = bb/pow(hh,3.0) - 1/pow(hh,6.0);
  disj0 = bb/pow(hu,3.0) - 1/pow(hu,6.0);
  disjh = -3.0*bb/pow(hh,4.0) + 6.0/pow(hh,7.0);
  disjh0 = -3.0*bb/pow(hu,4.0) + 6.0/pow(hu,7.0);
  gradterm = alp;

/* specify the equations in AUTO format */
  f[0] = per*hx - eps * (disj - disj0);
  f[1] = per*(hxx + eps*hx);
  f[2] = per*(disjh*hx+c0/qq-gradterm+vv*hh/qq);

  return 0;
}
```

```
int stpnt (integer ndim, doublereal t,
           doublereal *u, doublereal *par)
{
  doublereal hh, hx, hxx, xx;
  doublereal hu, eps, bb, per, c0, alp, vv;
  doublereal tpi, qq, disj, disj0, disjh, disjh0, ampl;

/* specify the initial values for variables */
  tpi = (doublereal)8.0*atan(1.0);
  hu  = (doublereal)5.0;
  eps = (doublereal)0.0;
  bb = (doublereal)0.2;
  c0 = (doublereal)0.0;
  alp = (doublereal)0.0;
  vv = (doublereal)0.0;

  disjh0 = -3.0*bb/pow(hu,4.0) + 6.0/pow(hu,7.0);
  per = tpi/sqrt(-disjh0);

/* specify the initial values for parameters */
  par[0] = hu;
  par[1] = eps;
  par[2] = bb;
  par[4] = per;
  par[5] = c0;
  par[40] = alp;
  par[41] = vv;
  par[10] = 1.0;
  ampl = (doublereal)0.0000001;

/* initialize the solution */
  u[0] = ampl*sin(tpi*t);
  u[1] = ampl*tpi*cos(tpi*t);
```

```
  u[2] = -ampl*tpi*tpi*sin(tpi*t);

  return 0;
}

int bcnd (integer ndim, const doublereal *par, const integer *icp,
          integer nbc, const doublereal *u0, const doublereal *u1,
  integer ijac, doublereal *fb, doublereal *dbc)
{
integer dbc_dim1;
  dbc_dim1 = nbc;

/*
the number of boundary conditions (NBCD) and conservation relations
(NINT) imposes a constraint on the number of parameters (NPAR),
that AUTO can vary during the continuation process,
(NPAR = NBCD + NINT - NDIM + 1)
*/

/* specify boundary conditions */
  fb[0] = u0[0]-u1[0];
  fb[1] = u0[1]-u1[1];
  fb[2] = u0[2]-u1[2];
  return 0;
}

int icnd (integer ndim, const doublereal *par, const integer *icp,
          integer nint, const doublereal *u, const doublereal *uold,
          const doublereal *udot, const doublereal *upold, integer ijac,
          doublereal *fi, doublereal *dint)
{
integer dint_dim1;
  dint_dim1 = nint;
```

```
/* specify integral conditions */
  fi[0] = u[0] - 0.0;

/*
For autonomous systems it is necessary to introduce a pinning condition
that breaks the translational symmetry of the solutions. AUTO provides
the possibilities to formulate this pinning condition either as an
additional boundary or integral condition.
*/
/* integral pinning condition to break Translations symmetry */
  if(nint>1) fi[1] = u[0]*upold[0];

  return 0;
}

int fopt (integer ndim, const doublereal *u, const integer *icp,
          const doublereal *par, integer ijac,
          doublereal *fs, doublereal *dfdu, doublereal *dfdp)
{
  return 0;
}

int pvls (integer ndim, const doublereal *u,
          doublereal *par)
{
  integer tmp;
  doublereal hu, gg, hydrengy, gradengy, disjengy, energy0;
  extern doublereal getp();
  extern doublereal getpuwe();

/* Parameters set in this subroutine should be considered as "solution */
/* measures" and be used for output purposes only. */
/* They should never be used as 'true'' continuation parameters. */
```

```
/* They may, however, be added as ``over-specified parameters'' in the */
/* parameter list associated with the AUTO-Constant NICP, in order to */
/* print their values on the screen and in the ``p.xxx file. */

/* They may also appear in the list associated with AUTO-constant NUZR. */

/* For algebraic problems the argument U is, as usual, the state vector. */
/* For differential equations the argument U represents the approximate */
/* solution on the entire interval [0,1]. In this case its values must */
/* be accessed indirectly by calls to GETP, as illustrated below. */

/* Set PAR(6) equal to the Amplitude of U(0) */
  par[6] = getp("MAX", 1, u) - getp("MIN", 1, u);

/* Set PAR(7) equal to the Integral of U(0) */
  par[7] = getp("INT", 1, u);

  par[45] = getp("MIN", 2, u);
  par[46] = getp("MAX", 2, u);

  return 0;
}
```

Appendix C

Numerical Method to Solve Cahn-Hilliard Equation

In the present appendix we briefly introduce and analyse a semi-implicit time discretisation scheme used to accurately solve the Cahn-Hilliard equation. For more detailed information regarding that method see [49].

The scheme is applied for all time steps, the main feature of the method is the separation of the contractive and expansive terms across the time step. It is unconditionally gradient stable. The scheme allow the Cahn-Hilliard equation to be solved using a workstation instead the need to use a supercomputer.

The Cahn-Hilliard equation is very difficult to solve numerically because the equations are so called stiff and an efficient numerical solution is needed. To accurately solve them a fine discretisation of space is required. In order to solve the equations a semi-implicit method is applied which resolves the issues regarding the stiffness and solvability.

The equation is a fourth order nonlinear parabolic partial differential equation,

$$\frac{\partial \phi}{\partial t} = \triangle[-\epsilon^2 \triangle \phi + f(\phi)] \tag{6.39}$$

where $\phi = \phi(\vec{x}, t)$ and

$$0 < \epsilon \ll 1, \vec{x} \in \Omega, t > 0. \tag{6.40}$$

The nonlinear term considered in the simulations will be $f(\phi) = \phi^3 - \phi$, but the properties of the numerical method are equal for other nonlinear terms. The operator $\triangle$ is the laplacian. The linear part of $\triangle f(\phi)$ is, for one particular choice, $-\triangle u$. This term is responsible for the unstable dynamics of the Cahn-Hilliard equation, including as well the instability of constant solutions near $\phi = 0$. The nonlinear term of $\triangle f(\phi)$, $\triangle \phi^3$, has a stabilising effect.

The boundary conditions for the system are (no flux condition)

$$\nabla\phi \cdot \vec{n} = \nabla(\Delta\phi - f(\phi)) \cdot \vec{n} = 0 \tag{6.41}$$

where $\vec{n}$ is the outward normal on the boundary of Ω. These boundary conditions leave the spatial average of $\phi(\vec{x}, t)$ invariant in time.

Using finite differences, the Cahn-Hilliard equation can be discretized using centred approximations to the spatial derivative operators on $\Omega = [0, 1] \times [0, 1]$. The discrete approximation of $\phi(ih, jh, nk)$ can be ϕ_{ij}^n, where the time step is k, the spatial discretisation is $h = \frac{1}{m}$ and $m = O(\epsilon^{-1})$. Under these conditions, the standard centred difference approximation of the laplacian is

$$h^2\Delta_h\phi_{ij}^n = \phi_{i+1,j}^n + \phi_{i-1,j}^n + \phi_{i,j+1}^n + \phi_{i,j-1}^n - 4\phi_{i,j}^n \tag{6.42}$$

It will be used to approximate the continuos laplacian on the discrete grid.

The key to obtain the expected stability and solvability features of the time marching scheme is to separate the nonlinear terms in two parts, a stabilising term and a growth term, and finally to split those terms across the time step. To achieve this the most logical way is with a time marching scheme

$$\frac{\phi_{ij}^{n+1} - \phi_{ij}^n}{k} = -\epsilon^2\Delta_h^2\phi_{ij}^{n+1} + \Delta_h(\phi_{ij}^{n+1})^3 - \Delta_h\phi_{ij}^n. \tag{6.43}$$

To obtain ϕ_{ij}^{n+1} using this scheme, one needs to solve the nonlinear equations

$$(1 + k\epsilon^2\Delta_h^2)\phi_{ij}^{n+1} - k\Delta_h(\phi_{ij}^{n+1})^3 = (1 - k\Delta_h)\phi_{ij}^n \tag{6.44}$$

on every grid point.

The equations in Eq. (6.44) are a large coupled set of nonlinear equations.

When working with laplacian discretisations it would be recommended to use FFT based methods to invert the operators because the FFT basis functions are eigenvectors of the difference operators. In order to use FFT methods we must assure that the operator is linear and has constant coefficient. So, the effort required to solve the linear system is reduced to the effort to perform the FFTs. Briefly, one can say that FFT based methods consider the fact that the basis functions of the FFT are eigenfunctions of the discrete laplacian. The cosine basis functions that are used in the discrete cosine transformation are eigenfunctions of the Cahn-Hilliard equations with the boundary conditions mentioned above. This technique is used as the basis for the iterative solution of the Eq. (6.44).

Due to the fact that time marching method is unconditionally stable, one can take large steps and solve Cahn-Hilliard effectively over long time intervals. Fig. 3.14 and Fig. 3.15 show result from the simulations of Cahn-Hilliard equation using the described method.

Appendix D

Kinetic Monte Carlo Method

In order to study the diffusion process of neutrons in fissionable material, at the end of the Second World War, von Neumann, Ulam, and Metropolis developed the Monte Carlo method. The name "Monte Carlo" was suggested by Nicholas Metropolis in 1947 and it has been chosen because of its roots in the extensive use of random numbers in the calculation, much like a game played with a shuffled deck of cards, and has been used in the title of a paper which describe the early work at Los Alamos National Laboratory, [74].

Statisticians had used model sampling experiments to investigate problems before this time but the novel contribution of von Neumann and Ulam was to realize that determinate mathematical problems could be solved by finding a probabilistic analogue which is then solved by a stochastic sampling experiment. A Monte Carlo simulation will follow the "time dependence" of a model for which growth, or change, will not act exactly like Newton's equation of motion predicted, but in a stochastic way which depends on a sequence of random numbers. This sequence of random numbers are generated during the simulation. If a different sequence of random numbers is generated, for a second run, the simulation will not return identical results but will lead to values which will agree with the values obtained from the first simulation considering some "statistical error". These are tasks that are well suited to a computer and the growth of Monte Carlo method can be linked to the rapid development of these machines.

In 1901 Monte Carlo technique has been used for a simple integration in order to estimate the value of π. Since then, the method has grown to the point where it is, arguably, maybe the most powerful and commonly used technique for analysing complex problems. A large number of different physical phenomena which can be explored fall in this category. For example growth phenomena which involves macroscopic objects, like DLA growth of colloidal particles (the DLA phenomenon was first discovered by MC simulation), random brownian motion, etc, can be also studied. Furthermore, for example using Monte Carlo simulations of lattice gauge models, some most significant advances in understanding the theory of elementary particles have been possible.

But even if Monte Carlo is a successful method for simulations and for studying different complex

problems, it is a cpu intensive task to do them and there are some difficulties which can be encountered, like limited computer time and memory. Simulation which needs years of cpu time is simply impractical. In a similar manner, a calculation which needs memory which far exceed what is available, can be done only by using some advanced and sophisticated programming techniques which will slow down the running speed and increase the probability of errors. It is important, as well, that the user should consider first the requirements for both cpu time and memory before starting the project in order to have a realistic plan to obtain the necessary resources to do simulations for a problem properly. Sometimes this may require the developing of a new and more efficient algorithm for simulation and to invent new strategies to overcome such problems and difficulties. That is why it constitutes a very exciting and challenging field of research.

The term Monte Carlo (MC) method does not represent just a single method, instead, the term describes a large and widely used class of approaches, a wide variety or methods, with overlaps, in theoretical physics, chemistry, and engineering where random numbers play an essential role.

- Metropolis Monte Carlo - algorithm that determines wether a process should happen or not
- Thermodynamics Monte Carlo - thermodynamics quantities
- Lattice Monte Carlo - Monte Carlo through lattice based method
- Kinetic Monte Carlo - time evolution of a system
- Quantum Monte Carlo - electronic structure calculation

However, these approaches tend to follow a particular algorithm:

1. define a domain of possible inputs
2. generate the inputs randomly from the domain using a certain specified probability distribution
3. perform a deterministic computation using the inputs generated at previous step
4. combine the results of the individual computations into the final result

A widely known application of random numbers is the numerical evaluation of integrals which are intractable by analytic techniques in a high-dimensional space. There, the integral is replaced by a sum over function evaluations at discrete support points. For simplicity, the description of the method as applied to one-dimensional integrals is given below, but it should be understood that these techniques are extended and often most cost effective when applied to multidimensional integrals. In the simplest case one would like to obtain the integral $f(x)$ over some fixed interval:

$$y = \int_a^b f(x)\, dx. \tag{6.45}$$

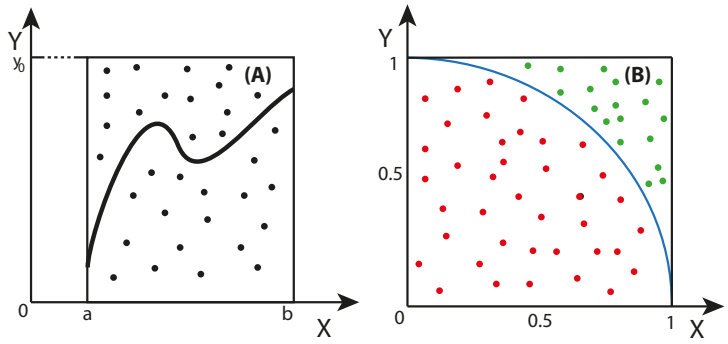

Figure 6.2: Simple representation of "hit-or-miss" Monte Carlo integration: (A) of a function $f(x)$, given by the solid curve, between $x = a$ and $x = b$. N points are randomly dropped into the box, N_0 of them fall below the curve. The integral is estimated using Eq. (6.45) and (B) to estimate the value of π using simple sampling Monte Carlo [74].

Fig. 6.2 (A) is shown a representation of this problem.

A straightforward Monte Carlo solution to this problem via "hit-or-miss" (or acceptance-rejection) method is to draw a box extending from a to b and from 0 to y_0 where $y_0 = f(x)$ throughout this interval, Fig. 6.2. Estimation of the integral is given by the fraction of points which fall below the solid curve times the area of the box:

$$y_{est} = (N_0/N) \cdot [y_0(b-a)] \tag{6.46}$$

The estimation is better if $N \to \infty$.

Another interesting problem is the estimation of a numerical value of π. A representation of the problem is given in Fig. 6.2 (B) and the procedure is the follow. Choose randomly N points in the XY plane so that $0 < x < 1$ and $0 < y < 1$. Calculate the distance from the origin for each point and count those which are less then a distance of 1 from origin. The fraction of points which satisfy this condition, N_0/N provide an estimate for the area of one-quarter of a circle so that $\pi = 4N_0/N$. Repeating this procedure multiple times and the results can be used to estimate the error.

One can notice how the approximation of π follows the general algorithm of Monte Carlo method mentioned above. Starting by defining a domain of inputs: in this case, it's the square which circumscribes our circle. The next step is the generation of inputs randomly (scatter individual grains within the square), then perform a computation on each input (test whether it falls within the circle). At the end, the results are combined into our final result, the approximation of π.

Another example which is introduced here is the Ising model. The Ising model is one of the simplest lattice models which one can imagine and its behaviour has been studied for a long time. The simple Ising model consists of spins which are confined to the sites of a lattice and which may have only the

values $+1$ and -1. They interact with the neighbours on the lattice with the interaction constant J. Ising proposed that adjacent spins should have an energy associated with the bond between them, such that opposing adjacent spins have an energy cost $(+J)$ and parallel spins are energetically favourable (J). The hamiltonian of this model is given by

$$H = -\frac{J}{2}\sum_{ij}\sigma_i\sigma_j - H\sum_i \sigma_i \tag{6.47}$$

where $\sigma = \pm 1$. The Ising model has been solved exactly in one dimension showing that there is no phase transition. In two dimensional case Lars Onsager obtained the exact results [87] which showed that there is a second order phase transition with divergences in the specific heat, susceptibility and correlation length. Furthermore, in three dimensions such a solution has yet to be found. For this reason, the system lends itself well to study by the Monte Carlo method. The Metropolis algorithm is an excellent tool to this end.

Metropolis algorithm is a particular variation on the Monte Carlo method which represents a simple way to evolve a system towards its equilibrium state. Described in terms of the Ising model, the Metropolis algorithm proceeds according to the following steps:

1. choose a random initial state
2. choose a spin site , i at random, and temporary inverted, taking the system from state 1 to the other state 2
3. the energy change $\Delta E = E(2) - E(1)$ is evaluated, and if the inversion is found to be energetically favourable ($\Delta E < 0$), then it is retained
4. if $\Delta E > 0$ generate a random number r such that $0 < r < 1$
5. if $r < \exp(\Delta E/k_B T)$ then the spin flip is accepted, if $r > \exp(\Delta E/k_B T)$ then the spin is flipped back to its original state

The entire process is then repeated, until the system reaches equilibrium. In Fig 6.3 is shown configurations for finite 150x150 Ising lattices. At temperatures well above the critical temperatures, the spin arrangement converges to a nearly random arrangement, independent of the starting state. Above the critical temperature, there is a single thermodynamic state and this has zero magnetisation. The spin arrangement is truly random at infinite temperature Fig. 6.3 (a). For temperatures near the transition temperature, there are large clusters of spins with the same orientation, which fluctuate only very slowly. This is because the "correlation length" of an infinitely large system diverges at the critical point, Fig. 6.3 (b). Below the critical temperature, there are two thermodynamic states (the "up spin" state with positive magnetisation and the "down spin" state negative magnetisation) and the system stays in one or

the other depending on how the spins are initialised. Eventually, if you let the simulation run for a long time, one of the states will win. Which one wins depends on the random thermal fluctuations. There is equal probability for it to be the "up spin" or "down spin" state, Fig. 6.3 (c).

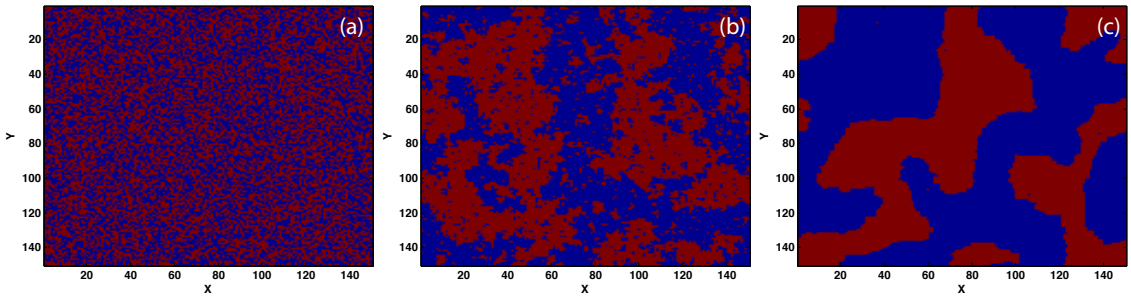

Figure 6.3: Typical spin configuration for the two-dimensional Ising square lattice, 150x150. The equilibrium state of the Ising model (spin +1 is blue, -1 is red) is calculated by a Metropolis algorithm at different temperatures showing the system (a) well above the critical temperature, (b) exactly at the critical temperature, and below the critical temperature (c).

The recipe for the Monte Carlo method given so far applies to non-conserved observables (e.g., the magnetisation). For a conserved quantity (e.g., the concentration of particles), one uses Kawasaki dynamics:

- choose a pair of (neighbouring) spins
- exchange the spins using Metropolis acceptance criterion

Metropolis Monte Carlo method offers an elegant and very good way to study different complex systems. It is at the heart of many of the simulation studies of equilibrium properties of physical systems. It uses simple rules involving almost nothing more than moving one atom at a time by a small random displacement. But, in the 1960's scientists started to develop a different type of Monte Carlo algorithm for evolving systems from state to state, dynamically, so called Kinetic Monte Carlo method (KMC). The popularity and the range of applications which kinetic Monte Carlo simulation can study, has continued to grow and KMC is now a common tool for studying surface diffusion, molecular beam epitaxy growth (MBE), chemical vapour deposition (CVD), defects formation and diffusion, oxidation (thermal growth, atomic layer deposition techniques). An appealing property of KMC is that it can, in principle, give the exact dynamical evolution of a system.

The kinetic Monte Carlo (KMC) method is a Monte Carlo method computer simulation intended to simulate the time evolution of some processes that occur with a given known rate in nature. It is important to understand that these rates are inputs to the KMC algorithm, the method itself cannot predict them.

The KMC method is essentially the same as so called the Dynamic Monte Carlo method (DMC), the main difference is in terminology and usage areas: KMC is used mainly in physics while the "dynamic" method is mostly used in chemistry.

The time scale one would like to cover by the simulation should be of the same order as the actual time used in experimental studies for the corresponding process which can be of the order of seconds, minutes. In advantage over classical Monte Carlo method, a kinetic Monte Carlo simulation allows us to assign to the simulation steps the meaning of a physical time. The algorithm proposed and used in the thesis is almost the same with the algorithm for classical Monte Carlo simulation described above with one exception. We assign an initial time t_0 for the initial starting configuration. The simulation starts and when the system evolve to the next state (a cell containing liquid is evaporating), we update our "real" time step, increasing the previous time with ΔT, then, the new time will be $t_1 = t_0 + \Delta T$ or written for general case: $t_{new} = t_{prev} + \Delta T$.

The Kinetic Monte Carlo algorithm becomes:

1. choose a random initial state
2. assign an initial time t_0 to the system
3. choose a spin site , i at random, and temporary inverted, taking the system from state 1 to the other state 2
4. the energy change $\Delta E = E(2) - E(1)$ is evaluated, and if the inversion is found to be energetically favourable ($\Delta E < 0$), then it is retained
5. if $\Delta E > 0$ generate a random number r such that $0 < r < 1$
6. if $r < \exp(\Delta E / k_B T)$ then the spin flip is accepted, if $r > \exp(\Delta E / k_B T)$ then the spin is flipped back to its original state
7. update the time step according $t_{new} = t_{prev} + \Delta T$

The mentioned Kinetic Monte Carlo algorithm was used to analyse the influence of the nanoparticles on the basic dewetting behavior, i.e., on spinodal dewetting, on dewetting by nucleation and growth of holes and to study fingering instabilities process for straight and circular front.

The Monte Carlo method has a long and considerable history in Physics and science. Back in 1949, Metropolis and Ulam, [74], presented the use of Monte Carlo method simulations by using of "modern computing machine". They not only emphasised the advantages of the method but also, in addition, they gave examples. With the very rapidly increasing of computer power, it is already clear that computer simulations will be able to rapidly increase in sophistication, to allow us to make more subtle comparisons with the experiments.

This complementary section which accompanies the thesis is meant to give a short introduction and overview of Kinetic Monte Carlo Method and it is not intended to give too many details, so, the reader is encouraged to research the literature in order to find more about that fascinating subject.

Bibliography

[1] D. M. Anderson, G. B. McFadden, and A. A. Wheeler. Diffuse-interface methods in fluid mechanics. *Ann. Rev. Fluid Mech.*, 30:139–165, 1998.

[2] P. Ball. *The self-made tapestry*. Oxford University Press, Oxford, 1999.

[3] J. Becker, G. Grün, R. Seemann, H. Mantz, K. Jacobs, K. R. Mecke, and R. Blossey. Complex dewetting scenarios captured by thin-film models. *Nat. Mater.*, 2:59–63, 2003.

[4] H. Bénard. Les tourbillons cellulaires dans une nappe liquide. *Rev. Gén. Sci. Pures Appl.*, 11:1261–1271, 1900.

[5] D. J. Benney. Long waves on liquid films. *J. Math. & Phys.*, 45:150–155, 1966.

[6] M. Bestehorn and K. Neuffer. Surface patterns of laterally extended thin liquid films in three dimensions. *Phys. Rev. Lett.*, 87:046101, 2001.

[7] J. Bischof, D. Scherer, S. Herminghaus, and P. Leiderer. Dewetting modes of thin metallic films: Nucleation of holes and spinodal dewetting. *Phys. Rev. Lett.*, 77:1536–1539, 1996.

[8] E. Bormashenko, R. Pogreb, O. Stanevsky, Y. Bormashenko, T. Stein, V. Z. Gaisin, R. Cohen, and O. V. Gendelman. Mesoscopic patterning in thin polymer films formed under the fast dip-coating process. *Macromol. Mater. Eng.*, 290:114–121, 2005.

[9] E. Bormashenko, R. Pogreb, O. Stanevsky, Y. Bormashenko, T. Stein, and O. Gengelman. Mesoscopic patterning in evaporated polymer solutions: New experimental data and physical mechanisms. *Langmuir*, 21:9604–9609, 2005.

[10] J.-H. Bradt, M. Mertig, B. Winzer, U. Thiele, and W. Pompe. Collagen assembly from acid solution to networks on solid surfaces and to fibrils. In *Proceedings of the Third International Conference on Intelligent Materials and Third European Conference on Smart Structures and Materials Lyon June 1996*, pages 78–82. SPIE–The International Society for Optical Engineering, 1996. Proc. SPIE 2779.

[11] F. Brochard-Wyart and J. Daillant. Drying of solids wetted by thin liquid films. *Can. J. Phys.*, 68:1084–1088, 1989.

[12] F. Brochard-Wyart and C. Redon. Dynamics of liquid rim instabilities. *Langmuir*, 8:2324–2329, 1992.

[13] L. Brusch, H. Kühne, U. Thiele, and M. Bär. Dewetting of thin films on heterogeneous substrates: Pinning versus coarsening. *Phys. Rev. E*, 66:011602, 2002.

[14] J. W. Cahn. Phase separation by spinodal decomposition in isotropic systems. *J. Chem. Phys.*, 42:93–99, 1965.

[15] J. W. Cahn and J. E. Hilliard. Free energy of a nonuniform system. 1. Interfacual free energy. *J. Chem. Phys.*, 28:258–267, 1958.

[16] I. Cantat and C. Misbah. Dynamics and similarity laws for adhering vesicles in haptotaxis. *Phys. Rev. Lett.*, 83:235–238, 1999.

[17] J. Q. Carou, N. J. Mottram, S. K. Wilson, and B. R. Duffy. A mathematical model for blade coating of a nematic liquid crystal. *Liq. Cryst.*, 34:621–631, 2007.

[18] A. Chatterjee and D. G. Vlachos. An overview of spatial microscopic and accelerated kinetic Monte Carlo methods. *J. Comput-Aided Mater. Des.*, 14:253–308, 2007.

[19] N. Clarke. Instabilities in thin-film binary mixtures. *Eur. Phys. J. E*, 14:207–210, 2004.

[20] N. Clarke. Toward a model for pattern formation in ultrathin-film binary mixtures. *Macromolecules*, 38:6775–6778, 2005.

[21] M. C. Cross and P. C. Hohenberg. Pattern formation out of equilibrium. *Rev. Mod. Phys.*, 65:851–1112, 1993.

[22] P.-G. de Gennes. Wetting: Statics and dynamics. *Rev. Mod. Phys.*, 57:827–863, 1985.

[23] R. D. Deegan. Pattern formation in drying drops. *Phys. Rev. E*, 61:475–4–85, 2000.

[24] R. D. Deegan, O. Bakajin, T. F. Dupont, G. Huber, S. R. Nagel, and T. A. Witten. Capillary flow as the cause of ring stains from dried liquid drops. *Nature*, 389:827–829, 1997.

[25] R. D. Deegan, O. Bakajin, T. F. Dupont, G. Huber, S. R. Nagel, and T. A. Witten. Contact line deposits in an evaporating drop. *Phys. Rev. E*, 62:756–765, 2000.

[26] B. V. Derjaguin, N. V. Churaev, and V. M. Muller. *Surface Forces*. Consultants Bureau, New York, 1987.

[27] B. V. Derjaguin and L. D. Landau. Theory of the stability of strongly charged lyophobic sols and of the adhesion of strongly charged particles in solutions of electrolytes. *Acta Physicochim. U.R.S.S.*, 14:633–662, 1941.

[28] E. Doedel, H. B. Keller, and J. P. Kernevez. Numerical analysis and control of bifurcation problems (I) Bifurcation in finite dimensions. *Int. J. Bif. Chaos*, 1:493–520, 1991.

[29] E. Doedel, H. B. Keller, and J. P. Kernevez. Numerical analysis and control of bifurcation problems (II) Bifurcation in infinite dimensions. *Int. J. Bifurcation Chaos*, 1:745–72, 1991.

[30] E. J. Doedel, A. R. Champneys, T. F. Fairgrieve, Y. A. Kuznetsov, B. Sandstede, and X. J. Wang. *AUTO97: Continuation and bifurcation software for ordinary differential equations*. Concordia University, Montreal, 1997.

[31] E. J. Doedel, R. C. Paffenroth, H. B. Keller, D. J. Dichmann, J. Galan-Vioque, and A. Vanderbauwhede. Computation of periodic solutions of conservative systems with application to the 3-body problem. *Int. J. Bifurcation Chaos*, 13:1353–1381, 2003.

[32] I. Durand, P. Jonson, C. Misbah, A. Valance, and K. Kassner. Adhesion-induced vesicle propulsion. *Phys. Rev. E*, 56:R3776–R3779, 1997.

[33] M. Elbaum and S. G. Lipson. How does a thin wetted film dry up? *Phys. Rev. Lett.*, 72:3562–3565, 1994.

[34] M. Elbaum and S. G. Lipson. Pattern formation in the evaporation of thin liquid films. *Israel J. Chem.*, 35:27–32, 1995.

[35] M. H. Eres, L. W. Schwartz, and R. V. Roy. Fingering phenomena for driven coating films. *Phys. Fluids*, 12:1278–1295, 2000.

[36] R. Fetzer, K. Jacobs, A. Münch, B. Wagner, and T. P. Witelski. New slip regimes and the shape of dewetting thin liquid films. *Phys. Rev. Lett.*, 95:127801, 2005.

[37] K. A. Fichthorn and W. H. Weinberg. Theoretical foundations of dynamic monte-carlo simulations. *J. Chem. Phys.*, 95:1090–1096, 1991.

[38] L. Frastia, A. J. Archer, and U. Thiele. Dynamical model for the formation of patterned deposits at receding contact lines. 2010. (preprint at http://arxiv.org/abs/1008.4334).

[39] M. Hamieh P. Damman S. Gabriele T. Vilmin G. Reiter, S. Al Akhrass and E. Raphael. Dewetting as an investigative tool for studying properties of thin polymer films. *Eur. Phys. J. Special Topics*, 166:165–172, 2009.

[40] D. Gallez and W. T. Coakley. Far-from-equilibrium phenomena in bioadhesion processes. *Heterogeneous Chem. Rev.*, 3:443–475, 1996.

[41] G. L. Ge and L. Brus. Evidence for spinodal phase separation in two-dimensional nanocrystal self-assembly. *J. Phys. Chem. B*, 104:9573–9575, 2000.

[42] W. M. Gelbart, R. P. Sear, J. R. Heath, and S. Chaney. Array formation in nano-colloids: Theory and experiment in 2D. *Faraday Discuss.*, 112:299–307, 1999.

[43] H. Gilhoj, C. Jeppesen, and O. G. Mouritsen. Effects of mobile vacancies on the dynamics of ordering and phase-separation in nonconserved multicomponent systems. *Phys. Rev. E*, 52:1465–1475, 1995.

[44] J. F. Gouyet. Generalized Allen-Cahn equations to describe far-from-equilibrium order-disorder dynamics. *Phys. Rev. E*, 51:1695–1710, 1995.

[45] L. V. Govor, J. Parisi, G. H. Bauer, and G. Reiter. Instability and droplet formation in evaporating thin films of a binary solution. *Phys. Rev. E*, 71:051603, 2005.

[46] L. V. Govor, G. Reiter, J. Parisi, and G. H. Bauer. Self-assembled nanoparticle deposits formed at the contact line of evaporating micrometer-size droplets. *Phys. Rev. E*, 69:061609, 2004.

[47] X. Gu, D. Raghavan, J. F. Douglas, and A. Karim. Hole-growth instability in the dewetting of evaporating polymer solution films. *J. Polym. Sci. Pt. B-Polym. Phys.*, 40:2825–2832, 2002.

[48] M. D. Haw, M. Gillie, and W. C. K. Poon. Effects of phase behavior on the drying of colloidal suspensions. *Langmuir*, 18:1626–1633, 2002.

[49] Yinnian He, Yunxian Liu, and Tao Tang. On large time-stepping methods for the cahn-hilliard equation. *Applied Numerical Mathematics*, 57(5-7):616 – 628, 2007. Special Issue for the International Conference on Scientific Computing.

[50] S. W. Hong, J. F. Xia, and Z. Q. Lin. Spontaneous formation of mesoscale polymer patterns in an evaporating bound solution. *Adv. Mater.*, 19:1413–1417, 2007.

[51] J. Huang, F. Kim, A. R. Tao, S. Connor, and P. Yang. Spontaneous formation of nanoparticle stripe patterns through dewetting. *Nat. Mater.*, 4:896–900, 2005.

[52] J. N. Israelachvili. *Intermolecular and Surface Forces*. Academic Press, London, 1992.

[53] Philibert J. One and a half century of diffusion: Fick, einstein, before and beyond. *Diffusion Fundamentals*, 2:1.1–1.10, 2005.

[54] S. Kalliadasis and U. Thiele, editors. *Thin Films of Soft Matter*. Springer, Wien / New York, 2007. CISM 490.

[55] H. C. Kang and W. H. Weinberg. Dynamic monte-carlo with a proper energy barrier - surface-diffusion and two-dimensional domain ordering. *J. Chem. Phys.*, 90:2824–2830, 1989.

[56] O. Karthaus, L. Grasjö, N. Maruyama, and M. Shimomura. Formation of ordered mesoscopic polymer arrays by dewetting. *Chaos*, 9:308–314, 1999.

[57] D. E. Kataoka and S. M. Troian. A theoretical study of instabilities at the advancing front of thermally driven coating films. *J. Colloid Interface Sci.*, 192:350–362, 1997.

[58] R. Konnur, K. Kargupta, and A. Sharma. Instability and morphology of thin liquid films on chemically heterogeneous substrates. *Phys. Rev. Lett.*, 84:931–934, 2000.

[59] E. L. Koschmieder. On convection under an air surface. *J. Fluid Mech.*, 30:9–15, 1967.

[60] J. S. Langer. *An introduction to the kinetics of first-order phase transitions*, chapter 3, pages 297–363. Cambridge University Press, 1992.

[61] M. I. Larsson. Kinetic monte carlo simulations of adatom island decay on cu(111). *Phys. Rev. B*, 6411:115428, 2001.

[62] S. G. Lipson. Pattern formation in drying water films. *Phys. Scripta*, T67:63, 1996.

[63] G. Liu, C. F. Zhang, J. Zhao, and Y. X. Zhu. Study of the morphology of the three-phase contact line and its evolution by morphological examination after droplet evaporation of aqueous polymer solutions. *Langmuir*, 24:7923–7930, 2008.

[64] J. A. Lundbaek and O. S. Andersen. Spring constants for channel-induced lipid bilayer deformations estimates using gramicidin channels. *Biophys. J.*, 76:889–895, 1999.

[65] A. V. Lyushnin, A. A. Golovin, and L. M. Pismen. Fingering instability of thin evaporating liquid films. *Phys. Rev. E*, 65:021602,1–7, 2002.

[66] H. Maeda. An atomic force microscopy study of ordered molecular assemblies and concentric ring patterns from evaporating droplets of collagen solutions. *Langmuir*, 15:8505–8513, 1999.

[67] H. Maeda. Observation of spatially rhythmic patterns from evaporating collagen solution droplets. *Langmuir*, 16:9977–9982, 2000.

[68] M. Maillard, L. Motte, A. T. Ngo, and M. P. Pileni. Rings and hexagons made of nanocrystals: A Marangoni effect. *J. Phys. Chem. B*, 104:11871–11877, 2000.

[69] C. P. Martin, M. O. Blunt, and P. Moriarty. Nanoparticle networks on silicon: Self-organized or disorganized? *Nano Lett.*, 4:2389–2392, 2004.

[70] C. P. Martin, M. O. Blunt, E. Pauliac-Vaujour, A. Stannard, P. Moriarty, I. Vancea, and U. Thiele. Controlling pattern formation in nanoparticle assemblies via directed solvent dewetting. *Phys. Rev. Lett.*, 99:116103, 2007.

[71] I. S. McKinley, S. K. Wilson, and B. R. Duffy. Spin coating and air-jet blowing of thin viscous drops. *Phys. Fluids*, 11:30–47, 1999.

[72] M. Mertig, U. Thiele, J. Bradt, D. Klemm, and W. Pompe. Dewetting of thin collagenous precursor films. *Appl. Phys. A*, 66:S565–S568, 1998.

[73] M. Mertig, U. Thiele, J. Bradt, G. Leibiger, W. Pompe, and H. Wendrock. Scanning force microscopy and geometric analysis of twodimensional collagen network formation. *Surf. Interface Anal.*, 25:514–521, 1997.

[74] N. Metropolis and S. Ulam. The Monte Carlo method. *J Am Stat Assoc*, 44(247):335–341, 1949.

[75] V. S. Mitlin. Dewetting of solid surface: Analogy with spinodal decomposition. *J. Colloid Interface Sci.*, 156:491–497, 1993.

[76] V. S. Mitlin. Dewetting revisited: New asymptotics of the film stability diagram and the metastable regime of nucleation and growth of dry zones. *J. Colloid Interface Sci.*, 227:371–379, 2000.

[77] P. Moriarty, M. D. R. Taylor, and M. Brust. Nanostructured cellular networks. *Phys. Rev. Lett.*, 89:248303, 2002.

[78] P. Müller-Buschbaum. Dewetting and pattern formation in thin polymer films as investigated in real and reciprocal space. *J. Phys.-Condes. Matter*, 15:R1549–R1582, 2003.

[79] P. Müller-Buschbaum, E. Bauer, S. Pfister, S. V. Roth, M. Burghammer, C. Riekel, C. David, and U. Thiele. Creation of multi-scale stripe-like patterns in thin polymer blend films. *Europhys. Lett.*, 73:35–41, 2006.

[80] A. Münch. Dewetting rates of thin liquid films. *J. Phys.-Condes. Matter*, 17:S309–S318, 2005.

[81] A. Münch and B. Wagner. Contact-line instability of dewetting thin films. *Physica D*, 209:178–190, 2005.

[82] A. Münch, B. Wagner, and T. P. Witelski. Lubrication models with small to large slip lengths. *J. Eng. Math.*, 53:359–383, 2005.

[83] A. Novick-Cohen. The nonlinear Cahn - Hilliard equation: Transition from spinodal decomposition to nucleation behavior. *J. Stat. Phys.*, 38:707–723, 1985.

[84] A. Novick-Cohen and L. A. Segel. Nonlinear aspects of the Cahn - Hilliard equation. *Physica D*, 10:277–298, 1984.

[85] L. Onsager. Reciprocal relations in irreversible processes. I. *Phys. Rev.*, 37(4):405–426, Feb 1931.

[86] L. Onsager. Reciprocal relations in irreversible processes. II. *Phys. Rev.*, 38(12):2265–2279, Dec 1931.

[87] L. Onsager. Crystal statistics. I. A two-dimensional model with an order-disorder transition. *Phys. Rev.*, 65:117–149, 1944.

[88] A. Oron, S. H. Davis, and S. G. Bankoff. Long-scale evolution of thin liquid films. *Rev. Mod. Phys.*, 69:931–980, 1997.

[89] A. Oron and P. Rosenau. Formation of patterns induced by thermocapillarity and gravity. *J. Physique II France*, 2:131–146, 1992.

[90] E. Pauliac-Vaujour and P. Moriarty. Meniscus-mediated organization of colloidal nanoparticles. *J. Phys. Chem. C*, 111:16255–16260, 2007.

[91] E. Pauliac-Vaujour, A. Stannard, C. P. Martin, M. O. Blunt, I. Notingher, P. J. Moriarty, I. Vancea, and U. Thiele. Fingering instabilities in dewetting nanofluids. *Phys. Rev. Lett.*, 100:176102, 2008.

[92] L. M. Pismen. Spinodal dewetting in a volatile liquid film. *Phys. Rev. E*, 70:021601, 2004.

[93] L. M. Pismen and Y. Pomeau. Disjoining potential and spreading of thin liquid layers in the diffuse interface model coupled to hydrodynamics. *Phys. Rev. E*, 62:2480–2492, 2000.

[94] L. M. Pismen and U. Thiele. Asymptotic theory for a moving droplet driven by a wettability gradient. *Phys. Fluids*, 18:042104, 2006.

[95] E. Rabani, D. R. Reichman, P. L. Geissler, and L. E. Brus. Drying-mediated self-assembly of nanoparticles. *Nature*, 426:271–274, 2003.

[96] L. A. Ray and R. C. Baetzold. A monte-carlo estimation of surface-diffusion by simulating laser-induced thermal-desorption. *J. Chem. Phys.*, 93:2871–2878, 1990.

[97] J. W. S. Rayleigh. On convective currents in a horizontal layer of fluid, when the higher temperature is on the under side. *Phil. Mag. S.6*, 32:529–546, 1916.

[98] C. Redon, F. Brochard-Wyart, and F. Rondelez. Dynamics of dewetting. *Phys. Rev. Lett.*, 66:715–718, 1991.

[99] G. Reiter. Dewetting of thin polymer films. *Phys. Rev. Lett.*, 68:75–78, 1992.

[100] G. Reiter. Mobility of polymers in films thinner than their unperturbed size. *Europhys. Lett.*, 23:579–584, 1993.

[101] G. Reiter, J. Schultz, P. Auroy, and L. Auvray. Improving adhesion via connector polymers to stabilize non-wetting liquid films. *Europhys. Lett.*, 33:29–34, 1996.

[102] G. Reiter and A. Sharma. Auto-optimization of dewetting rates by rim instabilities in slipping polymer films. *Phys. Rev. Lett.*, 8716:166103, 1–4, 2001.

[103] O. Reynolds. On the theory of lubrication and its application to Mr. Beauchamp Tower's experiments, including an experimental determination of the viscosity of olive oil. *Phil. Trans. Roy. Soc.*, 177:157–234, 1886.

[104] N. Samid-Merzel, S. G. Lipson, and D. S. Tannhauser. Pattern formation in drying water films. *Phys. Rev. E*, 57:2906–2913, 1998.

[105] J. Sarkar, A. Sharma, and V. Shenoy. Adhesion and debonding of soft elastic films: Crack patterns, metastable pathways, and forces. *Langmuir*, 21:1457–1469, 2005.

[106] R. Seemann, S. Herminghaus, and K. Jacobs. Dewetting patterns and molecular forces: A reconciliation. *Phys. Rev. Lett.*, 86:5534–5537, 2001.

[107] R. Seemann, S. Herminghaus, and K. Jacobs. Shape of a liquid front upon dewetting. *Phys. Rev. Lett.*, 87:196101, 2001.

[108] R. Seemann, S. Herminghaus, C. Neto, S. Schlagowski, D. Podzimek, R. Konrad, H. Mantz, and K. Jacobs. Dynamics and structure formation in thin polymer melt films. *J. Phys.-Condes. Matter*, 17:S267–S290, 2005.

[109] A. Sharma. Disintegration of macroscopic fluid sheets on substrate: A singular perturbation approach. *J. Colloid Interface Sci.*, 156:96, 1993.

[110] A. Sharma. Equilibrium contact angles and film thicknesses in the apolar and polar systems: Role of intermolecular interactions in coexistence of drops with thin films. *Langmuir*, 9:3580, 1993.

[111] A. Sharma. Relationship of thin film stability and morphology to macroscopic parameters of wetting in the apolar and polar systems. *Langmuir*, 9:861–869, 1993.

[112] A. Sharma and G. Reiter. Instability of thin polymer films on coated substrates: Rupture, dewetting and drop formation. *J. Colloid Interface Sci.*, 178:383–399, 1996.

[113] P. Siepmann, C. P. Martin, I. Vancea, P. J. Moriarty, and N. Krasnogor. A genetic algorithm approach to probing the evolution of self-organized nanostructured systems. *Nano Lett.*, 7:1985–1990, 2007.

[114] I. I. Smalyukh, O. V. Zribi, J. C. Butler, O. D. Lavrentovich, and G. C. L. Wong. Structure and dynamics of liquid crystalline pattern formation in drying droplets of DNA. *Phys. Rev. Lett.*, 96:177801, 2006.

[115] D. J. Srolovitz and G. N. Hassold. Effects of diffusing impurities on domain growth in the Ising-model. *Phys. Rev. B*, 35:6902–6910, 1987.

[116] A. Stannard, C. P. Martin, E. Pauliac-Vaujour, P.J. Moriarty, and U. Thiele. Dual-scale pattern formation in nanoparticle assemblies. *J. Chem. Phys. C*, 112:15195–15203, 2008.

[117] V M Starov and M G Velarde. Surface forces and wetting phenomena. *Journal of Physics: Condensed Matter*, 21(46):464121, 2009.

[118] L. B. S. Sumner, A. M. Wood, and G. P. Neitzel. Lubrication analysis of thermocapillary-induced nonwetting. *Phys. Fluids*, 15:2923–2933, 2003.

[119] J. B. Swift, K. L. Babcock, and P. C. Hohenberg. Effects of thermal noise in Taylor-Couette flow with corotation and axial through-flow. *Physica A*, 204:625–649, 1994.

[120] C. G. Sztrum, O. Hod, and E. Rabani. Self-assembly of nanoparticles in three-dimensions: Formation of stalagmites. *J. Phys. Chem. B*, 109:6741–6747, 2005.

[121] K. Takei, V. Haucke, V. Slepnev, K. Farsad, M. Salazar, H. Chen, and P. De Camilli. Generation of coated intermediates of clathrin-mediated endocytosis on protein-free liposomes. *Cell*, 94:131–141, 1998.

[122] U. Thiele. *Entnetzung von Kollagenfilmen*. PhD thesis, Technische Universität Dresden, 1998.

[123] U. Thiele. Open questions and promising new fields in dewetting. *Eur. Phys. J. E*, 12:409–416, 2003.

[124] U. Thiele. Structure formation in thin liquid films. In S. Kalliadasis and U. Thiele, editors, *Thin films of Soft Matter*, pages 25–93, Wien, 2007. Springer.

[125] U. Thiele. Thin film evolution equations from (evaporating) dewetting liquid layers to epitaxial growth. *J. Phys.: Condens. Matter*, 22:084019, 2010.

[126] U. Thiele, S. Madruga, and L. Frastia. Decomposition driven interface evolution for layers of binary mixtures: I. Model derivation and stratified base states. *Phys. Fluids*, 19:122106, 2007.

[127] U. Thiele, M. Mertig, and W. Pompe. Dewetting of an evaporating thin liquid film: Heterogeneous nucleation and surface instability. *Phys. Rev. Lett.*, 80:2869–2872, 1998.

[128] U. Thiele, K. Neuffer, M. Bestehorn, Y. Pomeau, and M. G. Velarde. Sliding drops on an inclined plane. *Colloid Surf. A*, 206:87–104, 2002.

[129] U. Thiele, K. Neuffer, Y. Pomeau, and M. G. Velarde. On the importance of nucleation solutions for the rupture of thin liquid films. *Colloid Surf. A*, 206:135–155, 2002.

[130] U. Thiele, I. Vancea, A. J. Archer, M. J. Robbins, L. Frastia, A. Stannard, E. Pauliac-Vaujour, C. P. Martin, M. O. Blunt, and P. J. Moriarty. Modelling approaches to the dewetting of evaporating thin films of nanoparticle suspensions. *J. Phys.-Cond. Mat.*, 21:264016, 2009.

[131] U. Thiele, M. G. Velarde, and K. Neuffer. Dewetting: Film rupture by nucleation in the spinodal regime. *Phys. Rev. Lett.*, 87:016104, 2001.

[132] U. Thiele, M. G. Velarde, K. Neuffer, and Y. Pomeau. Film rupture in the diffuse interface model coupled to hydrodynamics. *Phys. Rev. E*, 64:031602, 2001.

[133] I. Vancea, U. Thiele, E. Pauliac-Vaujour, A. Stannard, C. P. Martin, M. O. Blunt, and P. J. Moriarty. Front instabilities in evaporatively dewetting nanofluids. *Phys. Rev. E*, 78:041601, 2008.

[134] E. Vives and A. Planes. Kinetics of a vacancy-driven order-disorder transition in a 2-dimensional binary alloy. *Phys. Rev. Lett.*, 68:812–815, 1992.

[135] D. D. Vvedensky. Multiscale modelling of nanostructures. *J. Phys.-Condes. Matter*, 16:R1537–R1576, 2004.

[136] T. R. Weikl, J. T. Groves, and R. Lipowsky. Pattern formation during adhesion of multicomponent membranes. *Europhys. Lett.*, 59:916–922, 2002.

[137] S. J. Weinstein and K. J. Ruschak. Coating flows. *Annu. Rev. Fluid Mech.*, 36:29–53, 2004.

[138] R. Xie, A. Karim, J. F. Douglas, C. C. Han, and R. A. Weiss. Spinodal dewetting of thin polymer films. *Phys. Rev. Lett.*, 81:1251–1254, 1998.

[139] G. Yosef and E. Rabani. Self-assembly of nanoparticles into rings: A lattice-gas model. *J. Phys. Chem. B*, 110:20965–20972, 2006.

[140] L. Zhang, S. Maheshwari, H. C. Chang, and Y. X. Zhu. Evaporative self-assembly from complex DNA-colloid suspensions. *Langmuir*, 24:3911–3917, 2008.